QUANTITATIVE CHARACTERIZATION OF PROCESSING-MICROSTRUCTURE-PROPERTIES RELATIONSHIPS IN PRESSURE DIE-CAST MG ALLOYS

A Dissertation
Presented to
The Academic Faculty

by

Soon Gi Lee

In Partial Fulfillment
of the Requirements for the Degree
Doctor of Philosophy in the
School of Materials Science and Engineering

Georgia Institute of Technology
August 2006

QUANTITATIVE CHARACTERIZATION OF PROCESSING-MICROSTRUCTURE-PROPERTIES RELATIONSHIPS IN PRESSURE DIE-CAST MG ALLOYS

Approved by:

Dr. Arun M. Gokhale, Advisor
School of Materials Science and Engineering
Georgia Institute of Technology

Dr. David M. McDowell
School of Mechanical Engineering
Georgia Institute of Technology

Dr. Meilin Liu
School of Materials Science and Engineering
Georgia Institute of Technology

Dr. Naresh N. Thadhani
School of Materials Science and Engineering
Georgia Institute of Technology

Dr. J. David Frost
School of Civil and Environmental Engineering
Georgia Institute of Technology

Date Approved: May 23rd, 2006

ACKNOWLEDGEMENTS

I would like to thank my family, especially my parents, without whose unfailing love and support I would not be where I am today.

I would like to thank many individuals who have contributed to my completion of this document. First and foremost, I would like to thank my advisor Dr. Arun Gokhale for his guidance, support, and encouragement throughout my time as a student at the Georgia Institute of Technology. Without his constant guidance, this work would not be possible.

Furthermore, I would like to thank my thesis committee members Dr. McDowell, Dr. Liu, Dr. Thadhani, and Dr. Frost for their help and constructive comments which resulted in what I believe to be a good thesis work. I thank Gautam Patel for support and expertise. I also thank my colleagues Arun Sreeranganathan, Scott Lieberman, Yuxiong Mao, Harpreet Singh, and Joel Harris for their support. They have not only given me friendship but have also been there giving me timely help when I was in need. Thanks to all my co-laborers who encouraged and strengthened me, who built me up and didn't tear me down.

This material is based upon work supported by Department of Energy Cooperative Agreement No. DE-FC05-02OR22910. Additional financial support was provided by the U.S. National Science Foundation under grant No. DMR-0404668. The financial support is gratefully acknowledged.

TABLE OF CONTENTS

LIST OF TABLES

LIST OF FIGURES

SUMMARY

The central goal of this research is to quantitatively characterize the relationships between processing, microstructure, and mechanical properties of important high-pressure die-cast (HPDC) Mg-alloys. For this purpose, a new digital image processing technique for automatic detection and segmentation of gas and shrinkage pores in the cast microstructure is developed and it is applied to quantitatively characterize the effects of HPDC process parameters on the size distribution and spatial arrangement of porosity. To get better insights into detailed geometry and distribution of porosity and other microstructural features, an efficient and unbiased montage based serial sectioning technique is applied for reconstruction of three-dimensional microstructures. The quantitative microstructural data have been correlated to the HPDC process parameters and the mechanical properties. The analysis has led to hypothesis of formation of new type of shrinkage porosity called, “gas induced shrinkage porosity” that has been substantiated via simple heat transfer simulations. The presence of inverse surface macrosegregation has been also shown for the first time in the HPDC Mg-alloys. An image analysis based technique has been proposed for simulations of realistic virtual microstructures that have realistic complex pore morphologies. These virtual microstructures can be implemented in the object oriented finite elements framework to model the variability in the fracture sensitive mechanical properties of the HPDC alloys.

CHAPTER 1

PROBLEM FORMULATION AND OBJECTIVES

During the recent years, magnesium alloys, as lightweight structural materials, have received considerable attention from many industries due to their unique combination of good strength and low density. In the automotive industry, the use of Mg-alloys has steadily increased since the early 1990s. Extreme lightness of magnesium, (density of 1.74 g/cm^3, which is two-thirds that of aluminum, less than half that of titanium, and less than one-fourth that of steel) makes it very attractive for automotive parts because lower components weight can lead to higher fuel efficiency and lower emissions. Consequently, during the recent years, automotive components such as steering wheels, instrument panels, seat frames, and doorframes are being manufactured from Mg-alloys. Most of the Mg-alloy components are manufactured via pressure die-casting process. However, the pressure die-casting process inevitably leads to formation of porosity and other casting defects that adversely affect the fracture related mechanical properties (such as ductility, toughness, and fatigue resistance) of the cast Mg-alloys. Nonetheless, very little research has been conducted to relate the process conditions and casting defects partly due to the lack of techniques to characterize the casting defects. Therefore, a systematic study of the quantitative correlations between important process parameters and the porosity/defect distributions in the cast Mg-alloys is of considerable practical interest. Accordingly, an important objective of this research is to quantitatively characterize and correlate effects of pressure die-casting conditions on the casting defects in some technologically important Mg-alloys. Another important objective of this research is to validate the models and computer simulations for casting processes on the basis of the quantitative experimental microstructural data. Optimized or improved

process conditions are proposed using validated computer simulations of the casting processes. These validated computer simulations provide a useful tool to optimize the process conditions and to develop the technology for manufacturing of high-pressure die-cast Mg-alloy components having reproducible and desirable microstructure and properties. Third important aim of this study is to develop the methodology to perform simulations based parametric studies on the effects of variations in the spatial arrangements and volume fraction of casting defects (mainly pores) on the micro-mechanical response of the microstructure. Such simulations will be useful for understanding of the variability of the mechanical properties corresponding to different microstructures. In summary, the main objectives of the research are as follows.

1. To develop a new digital image processing technique for quantitative characterization of porosity
2. To quantitatively characterize the effects of individual high-pressure die-casting process conditions on the casting defects and microstructure using novel digital imaging processing and stereology based techniques.
3. To simulate various microstructures by means of two-dimensional and three-dimensional microstructure reconstruction
4. To utilize the simulated microstructure for realistic parametric studies on the effects of variations in spatial clustering and other microstructure attributes on the micro-mechanical response in order to predict the variability in the mechanical properties of the pressure die-cast Mg-alloys

The results of the present research provide much needed science-based information for the development and applications of pressure die-cast Mg-alloy structural components that have reproducible desired fracture related mechanical properties.

CHAPTER 2

LITERATURE REVIEW AND BACKGROUND

2.1 Introduction

Since early 1990's, applications of magnesium alloys have rapidly grown in automotive and other industries due to their numerous attractive properties [1]. First, magnesium is the lightest of all structural metals: its density (~1.74g/cm^3) is two-thirds that of aluminum; less than half that of titanium; and less than one-fourth that of steel**.** Low inertia due to low density of magnesium is especially advantageous for structural parts, particularly for automotive components. The importance of magnesium in the automotive market is emphasized by the recent trend set by major automobile producers. It has been estimated [2] that each 10% saving in dead weight of a vehicle corresponds to an increase in fuel economy of 5.5%. This, in turn, can lead to reduced exhaust emissions. This is commercially important, because the US government's "Corporate Average Fuel Economy" (CAFE) legislation requires manufacturers to achieve progressive improvements in the fuel economies of vehicles. This legislation is providing much of the stimulus to weight-reduction programs through material substitutions. Consequently, many automotive manufacturers in Europe and America are utilizing increasing number of vehicle parts made of magnesium alloys that replace the steel and cast iron components in the older models [3]. Mg-alloys are currently being used for automotive frames, instrument panels, floors, brackets, and steering wheels, as well as in engine components, such as pistons and housings [4-7]. Magnesium alloys also have other attractive properties, such as high shock and dent resistance, a greater ability than aluminum to dampen noise and vibration, and good electromagnetic interference (EMI) shielding capability. Consequently, Magnesium alloys are now also being used for sports equipment (for example, baseball catchers' masks, skis, etc), and consumer goods such as

ladders, portable tools, electronic equipment, laptop cases, binoculars, cameras, furniture, and luggage [3].

2.2 Chemical Compositions of Mg-Alloys

Alloy designation for Mg-alloys named by the American Society for Testing and Materials (ASTM) is a three-part letter-number-letter system [1]. The first part consists of code letters indicating the two major alloying elements (listed in order of decreasing alloying content) and the second part consists of the weight percentages of these two elements (rounded off to the nearest whole number and listed in the same order as the code letters) [3]. The third part consists of an assigned letter to distinguish between alloys having the same nominal designation. For example, AM60B is a magnesium alloy containing approximately 6% aluminum and less than 1% manganese, and is the second specific composition registered having this nominal composition.

AM and AZ series of Mg-alloys are commercially important cast alloys. AM series of Mg-alloys are widely used for automotive applications such as steering wheels and instrument panels, where ductility and strength are of prime concern. These alloys are essentially Mg-Al alloys with minor quantity of Mn and impurities. Aluminum improves strength and hardness of Mg; it widens the freezing range as shown in Figure 2.1, Mg-Al binary phase diagram; and it makes the alloy easier to cast. Commercial Mg alloys rarely exceed 10 wt. % aluminum as higher Al content decreases ductility and toughness. Aluminum content of about 6 wt. % yields the optimum combination of strength and ductility in AM-series alloys. AM series alloys contain small quantity (~ 0.5 wt %) of Mn that is added to improve their saltwater corrosion resistance via removal of Fe and other heavy metal impurity elements from solid solution matrix through formation of intermetallic compounds. Zinc in AZ series of Mg-alloys is next to aluminum in effectiveness and often used in combination with aluminum to produce improvement in room-temperature strength [3].

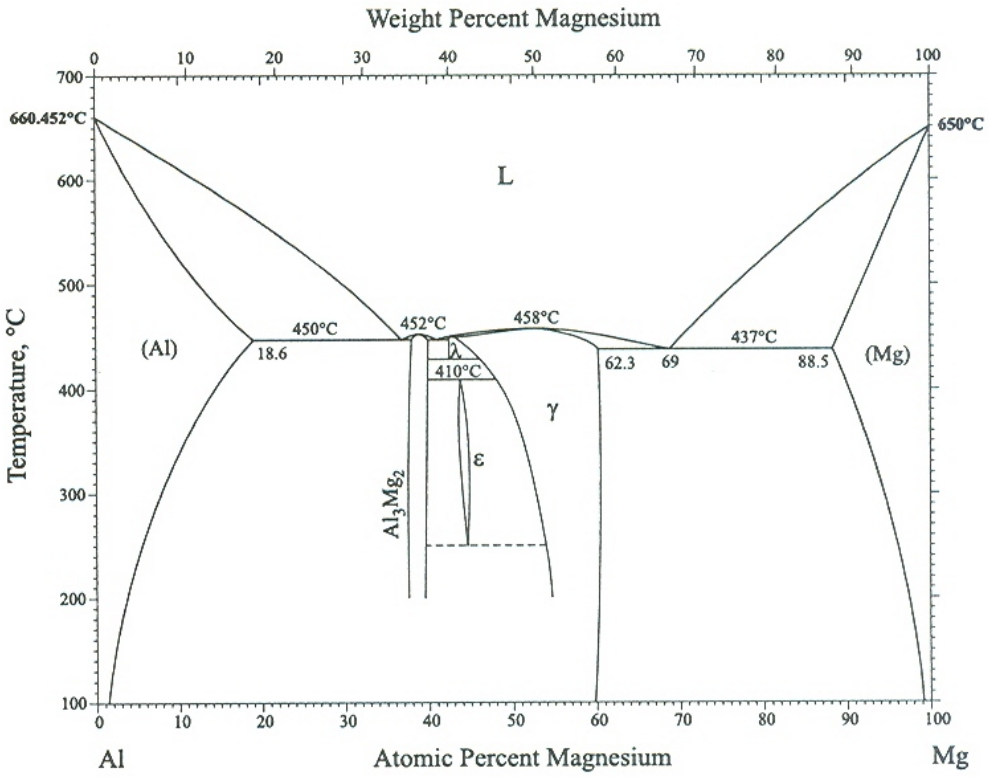

Figure 2.1: Mg-Al binary phase diagram [9].

2.3 Pressure Die-Casting of Mg-Alloys

Pressure die-casting, often called high-pressure die-casting (HPDC) to distinguish it from the gravity and low-pressure types of permanent-mold casting, is a process similar to permanent mold casting process except that the liquid metal is injected into the mold under pressure as shown in Figure 2.2. Die-casting is a fast and cost-effective manufacturing process for production of high volume complex net-shaped metal components. It has the benefit of increased quality and reproducibility, often at lower costs compared to other processes [8]. Die-casting equipment can typically produce large number of components (hundreds of thousands to millions) before requiring replacement. Pressure die-casting process generates parts that have good surface finish and dimensional accuracy (as good as 0.2 % of casting dimension).

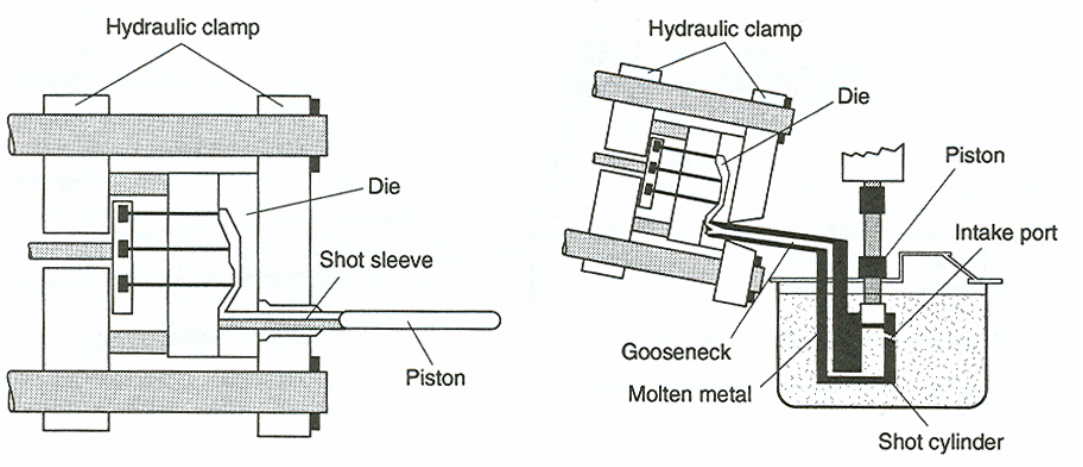

(a) (b)

Figure 2.2: Machines for die-casting magnesium alloys. (a) Cold-chamber machine and (b) Hot-chamber machine [3].

For many parts, post-machining can be totally eliminated, or only very light machining may be required to bring dimensions to required tolerance. Consequently, pressure die-casting is the most preferred fabrication process for Mg-alloy components used for majority of the automotive as well as numerous other applications. Microstructure of HPDC Mg-alloys contains features at numerous different length scales ranging from nanometers to millimeters. Important microstructural features are described in the following section.

2.4 Microstructure of Pressure Die-Cast Mg-Alloys

Depending on the alloy chemistry and processing conditions, the HPDC Mg-alloy microstructures contain features such as Mg-rich dendrite having local concentration gradients, eutectic constituents containing Mg-rich eutectic phases, other intermetallic compounds (for example, β-$Mg_{17}Al_{12}$ in AM series alloys and AlMnFe), and discontinuities such as gas and shrinkage pores, and internal oxide films. Figure 2.3 shows optical and corresponding scanning micrographs depicting several features in the microstructure of HPDC AM60 alloy.

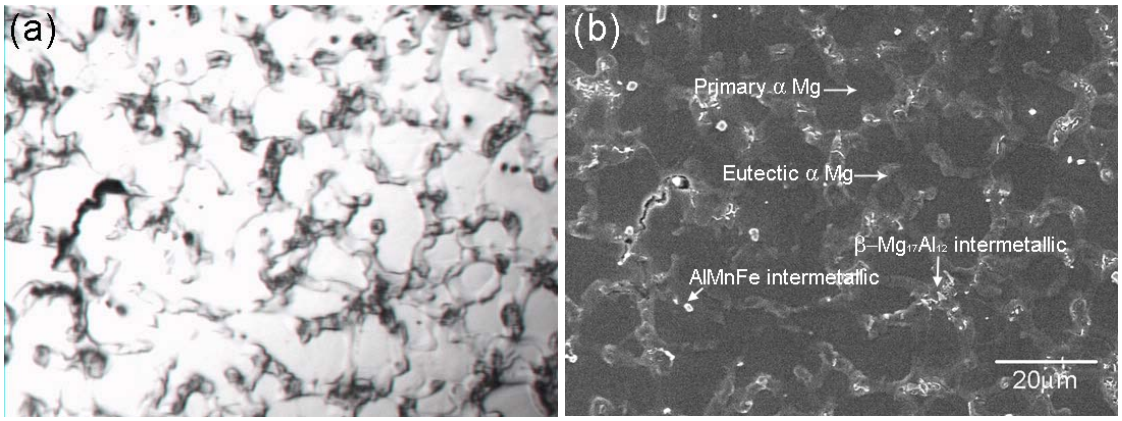

Figure 2.3: (a) optical and (b) corresponding scanning electron micrographs showing several phases present in the microstructure of AM60 alloy.

The geometric attributes of these microstructural features (such as their relative amounts, sizes, shapes, number densities, spatial distributions, etc.) primarily depend on the alloy chemistry, component geometry (section thickness, etc.), and process conditions [15-20].

2.5 Process Conditions and Casting Defects

Depending on the alloys chemistry, component geometry, and process conditions, the microstructure of HPDC Mg-alloys contains a variety of casting defects such as porosity (flow, gas, and shrinkage), defect bands, segregations, laminations, leakers, and inclusions [21]. Important microstructural defects are described in the following section and the effects of these casting defects on the mechanical properties of high-pressure die-cast Mg-alloys are presented in the subsequent section.

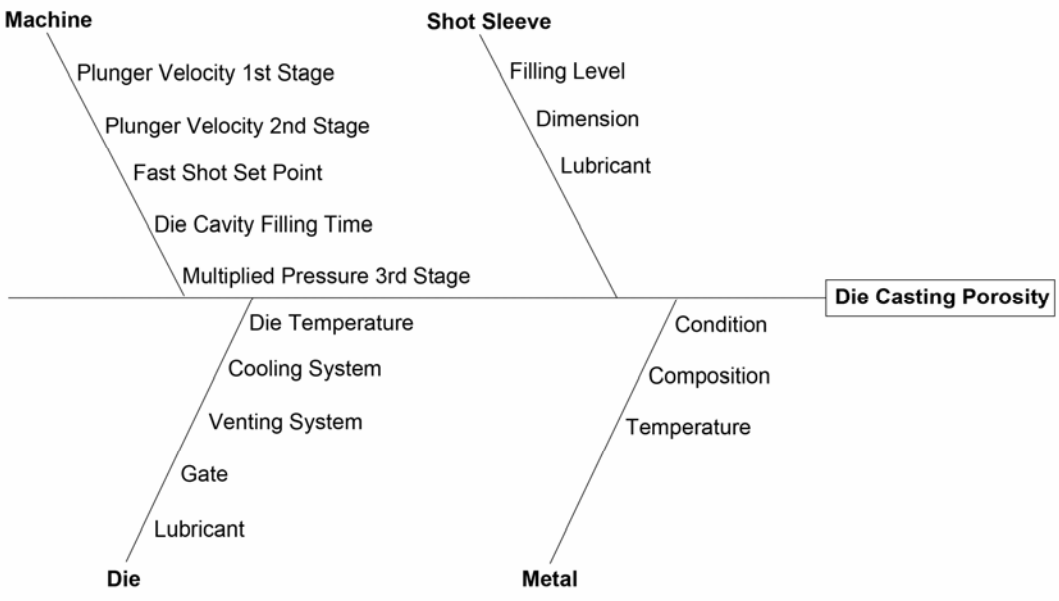

Figure 2.4: Cause and effect diagram for die-casting porosity [14].

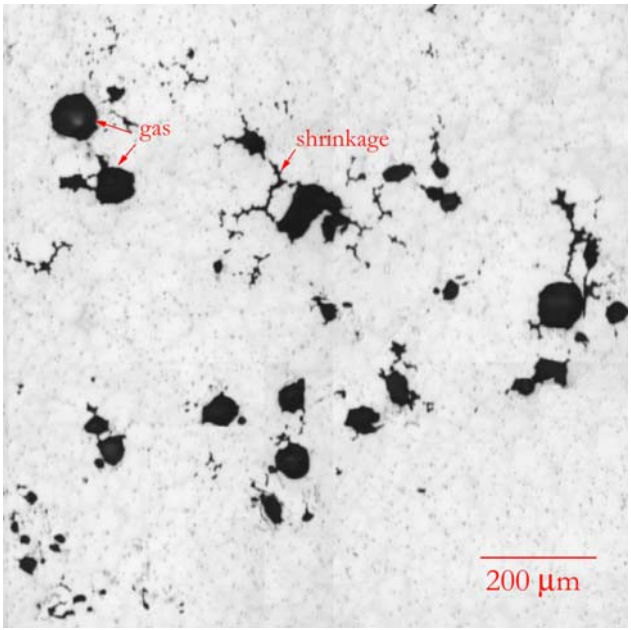

Figure 2.5: Optical micrograph of an unetched specimen showing round gas (air) and crack-like shrinkage pores.

2.5.1 Porosity

Among the casting defects, porosity is the most common and it is of major concern in the design of HPDC Mg-alloy components. Although high volume production and capability to produce near net shapes makes HPDC process very attractive, presence of large amount of porosity in the HPDC castings is a major disadvantage. The amount of micro-porosity, size and shape distribution of the micro-pores and their spatial clustering are governed by the alloy chemistry and high-pressure die-casting process parameters. Figure 2.4 identifies important high-pressure die-casting process parameters that affect micro-porosity [14]. Micro-porosity affects the fracture related mechanical properties of high-pressure die-cast Mg-alloys in an adverse manner.

The high-pressure die-cast Mg-alloys contain gas porosity as well as shrinkage porosity. The gas (air) pores appear as large round dark regions, whereas the shrinkage pores appear as elongated irregular dark regions as shown in Figure 2.5. The gas (air) pores are primarily due to entrapment of air present in the mold cavity during the casting process, whereas the shrinkage pores are predominantly due to insufficient melt filling followed by the solidification contraction. A part of the gas porosity may also be due to dissolved hydrogen (and other gases) in the liquid Mg-alloy and the trapped vapors of mold release agents sprayed on the die cavity surfaces. There have been numerous investigations on the relationships between the casting defects and process parameters such as melt temperature, cavity filling time, fullness of shot sleeve, piston rate, injection rate, die temperature, and other variables such as gate area, vent area, and die lubrication [15, 16, 20-31]. It is important to recognize that a given process parameters may affect the cast microstructure in more than one-way. For example, an increase in the melt temperature on the one hand improves the alloy castability (which can lead to a decrease in the amount of shrinkage porosity), but on the other hand, it can increase the amount of gas porosity due to an increase in the amount of dissolved hydrogen (and other gases) in the liquid alloy at a higher temperature. Further, the melt temperature in turn affects the

cooling rate, which can affect the dendrite cell size. Similarly, increasing shot sleeve fullness can lower the amount of micro-porosity, but it also leads to a decrease in the critical piston rate, which facilitates the micro-pore growth. During the pre-fill phase, the shot sleeve must be filled by a slow piston motion to avoid wave formation and air entrainment, until the metal fills the entire cross-section of the shot. The choice of the injection rate value is defined by two principal factors: die wearing and casting quality. High injection rate improves surface finishing, but it can increase casting porosity. The ratio between die temperature and casting temperature affects cooling rate and, consequently, characteristics such as skin thickness and grain size. Other variables such as gate area (closely connected with injection rate), vent area (closely connected with filling time or with injection rate), and die lubricant are also important factors to be considered. All of the casting defects affect the mechanical properties of cast alloys, therefore most of the studies have been done with the evaluation of the mechanical properties and their correlations to process parameters, rather than correlations between process parameters and porosity/defect attributes, which is required to understand how processing influences the microstructure.

2.5.2 Defect Bands

In HPDC components, bands of porosity or segregation are often present [11, 16, 32-33] that are parallel to the external surfaces of the casting. Such bands are more likely to be present in the thin-walled castings as shown in Figure 2.6. Dahle and co-workers [11] studied formation of defects bands and investigated the effect of casting conditions on casting integrity and the appearance of the bands. Formation of the defect bands is related to the solidification behavior, the mushy zone rheological properties, and the filling pattern of the casting with associated shearing of the mushy zone. It has been explained [11] that the central region may be predominantly formed by segregation and agglomeration of primary Mg-rich crystals/grains formed in the shot sleeve before

injection into the die, and consequently, one solidification front initiates at the center and proceeds towards the mould walls. At the same time, a second solidification front initiates from the mould walls and moves towards the center, leading to formation of shrinkage porosity where these two solidification fronts meet. This phenomenon can have a significant impact on the microstructural evolution of the casting and the mechanical properties, because defects bands contain solute rich segregation, porosity, or a combination of both. The amount and degree of localization of porosity formed in the defect bands depend on the alloy composition and the casting conditions.

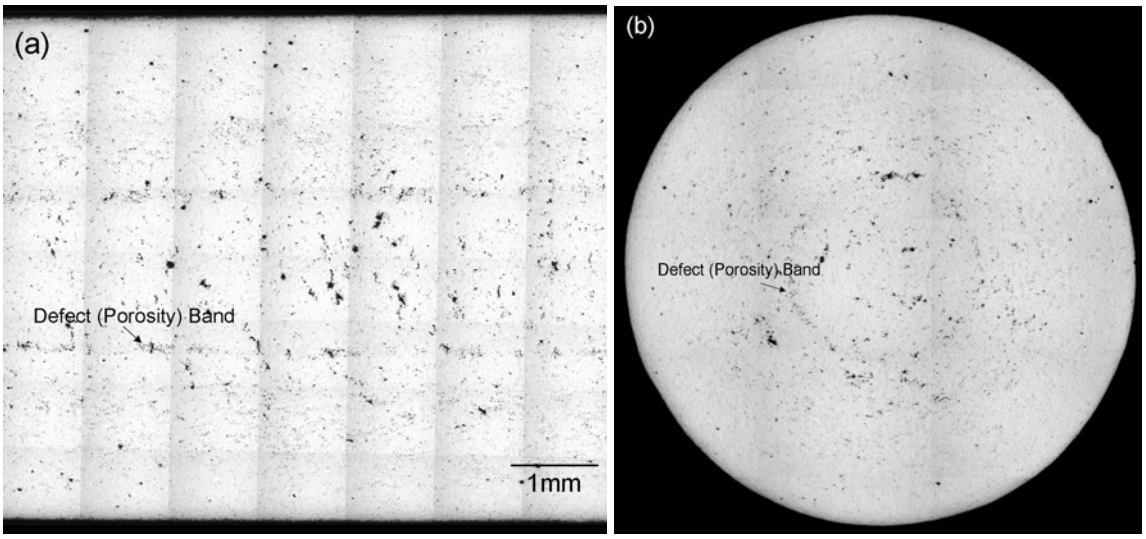

Figure 2.6: (a) longitudinal and (b) cylindrical cross-section of the tensile test bar (AM60) showing bands of porosity following the contour of the casting.

2.5.3 Inverse Surface Macrosegregation

Segregation results from various ways in which the solutes and impurities are redistributed within the solidified structure during solidification of alloys. Based on the scale of the segregation phenomena, it may be divided into two classes, namely, microsegregation and macrosegregation. Microsegregation is a short-range variation in

chemical composition such as that found between cells, dendrites, and grains, whereas macrosegregation refers to long range compositional variations such as those found between the outside and inside of a casting or ingot [31]. These compositional heterogeneities in the cast structure induce local variations in the mechanical properties. Particularly, macrosegregation has been believed to be the main cause of edge cracking during hot rolling of DC cast slabs as compared to the minor effect of inversesegregation that shows just compositional nonuniformity at the cast surface [34]. Another type of macrosegregation is known to occur when a semisolid external surface of a casting begins to contract from the mold wall, leaving a space into which the interdendritic liquid can flow. The pressure drop due to the air gap formation drives the liquid metal flow. A thin layer of highly segregated material referred to as exudation, in then formed at the surface of the casting. Figure 2.7 shows the schematic of formation of inverse surface macrosegregation.

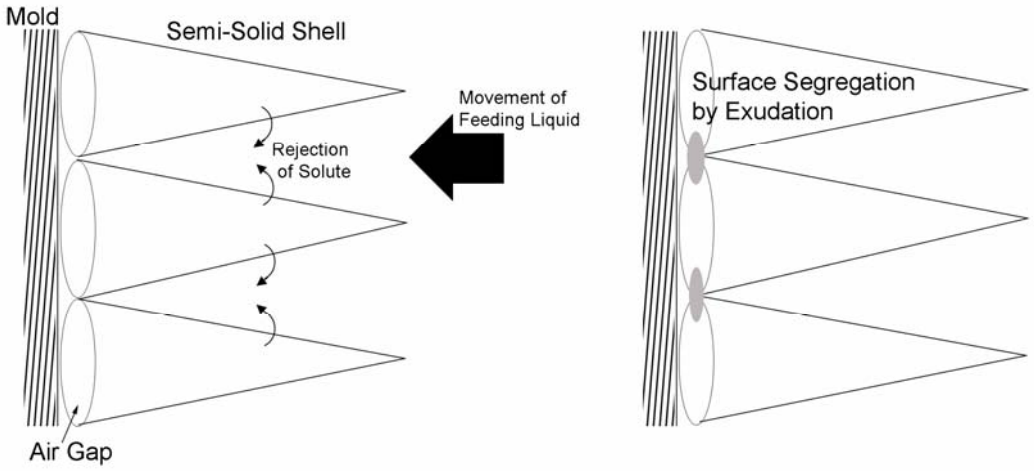

Figure 2.7: Schematic representation of formation of inverse surface macrosegregation.

This type of macrosegregation is some times called inverse surface macrosegregation as opposed to “normal” macrosegregation where the solute

concentration is lower at the surface and higher in the interior regions of the casting, and it has been observed in gravity cast in Al and Cu alloys [34-41]. In general, casting speed, cooling rate, metallostatic pressure, solidification shrinkage, and dendrite coarsening affect the inverse surface macrosegregation. Nonetheless, inverse surface macrosegregation has not been reported in Mg-alloys, in particular, high-pressure die-cast alloys. The preliminary research in this study has led to first observations of inverse surface macrosegregation in the high-pressure die-cast Mg-alloys [42-43]. Important microstructural observations and effects on mechanical properties are described in the chapter 5.1.3.1.

2.6 Mechanical Properties of Pressure Die-Cast Mg-Alloys

All casting defects adversely affect the mechanical properties of cast alloys, therefore numerous studies have been performed on evaluation of the effects of the microstructural defects on the mechanical properties and their correlations to process parameters. The effects of section thickness of a component on the microstructure and mechanical properties have also been conducted by many researchers [15-16, 25-26, 30]. In general, the volume fraction and average size of pores increase with the increase in section thickness due to insufficient liquid melt feeding, which adversely affect the fracture related mechanical properties. Another key factor that influences the mechanical properties is gate velocity. An increase in the gate velocity increases the amount of gas (air) porosity due to an increase in the entrapment of the air present in the die cavity [16, 20, 22, 27]. However, there exists an optimum gate velocity below which surface defects such as laps and cold shuts appear due to lack of sufficient heat content in the metal to fill the die. Gutman and co-workers [20] studied the effects of various die-casting parameters on the microstructure and mechanical properties of the AZ91D alloy. In this study, they

showed that casting temperature, injection rate, and slow shot rate are the most important process parameters that affect tensile and creep properties of high-pressure die-cast AZ91D alloy. Huang and co-workers [22] have studied the effects of some of these process parameters on the porosity levels in high purity AM60B alloy die-castings of cylindrical shape. The total porosity amounts (gas plus shrinkage porosity) were measured in polished and etched metallographic sections using image analysis. The authors have shown that that the increase in the consolidation pressure significantly reduces the total porosity if the piston rate is high, but the correlation doe not appear to be strong at the low piston rates. It is also observed that the piston rate itself influences the porosity levels. Chi-Ming Hung and co-workers [27] studied the effects of process conditions on the mechanical properties to determine the best combination of design parameters that can minimize the variations in the casting quality. These researchers employed the Taguchi optimization method for the design of experiments and data analysis. In this study, they showed that the optimum process conditions that minimize the variability in the properties consist of the lowest die temperature, slowest second shot velocity, lowest intensification pressure, and medium cooling rate. Another important factor is the melt temperature that mainly affects the amounts of dissolved gases and pre-solidified dendrite, and segregation. Gjestland and co-workers [15] reported that increasing melt temperature results in fine grain size due to possibly the lower fraction of pre-solidified dendrite and an increase in pressure induced nucleation sites, which improves the mechanical properties. However, higher melt temperature also increases the amounts of dissolved gases that result in the higher amount of the gas porosity. Gate velocity or injection rate is also an important factor that influences the porosity. Sequeira

and co-workers [16] studied the effects of gate velocity on the microstructure and mechanical properties of Mg-alloys. There exists an optimum gate velocity below which surface defects appear due to lack of sufficient heat content in the melt to fill the die and higher limit of gate velocity where porosity in the die castings increases possibly due to increased air entrapment. Other studies [20, 22, 27] have also led to similar conclusions. Consolidation pressure or intensification is applied to facilitate the feeding in the interdendritic channels, which may then lead to a decrease in the shrinkage porosity. And also the intensification pressure compresses the gas pores, and consequently, decreases their size. The research on the effects of intensification has been carried out [20, 22, 27]. Other important approach to reduce the porosity is use of partial vacuum in the die cavity prior to the metal fill [28, 29]. Niu and co-workers [28] showed that vacuum assistance reduces porosity and improves the mechanical properties as compared to conventional high-pressure die-casting process. McLaughlin and co-workers [29] have also observed similar beneficial effects of the vacuum assistance. Nevertheless, vacuum assisted high-pressure die-casting has not yet been widely used because of the complex set-up needed for the vacuum system, high cost, and numerous practical problems associated with use of such set up in a commercial production environment. Recently, Weiler and coworkers [44] used X-ray computed tomography to measure the size and distribution of macro-porosity within the gauge length of tensile samples of HPDC AM60B Mg-alloy, and have attempted to correlate amount of porosity with the tensile fracture strain. The results are in agreement with other works in that the area fraction of porosity that appears to be the major factor that affects the tensile strength and ductility of the magnesium alloy.

Although a lot of research has been done to correlate the process conditions with the mechanical properties, there are still numerous unresolved issues. In general, the measurement of the amount of porosity has been conducted by three ways: density measurements, conventional digital image technique, and X-ray tomography. The density method is not useful at low porosity levels and it gives only total amount of porosity; average pore size, etc. cannot be determined from density measurements alone. On the other hand, conventional digital image techniques yield more detailed information on the porosity attributes, however image analysis may lead to significant bias if the edge effects are not properly accounted for and/or if unbiased sampling techniques are not used. Further, in the earlier investigations [10], the image analysis techniques have been used to estimate the total porosity and not the separate amounts of gas and shrinkage porosities. However, gas and shrinkage porosities may have different functional dependencies on the process parameters and may not affect the mechanical properties in the same manner. Therefore, gas and shrinkage porosity should be segmented and separately characterized to study their effects on the mechanical properties. X-ray tomography is very good nondestructive technique in porosity measurement in that it yields various information on porosity such as size and spatial distribution in 3D space, however there are serious deficiencies in this technique: (1) low resolution (pores smaller than 80 μm could not be detected) they were not able to detect the shrinkage porosity at all because the thickness of crack-like shrinkage pores is on the order of few microns, and (2) gas pores smaller than 80 μm also could not be detected. Consequently, porosity measurements by X-ray tomography can seriously underestimate the total amount of porosity, as well as amount of gas porosity and average size of gas pores. It must be emphasized that crack-like

shrinkage pores as well as spatially clustered small pores exist in significant amounts in the HPDC Mg-alloys, and they are also expected to deleteriously affect the fracture sensitive properties such as tensile fracture strain. Therefore, it is strongly required to develop a new technique that has good porosity resolution and segment gas and shrinkage porosity to separately characterize individual effects on the mechanical properties.

Another important issue is the need for a systematic study on the effects of each process condition on the casting defects. The geometry of casting components should be simple enough to deconvolute the intrinsic effect of process conditions on porosity attributes, which should not be intrigued by the effects of the complex casting geometry. Further, the effect of each of process condition has also to be deconvoluted by keeping all the other parameters and process conditions constant. This study is designed to address these issues and will be discussed in the chapter 3.1

2.7 Three-Dimensional Microstructure Reconstruction

Material microstructures are usually of three-dimensional nature and opaque. However, the microstructural observations are generally performed in the two-dimensional (2D) metallographic sections through 3D microstructural domains of interest, although it is the 3D microstructure that governs mechanical properties. Clearly, a 2D metallographic section does not contain all the information concerning the true 3D microstructural geometry. In particular, the information concerning topological aspects of microstructure such as very complex topological connectivity and spatial distribution of porosity in cast microstructure cannot be obtained from independent 2D metallographic sections. Therefore, it is very essential to reconstruct and visualize 3D microstructure for understanding such aspects of 3D microstructural geometry. Depending on the material chemistry, processing, and microstructural length scales of interest, a 3D microstructure can be rendered using numerous techniques including X-ray computed tomography,

magnetic resonance imaging (MRI), and serial sectioning. This study concerns visualization of 3D microstructure from a stack of montage serial sections to observe short-, intermediate- and long-range spatial distribution and connectivity of porosity in the high-pressure die-cast Mg-alloys. The 3D microstructure of a relatively small microstructural volume of an opaque material can be reconstructed by using the classical serial sectioning technique developed in the 1970s [47]. The classical serial sectioning technique has been used in numerous investigations to study 3D microstructures of opaque materials [48-52], and it is quite useful for visualization of 3D particle/feature morphologies and short-range microstructural details at sufficiently high resolution. However, classical serial sectioning is not useful for quantitative characterization of topological attributes such as coordination numbers, and important descriptors of spatial arrangement of microstructural features such as higher order nearest neighbor distributions and radial distribution function due to serious bias (systematic error) resulting from edge effects [53-55]. The classical serial sectioning is also not useful for truly *unbiased* estimation of 3D grain/particle size distributions due to the same troublesome edge effects that create significant bias [56]. Further, the classical serial sectioning technique cannot be used to reconstruct large volume of 3D microstructure (~ $1mm^3$) at sufficiently high-resolution (~ 1μm). Therefore, it is not useful for characterization of long-range attributes of microstructural features. An efficient montage-based serial sectioning technique is available [53, 56, 57] that permits generation of significantly large volume (~ few mm^3) of 3D microstructure at a high resolution (~ 1μm). For approximately the same metallographic effort, the montage-based serial sectioning yields microstructural volume containing few thousand features, which provides sufficiently large statistical sample for efficient, reliable, unbiased, and assumption-free direct estimation of 3D microstructural properties as well as for study of topological aspects of microstructure such as feature connectivity.

In this study, the montage serial sectioning is applied to reconstruct large volumes of 3D porosity and other features of high-pressure die-cast Mg-alloys. Modern image processing and 3D image reconstruction techniques are used to reconstruct and visualize the 3D microstructure using volume and surface rendering techniques. Further, reconstruction of 3D porosity can provide useful insights into spatial arrangement and connectivity of porosity in 3D space and its relationship to solidification processes and mechanical properties.

CHAPTER 3

EXPERIMENTAL WORK

An important objective of this work is to quantitatively characterize the processing-microstructure-properties relationships in important high-pressure die-cast Mg-alloys. The experiments performed for this purpose are described in this chapter, in particular, high-pressure die-casting of model plates, and microstructure and properties characterization procedures are described in detail. The high-pressure die-casting was performed at Gibbs Die Casting Co, Evansville, Indiana, and the mechanical properties characterization tests were conducted at the Westmoreland Testing and Research Laboratories, Youngstown, Pennsylvania, whereas microstructure quantification work was carried out at Georgia Tech. The experimental data obtained from these experiments are analyzed in the next chapter.

3.1 Materials and Pressure Die-Casting Process

For the present study, two different AM series alloys (AM50 and AM60) have been high-pressure die-cast in a cold chamber machine at Gibbs Die Castings Inc., Evansville, IN. Nominal composition of these alloys is given in Table 3.1.

Table 3.1. Nominal chemical composition of AM50 (AM60) alloy.

Element (wt. %)	Al	Mn	Zn	Si	Cu	Ni	Balance
AM50 AM60	4.5–5.5 5.5-6.5	0.25min	0.22max	0.1max	0.01max	0.002max	Mg

The square high-pressure die-cast AM50 plates are of 146mm × 146mm × 14.3mm dimensions, whereas AM60 thin plates are of 200mm × 100mm × 4.3mm

dimensions. Numerous sets of AM50 and AM60 Mg-alloy plates were high-pressure die-cast using the combination of process parameters given in Table 3.2.

Table 3.2. Process parameters for high-pressure die-castings.

Plate ID		Gate Velocity (m/sec)	Intensification	Melt Temp. (°C)
AM50 (AM60)	Plate B	35	On	682
	Plate I	56 (5.2)	On	705
	Plate G	35 (2.7)	Off	705
	Plate M	56 (5.2)	Off	682
	Plate W	56 (5.2)	Off	705

The process parameters affect the porosity distributions in a variety of different ways, and therefore, it is essential to "deconvolute" the effects of individual process parameters on the porosity and other microstructural attributes to develop a thorough understanding of the process-microstructure correlations in the high-pressure die-cast Mg-alloys. This is the major weakness of most of the earlier experimental studies: the effects of individual process parameters (for example, gate velocity) on the porosity distributions have not been quantitatively characterized keeping all other process parameters constant. In particular, the present experiments were designed to *deconvolute* the effects of gate velocity, intensification pressure, melt temperature, and component thickness on the porosity and other casting defects and microstructures of AM50 and AM60 alloys. In all of these experiments, the die was heated through passage of steam. In order to deconvolute the effects of gate velocity, intensification, and melt temperature on the microstructure and casting defects, all other parameters such as vent area, casting geometry, gate dimensions, die temperature, etc. were kept the same during high-pressure die-casting of all the plates. Table 3.2 gives the values of the process parameters that have been varied to understand the process-microstructure relationships of interest. This design of experiments permits deconvolution of the individual effect of gate velocity

(plate G and W), intensification (plates I and W), melt temperature (plates M and W), and section thickness on the porosity levels in the cast microstructure of the high-pressure die-cast AM50 and AM60 Mg-alloys.

3.2 Metallography

For the purpose of porosity characterization, the dimension along the direction of the nominal liquid metal flow direction is designated as the "length" direction of the plates (Figure 3.1a). To characterize the porosity distributions as a function of the distance along the length, width, and thickness of the plates, the metallographic specimens were sectioned at different distances along the length of the plates at orientation perpendicular to the length direction. Due to the symmetry with respect to the centerline, only half of the area of each metallographic section (from center to edge, see Figure 3.1a) has been metallographically examined in each plate. The porosity measurements have been performed at various locations along the plate width as shown in Figure 3.1b). At each such location sampled along the length and width directions, the porosity measurements have been performed at different locations along the thickness direction of the plates from bottom to top plate surface. Similar sampling scheme was used for AM60 thin plates, but considering their small thickness, five sections along the length direction and three sections along the thickness direction were sufficient to characterize the spatial variation of porosity as illustrated in Figure 3.2 a and b.

The metallographic specimens were mounted in standard metallographic mounts, and then they were ground using 320 grit to 1000 grit abrasive SiC papers. Immediately after the last grinding step, the specimens were washed with water, rinsed with methanol, and dried. The fine polishing was conducted using 6μm and 1μm oil based diamond compounds.

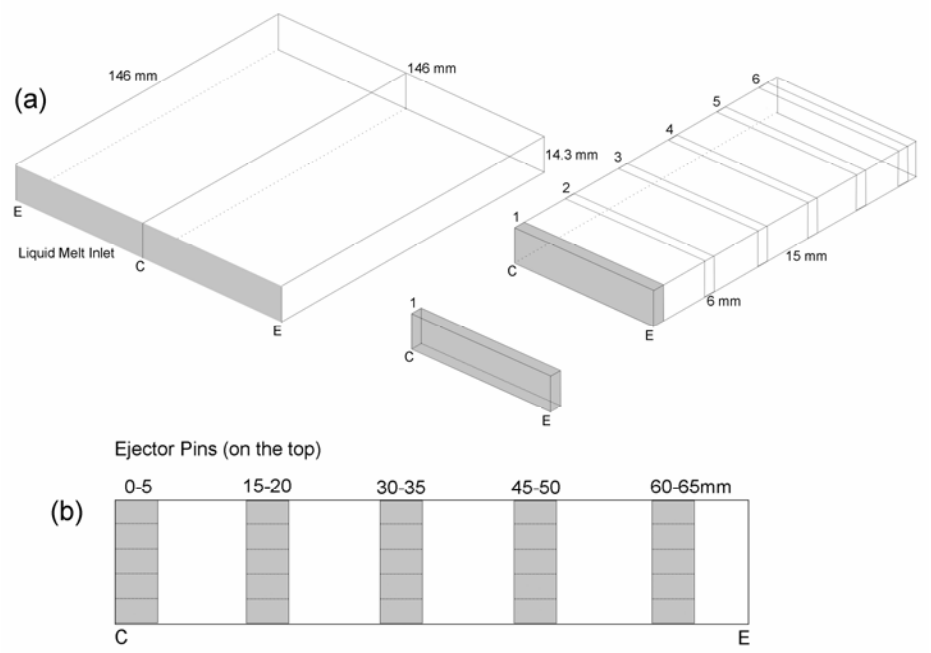

Figure 3.1 : (a) Schematic plate geometry and locations along the plate length where the metallographic specimens have been drawn, (b) locations along the width directions where the porosity measurements have been performed (AM50 thick plates).

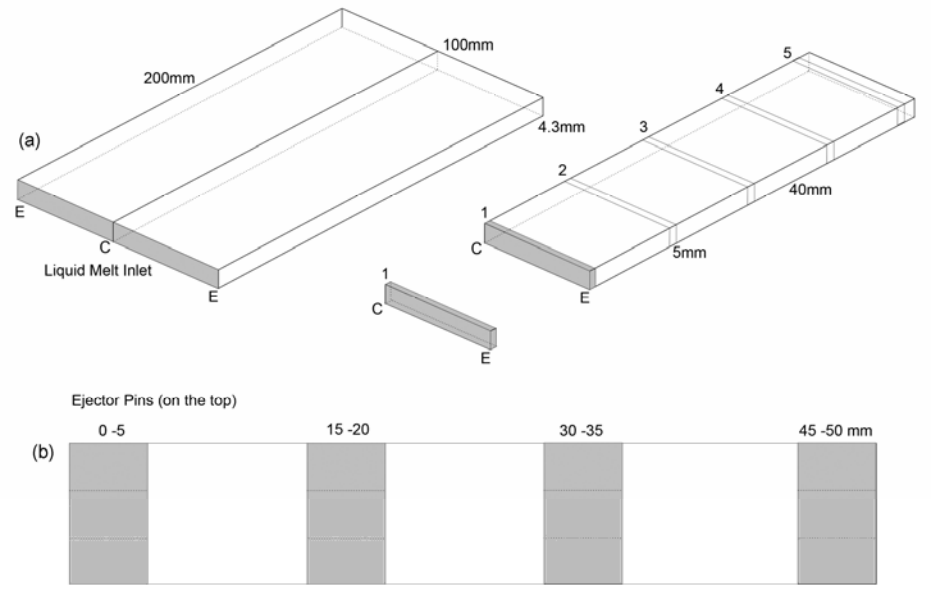

Figure 3.2: (a) Schematic plate geometry and locations along the plate length where the metallographic specimens have been drawn, (b) locations along the width directions where the porosity measurements have been performed (AM60 thin plates).

The final steps in polishing involved the use of 0.3μm alumina and 0.05μm colloidal silica. Glycerol and oil base lubricants were used during these polishing steps to avoid the formation of a surface film. The specimens were immediately rinsed with methanol and dried. The specimens were examined in the *as-polished condition* (without etching) for the porosity measurements and in the polished and etched condition for other microstructural features such as eutectic compounds and inverse surface macrosegregation. In the present work, three important casting defects observed in the AM50 and AM60 high-pressure die cast plates, namely, porosity, inverse surface macrosegregation, and porosity bands have been characterized. The characterization methods are presented as follows.

3.3 Digital Image Analysis and Stereology

Quantitative characterization of porosity attributes using automated digital image analysis involved the following three steps for *unbiased* estimation of the attributes of gas and shrinkage pores that are free of *edge effects*: (i) creation of "montage" of all the contiguous fields of view in the entire metallographic section, (ii) separation of gas and shrinkage pores using developed digital image analysis, (iii) automated stereological measurements and estimation of volume fraction and other attributes of the gas and shrinkage pores. These procedures are described as follows.

3.3.1 Montage Creation

Traditional microscopy involves observation of microstructure "one field of view at a time." The microstructural observations are usually carried out at a sufficiently high resolution (high magnification) to clearly resolve the features (for example, micropores in the present case) of interest, and as a result, only a limited area of the metallographic plane is observed in any given field of view. Quantitative microstructure characterization in such discrete microstructural fields is problematic as some features are intersected by

the observation frame boundaries, and therefore, they are only partly present in the microstructural field under observation. The size of such partly-in-partly-out features cannot be precisely measured as only a part of these features is observed. Not counting such features also creates a problem: larger features are more likely to interest the frame boundaries, and therefore, not counting the partly-in-partly-out features creates an unknown statistical bias (systematic error) in the estimation of attributes such as size distribution and average size. This difficulty can be resolved by creating a seamless "montage" of very large number of contiguous microstructural fields to cover the whole metallographic section captured at a sufficiently high resolution. The microstructural measurements on such large-area high-resolution image eliminate the bias due to edge effects created by the observation frame boundaries for all practical purposes. Using modern image analyzers, it is possible to create a seamless "montage" of very large number of contiguous microstructural fields of view [45, 46], where each field of view is captured at a high magnification such that all features of interest is clearly resolved. Since the montage is at high resolution and is of very large area, it is able to capture both small and long-range microstructural patterns and contains sufficiently large number of features so that the edge effects are eliminated for all practical purposes.

In the present work, the image montages have been made by tiling 280 contiguous fields of view for AM50 thick plate sections and 72 contiguous fields of view for AM60 thin plate sections at 0.97 μm pixel, captured through a Sony (XC-75) CCD camera mounted on an inverted stage Zeiss (Axiovert 100 A) microscope. The images are 8-bit gray-scale images. The tiling has been performed by a computer controlled motorized stage of the microscope; image correlation subroutines are used to match the edges of contiguous fields. The final montages are at a magnification such that each pixel is of 0.97 μm size and the total area covered by each montage is 60mm^2 for thick plates and 16mm^2 for thin plates.

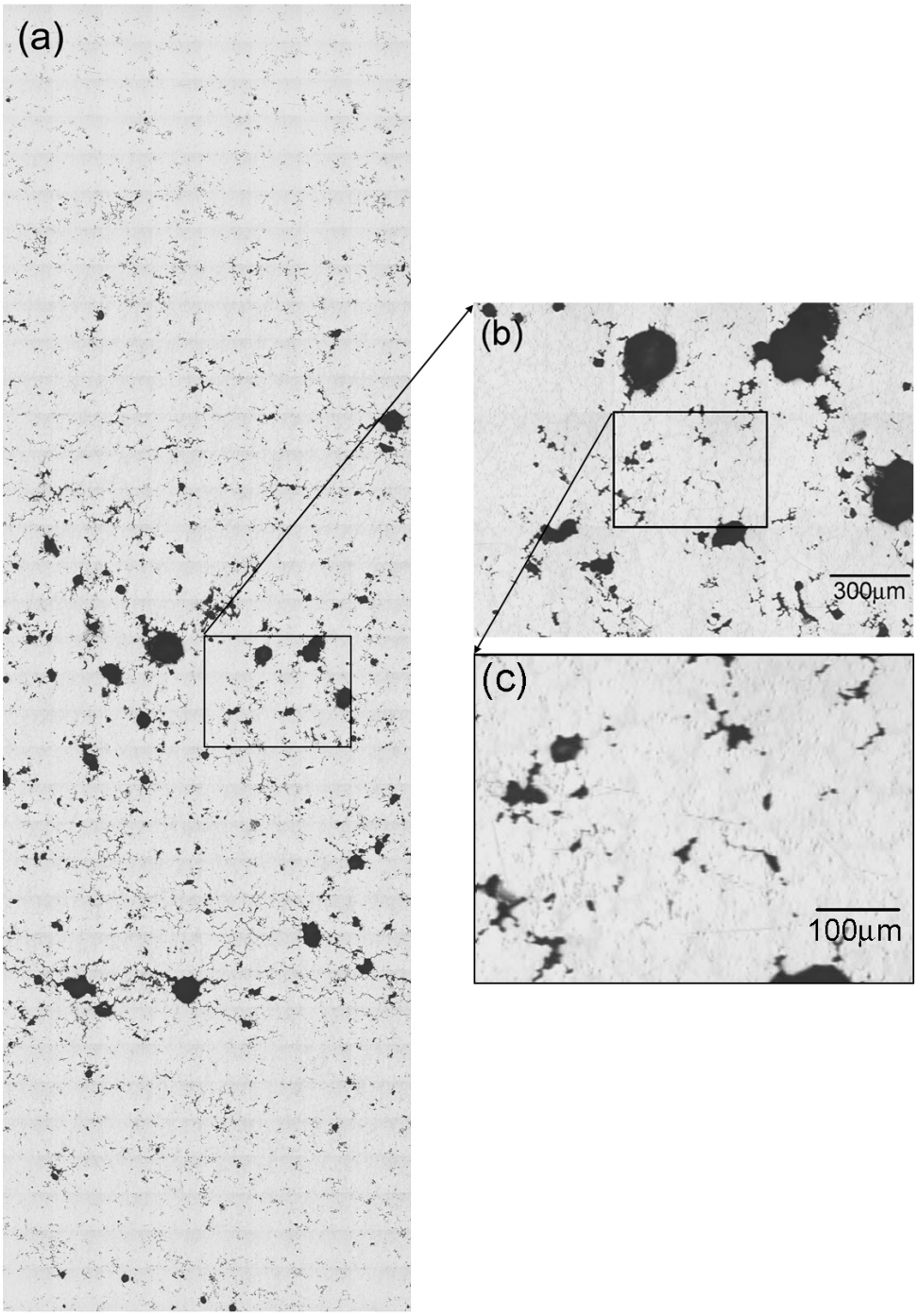

Figure 3.3: (a) Digitally compressed seamless montage of 280 contiguous microstructural fields covering the complete thickness of the AM50 thick plate (14.3 mm). (b) Enlarged view of the small window in (a). (c) Enlarged view of the small window in (b). This is one field of view in a. Each microstructural field in the montage in (a) has been captured at this resolution/magnification.

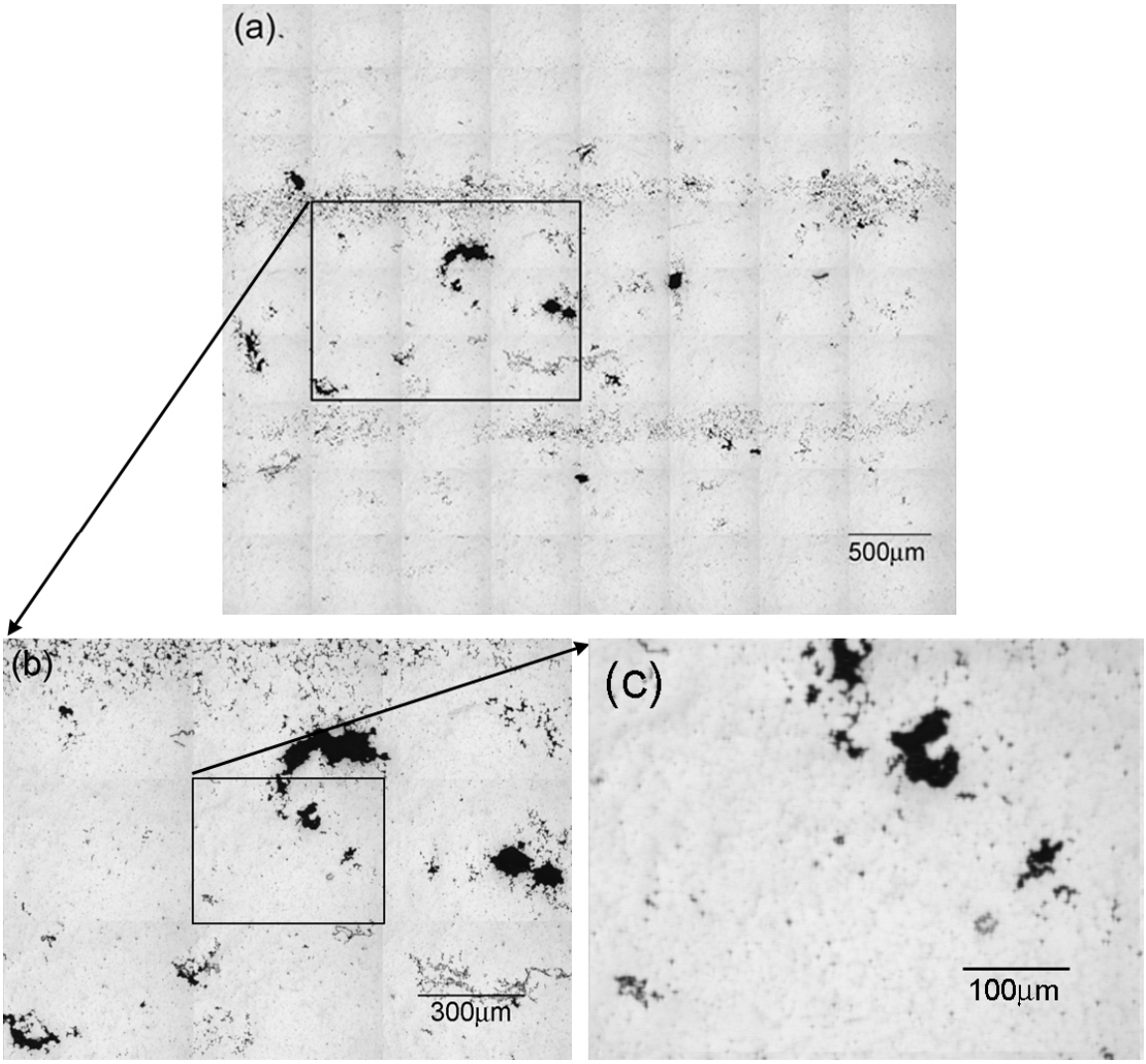

Figure 3.4: (a) Digitally compressed seamless montage of 72 contiguous microstructural fields covering the complete thickness of the AM60 thin plate (4.3 mm). (b) Enlarged view of the small window in (a). (c) Enlarged view of the small window in (b). This is one field of view in a. Each microstructural field in the montage in (a) has been captured at this resolution/magnification.

Figure 3.3a shows one such montage containing 280 contiguous microstructural fields that have been captured at the resolution of the micrograph in Figure 3.3c, which is one of the fields of view in the montage. The montage in Figure 3.3a covers the complete thickness of the die-cast plate (14.3 mm), which is along the y-axis of the montage. Such montages were created at different locations along the length and width of the cast plates (Figure 3.1) to characterize the porosity at different locations.

3.3.2 Separation of Gas and Shrinkage Porosity

It is important to recognize that (i) gas and shrinkage pores have different morphologies, and (ii) they have slightly different levels of relief in the metallographic plane. Therefore, these differences can be used to segment and separate the gas pores from shrinkage pores. The next step in the image analysis procedure is to separate the large gas (air) pores in the image montage from the rest of microstructure in order to measure their sizes, centroid coordinates, etc. Balasundaram and Gokhale [3] have developed an image processing method to separate the gas pores from shrinkage in the cast microstructure. In the present work, this method has been modified and further improved to account for highly inter-connected nature of the pores in AM50 plates. In case of the AM50 thick plates, gas and shrinkage pores are highly interconnected and therefore it is essential to disconnect such type of shrinkage pores from gas porosity. Further, depending on their shape and distribution in the microstructure, algorithms for separation of gas from shrinkage porosity do require some fine-tuning. To account for these details, a modified image analysis procedure was developed, which is described as follows. Figure 3.5 shows the algorithm for the complete image analysis procedure in the form of a flow chart. Montage creation is the first step (step 1) in this flow chart. The second step in the image analysis procedure is to convert the gray scale montage image into its binary image in order to measure their sizes, perimeters, centroid coordinates, etc. Gray scale montage image is converted into its binary image by thresholding (step 2).

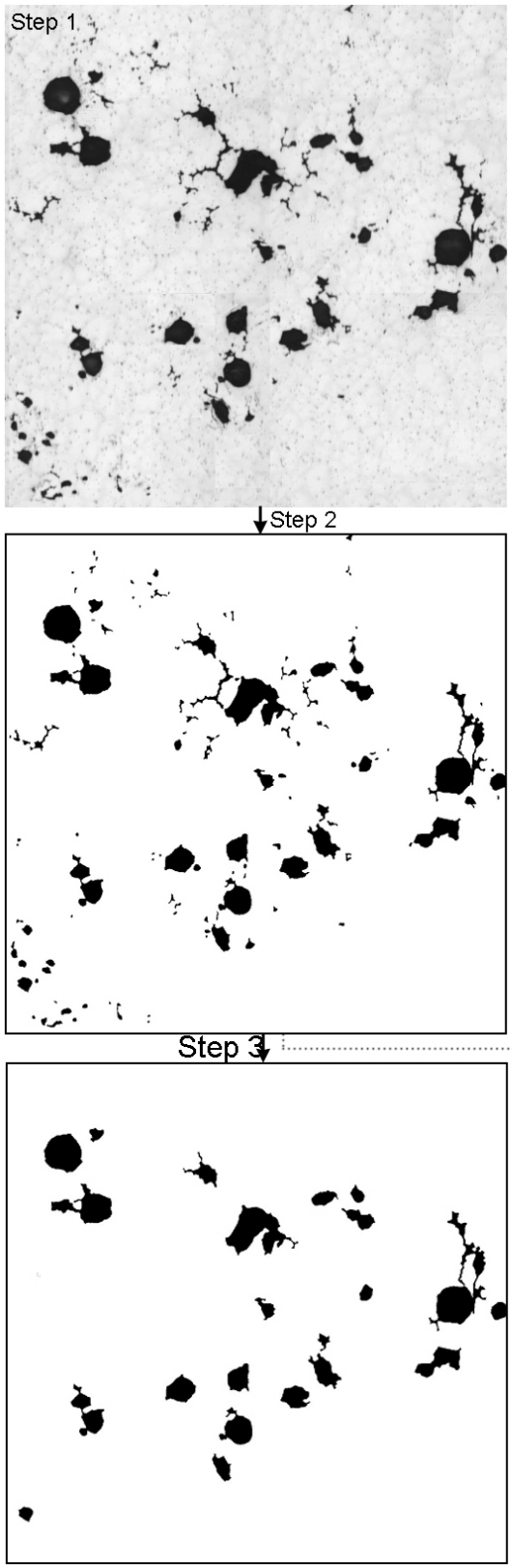

Step 1. Creation of "montage" of polished sample
Step 2. Thresholding of montage to obtain its binary image
Step 3. Separation of large gas from small gas and shrinkage
Step 4. Disconnection of shrinkage from large gas and adding shrinkage onto previous small gas and shrinkage
Step 5. Separation of small gas from shrinkage and adding small gas onto large gas

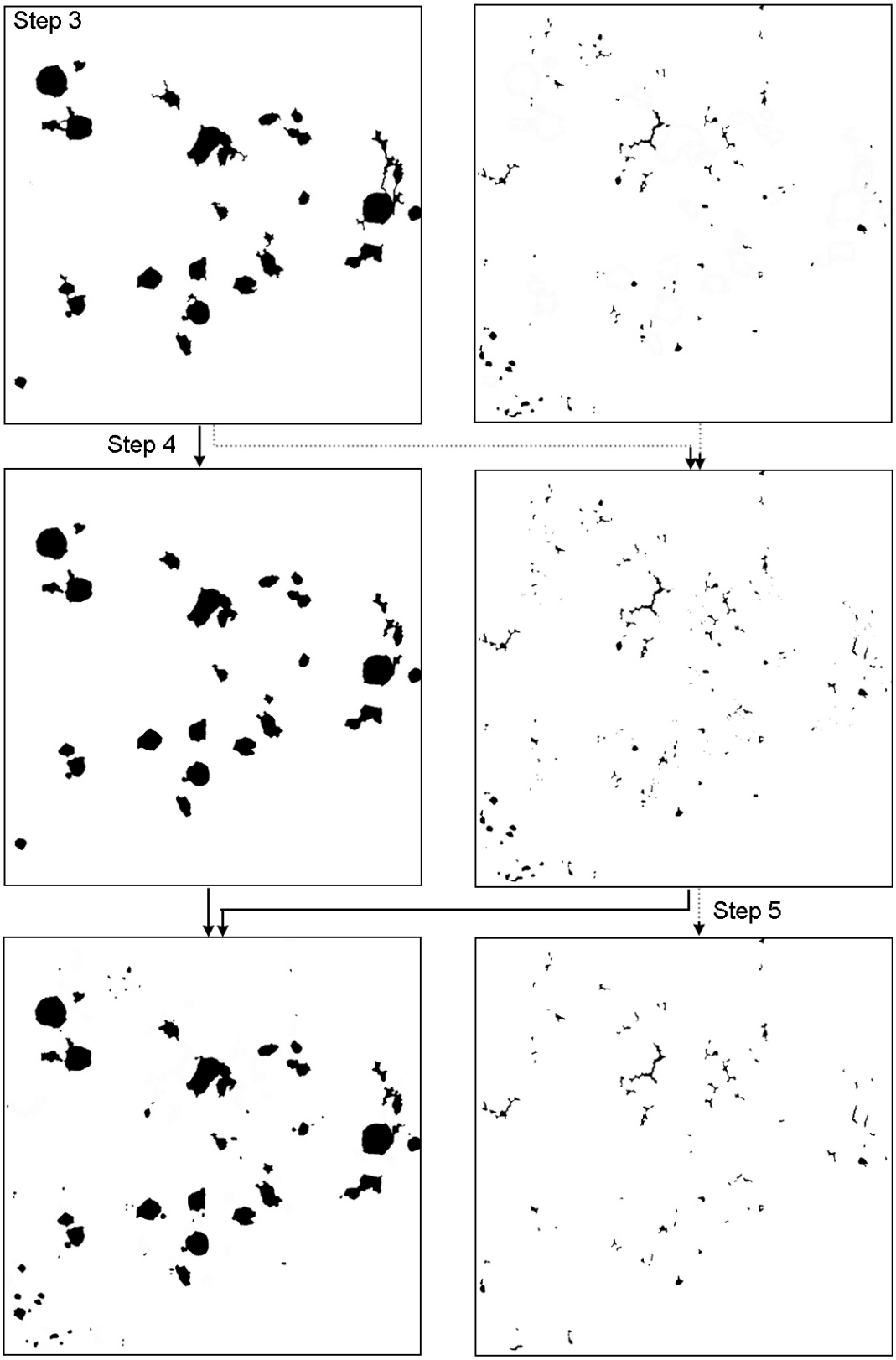

Figure 3.5: Flowchart algorithm for the separation procedures of gas and shrinkage pores.

From the binary image, large gas pores are first separated from the remaining porosity (step 3) using the difference in their area (gas pores larger than 20 μm equivalent circle diameter are regarded as large pores). This leads to creation of two binary images; one containing only large gas pores and the other containing only small gas pores and shrinkage pores. Depending on the alloy compositions, components geometry, process conditions, etc, some of shrinkage and gas porosity are highly interconnected. Therefore, next step is to separate connected shrinkage porosity from gas pores and adding shrinkage porosity onto the binary image containing small gas and shrinkage porosity obtained in the step 3. This is shown as step 4 in the flowchart. This step is not activated if the microstructure does not contain any connected shrinkage and gas porosity or if the binary image is to be used in a model for Finite Element (FE) based analysis. The separation of small gas pores from shrinkage pores in the binary image utilizes the differences in aspect ratio, quantified by the parameter, [perimeter/$\pi \cdot D_{circle}$], as aspect ratio of shrinkage pores is much larger than the gas pores (step 5). The small gas pores identified in this manner are separated and added onto the earlier binary image containing only the large gas pores to create an image containing the total gas porosity (no shrinkage pores). Consequently, the gas and shrinkage pores can be quantified separately.

Figure 3.6a shows the grayscale montage of 280 contiguous microstructural fields of AM50 thick sections and Figure 3.6b is the corresponding binary image showing both the gas and shrinkage porosity. Figure 3.6c shows the image with only gas pores, whereas Figure 3.6d is the image with only the shrinkage porosity. Gray scale montage and corresponding binary images for AM60 thin sections are shown in Figure 3.7. The gas and shrinkage pores were then quantitatively characterized by estimating their volume fraction (percentage), size distribution, number density, centroid coordinates, perimeters, etc using automatic digital image analysis on the separate montages containing only gas pores and only shrinkage pores. These data enable detailed investigation of the effects of gate velocity, intensification, and melt temperature on the porosity attributes.

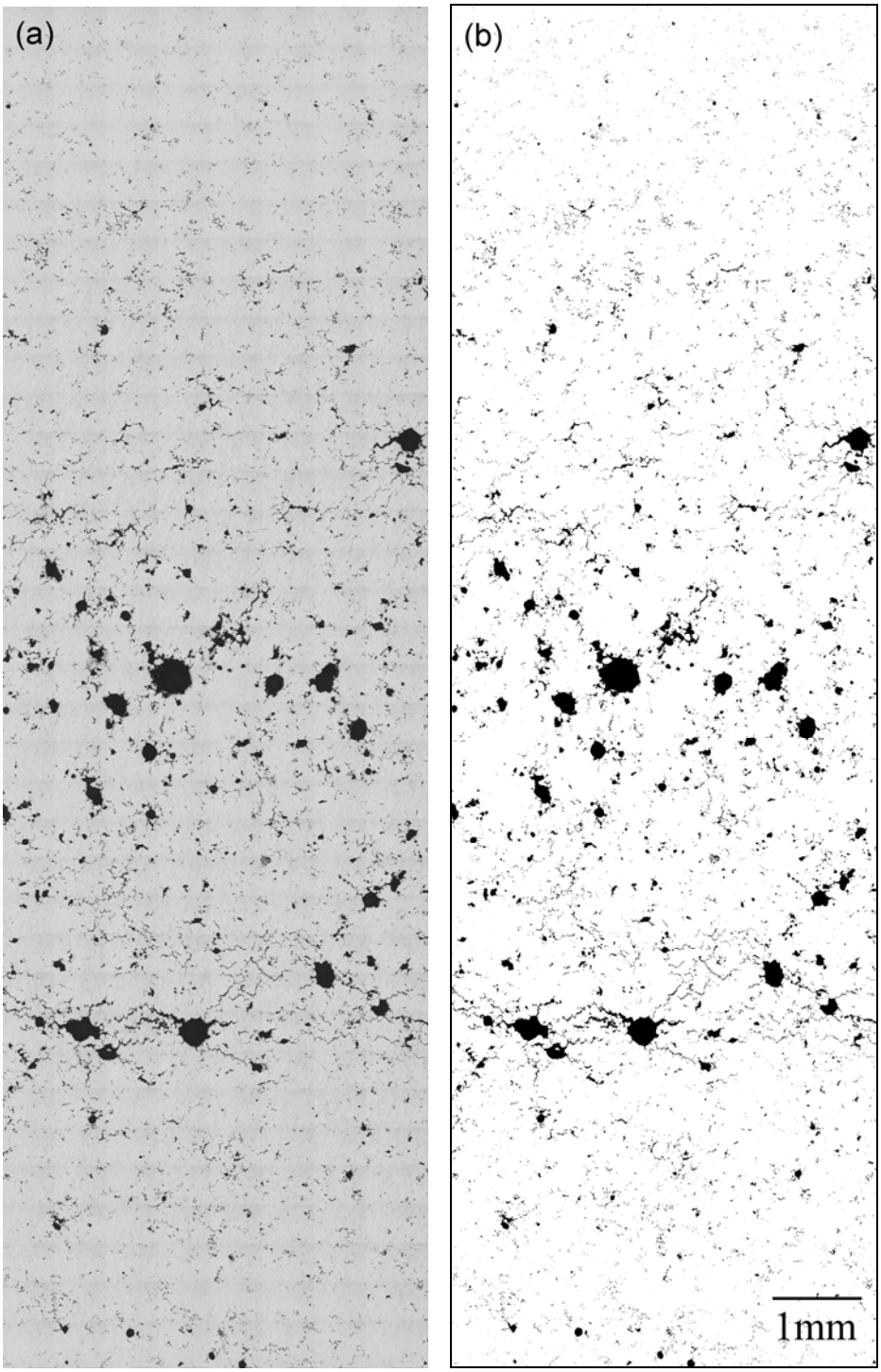

Figure 3.6: (a) Gray scale montage of 280 contiguous fields of view of AM50 thick sections covering the thickness of the plate showing gas and shrinkage pores, (b) binary image of the gray scale image (continued)

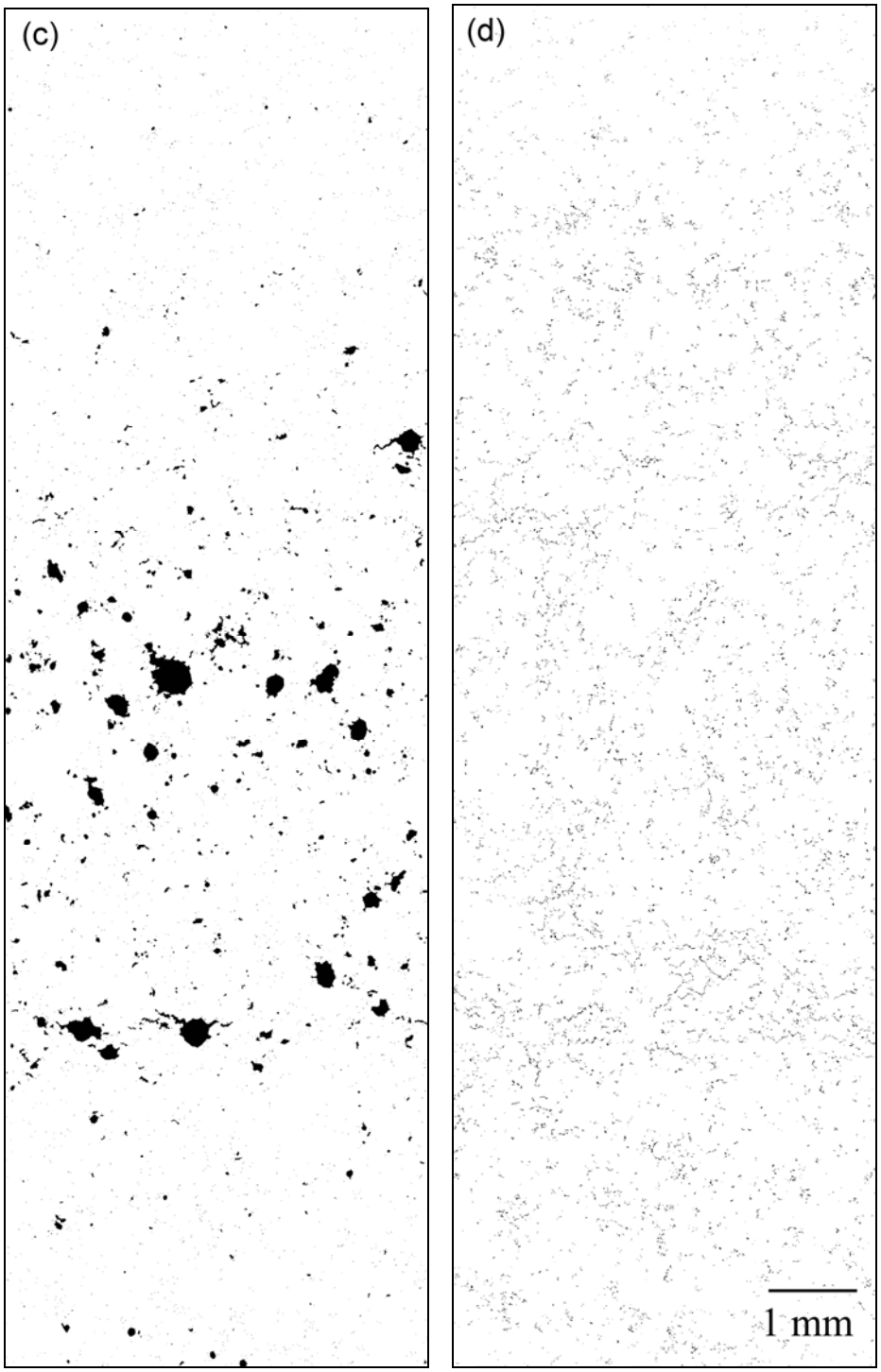

Figure 3.6: (c) the image containing only the gas pores, and (d) the image containing only shrinkage pores.

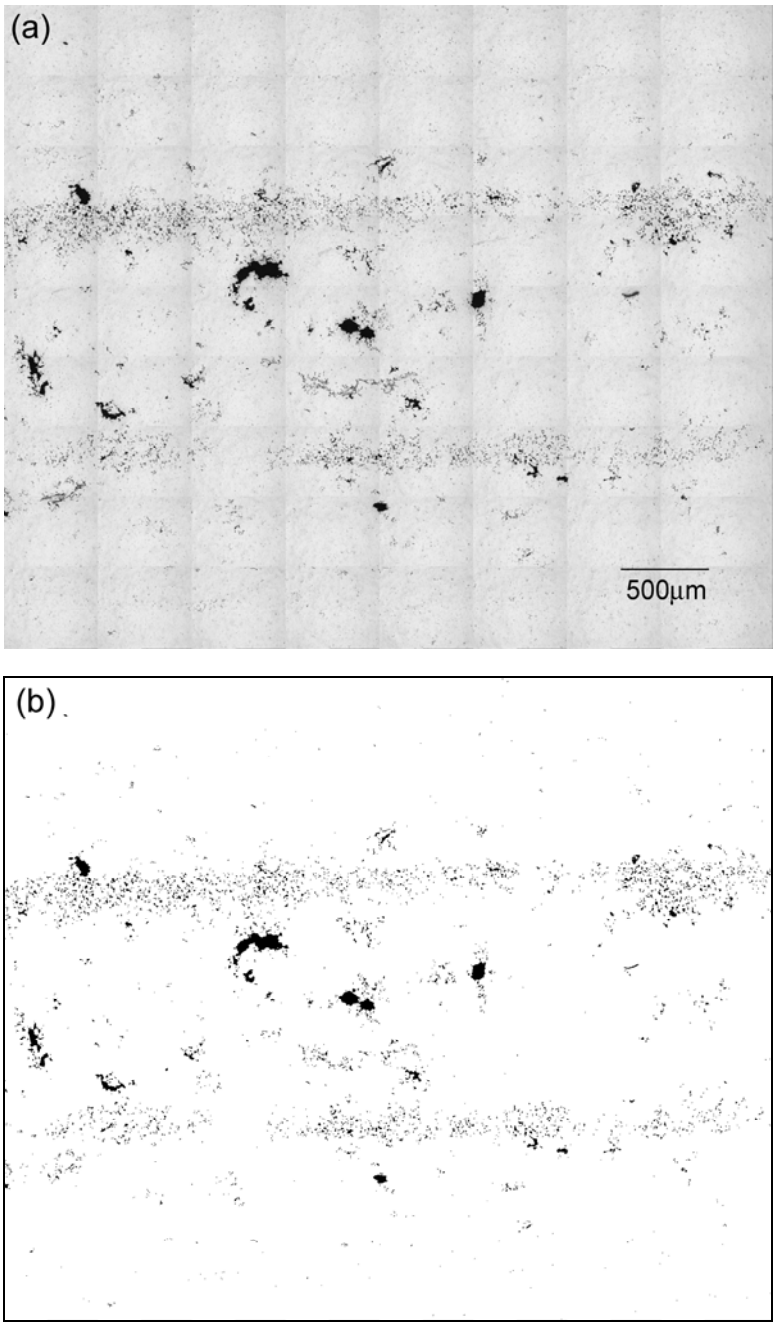

Figure 3.7: (a) Gray scale montage of 72 contiguous fields of view of AM60 thin sections covering the thickness of the plate showing gas and shrinkage pores, (b) binary image of the gray scale image (continued)

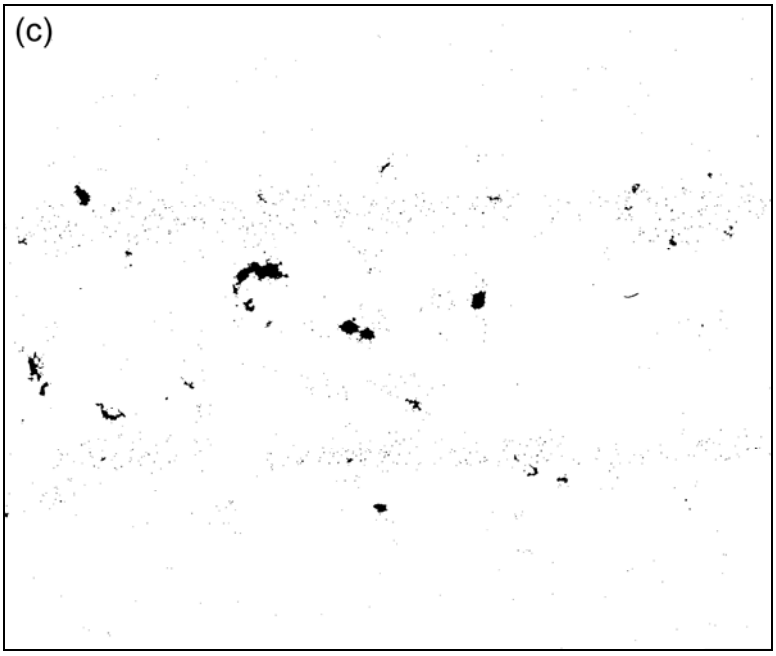

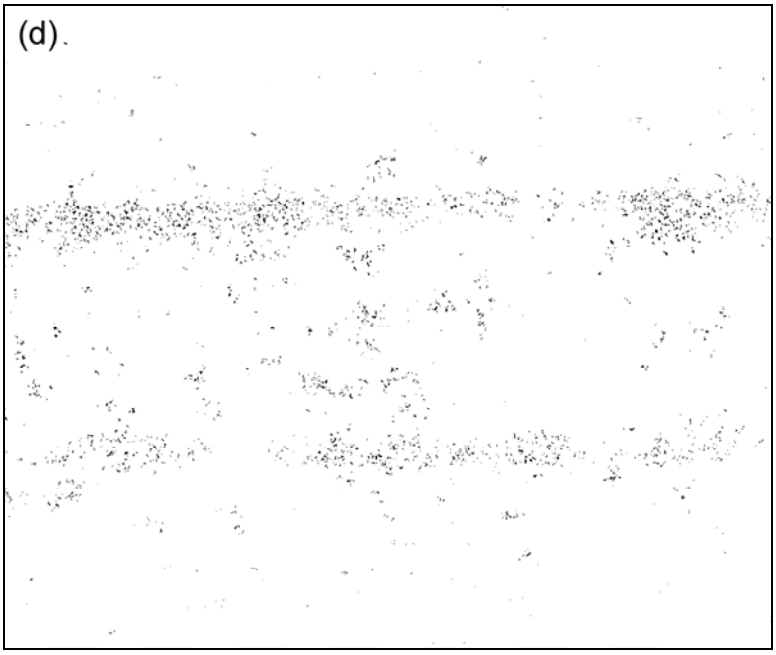

Figure 3.7: (c) the image containing only the gas pores, and (d) the image containing only shrinkage pores.

3.4 Three-Dimensional Microstructure Reconstruction

The three-dimensional microstructure reconstructions were carried for selected microstructures of high-pressure die-cast AM50 and AM60 Mg-alloys using montage serial sectioning technique. The metallographic specimens were prepared without etching using general polishing procedures described earlier.

3.4.1 Montage Serial Sectioning

To generate a large volume of 3D microstructure at high resolution, one may first reconstruct a small microstructural volume such as the one in Figure 3.8a, and then reconstruct many contiguous small volumes surrounding it, perfectly match their boundaries, and paste them together to generate a large microstructural volume, as shown in Figure 3.8b. First a "montage" of 225 (or more if necessary) contiguous microstructural fields observed at a high magnification (200× for the present microstructure) is created by using the large-area high-resolution montage procedure. Figure 3.9a shows such a montage of 225 fields of view (FOV), which has been compressed for display. Each region of this montage has a high resolution of the image shown in Figure 3.9b. Therefore, montage is a microstructural image of a large area (~12.4 mm^2) having a high resolution. In the present work, image analysis was performed on KS-400 image analysis system from Kontron, Inc. However, several other commercial image analysis systems also have the required capabilities. The computer codes for creating the montage were written in a language similar to C^{++} in a platform provided by the image analysis software (KS-400).

Once the montage of the first serial section is created and stored in the computer memory, small thickness of the specimen is removed (about 1 micron) by polishing, and then a second montage is created at the region exactly below that in the first metallographic plane. In the present study, this polish-montage-polish procedure was repeated to obtain stack of 100 montage serial sections.

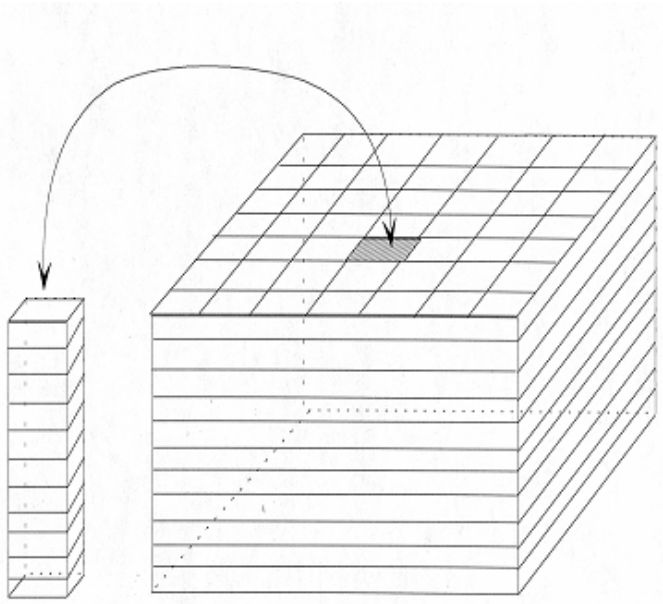

Figure 3.8: (a) Small microstructural volume element constructed from a stack consisting of one field of view in each serial section. (b) Large volume of microstructure obtained from contiguous small volumes such as those in (a) or by using montage serial sectioning.

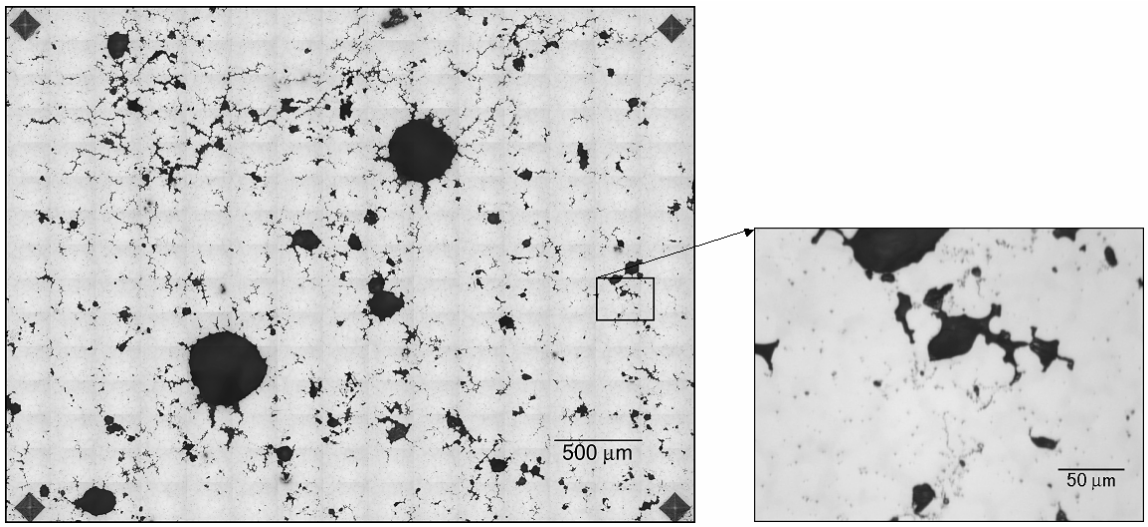

Figure 3.9: (a) Montage of 225 fields of view covering an area of 12.4 mm^2 created by matching contiguous microstructural fields grabbed at a resolution of 0.5 μm. The montage is digitally compressed for presentation. Each field of view of the montage has been grabbed at the resolution of the image shown in (b).

Micro-hardness indents were used to locate the exact region of interest in successive serial sections and to measure the distance between consecutive serial sections [53]. As the geometry of the indenter is accurately known as shown in Figure 3.10, the decrease in the length of the diagonal of the micro-hardness indent yields the distance between the two consecutive serial sections in a straightforward manner ($h \cong D/7$).

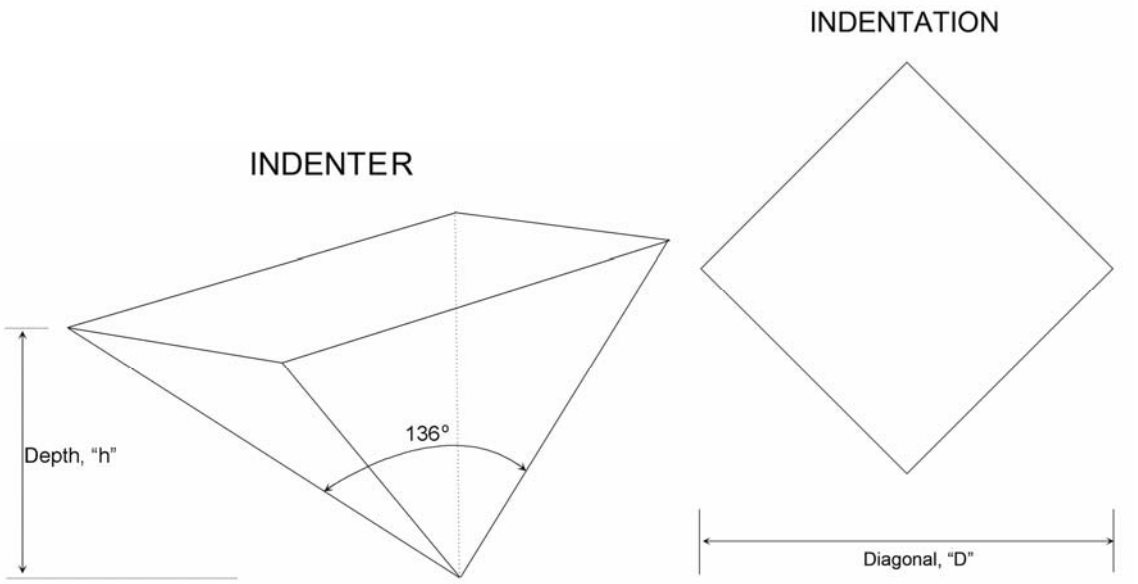

Figure 3.10: Geometry of Vickers-hardness indenter.

An important practical problem in the reconstruction of 3D microstructure from serial sections is that the successive serial sections may not be precisely aligned; they may have some transnational and rotational displacement with respect to each other. In the present study, in spite of adjusting the microscope stage, the montages of the consecutive serial sections were often displaced by about ±10 pixels and ±5 degrees, and therefore, it was essential to precisely align successive serial sections. Alignment can be achieved by locating two common points (in the present case, micro-hardness indents were used for this purpose) in the two consecutive serial sections and translating one image until the first common point is aligned in the two images. Then the image is

rotated about this point until the second common point is also aligned. In the present case, this was accomplished by using 3D image analysis software KS400 in which the images of the montage were digitally translated and rotated until they were exactly aligned to the respective previous sections.

3.4.2 Reconstruction and Visualization of Three-Dimensional Microstructure

The stack of aligned serial sections essentially constitutes a volume image data set similar to those encountered in X-ray computed tomography and magnetic resonance imaging (MRI). The steps are involved in the 3D visualization of such data sets are as follows.

- Data generation (in the present case, serial sections)
- Pre-processing such as image alignment, grid regularization, image enhancement, and interpolation
- Rendering of 3D images

The 3D microstructure visualization can be achieved either by surface rendering or by volume rendering. Surface rendering involves rendering of the iso-surface of the region of interest (ROI) from the volume data, whereas the volume rendering is the rendering of all volume data by specifying opacity and color of each voxel (3D pixel). The surface rendering leads to reduction in the size of the data set because only the surface data are retained. The surface rendering requires fitting of a surface in the volume data. Numerous algorithms are available for surface rendering, including contour connecting algorithm [63] and marching cube algorithm [64]. In the present work, marching cube algorithm has been used for surface rendering of 3D microstructure. In the process of volume rendering, all voxels are visualized by specifying a mapping between rendered image intensity and voxel intensity. In the present work, ray-casting algorithm [65] has been used to for volume rendering of the microstructural images. The 3D image rendering was done by using image analysis software Voxblast 3.10.

3.5 Mechanical Tests

There have been numerous studies on the effects of porosity on the mechanical properties of high-pressure die-cast Mg-alloys. However, none of these investigations have addressed the following issues.

- What are the reasons for the observed variability in the important fracture sensitive mechanical properties such as ductility?
- What are the correlations between the variability in the properties and the variability in the microstructure?
- How can the variability in the mechanical properties of the cast components be predicted and reduced?
- What are the effects of porosity and/or other phases, if any, on the fatigue properties other than on the uniaxial tensile properties?

To address some of these issues, in the present work, important fracture sensitive mechanical properties of AM50 and AM60 alloys have been quantitatively correlated to the microstructural and fractographic parameters. The mechanical tests were performed at the Westmoreland Testing and Research Laboratories, and the microstructural analysis has been performed at Georgia Tech.

3.5.1 Uniaxial Tensile Tests

Although amount of porosity in the cast microstructure appears to adversely affect the tensile ductility of HPDC Mg-alloys, attempts to establish quantitative correlations between the average amount of porosity in the bulk microstructure and fracture sensitive properties such as strength or ductility have often failed. On the other hand, the amount of porosity observed in the fracture surfaces of tensile test specimens shows strong quantitative correlation with the fracture sensitive mechanical properties of HPDC AM50, AM60, and AZ91 Mg-alloys [13, 66, 67], which is similar to that observed in numerous

cast Al-alloys [68-70]. Consequently, in this contribution, quantitative fractographic techniques have been used to explore the correlations between the variability in the tensile ductility of AM50 HPDC Mg-alloy and the geometric attributes of the micro-porosity present in the corresponding tensile fracture surfaces at test temperature. Round tensile test specimens of 6.4 mm diameter as illustrated in Figure 3.11 were high-pressure die-cast using the liquid metal gate velocity at 55 m/s and solidification pressure of 540 bars. The die-casting was performed at Norsk Hydro, Sweden.

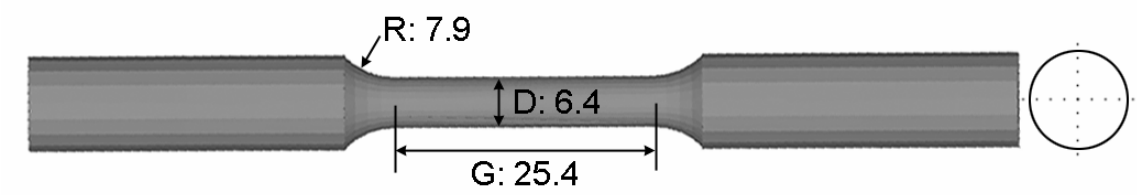

Figure 3.11: Geometry of the tensile test specimens.

The die cavity was at atmospheric pressure (no vacuum was used) before the fill. The liquid alloy temperature was 680°C. The initial die temperature was 200°C, which increased to approximately 220°C during the solidification of the cast specimens. The fine-grained "skin" present at the external surfaces of the cast tensile test specimens was not machined off from the *gage section*, but the grip sections were machined to ensure proper dimensions and alignment during the testing. The tests were performed at the engineering strain rate of 8.3×10^{-3} percent per second at room temperature as per ASTM E21-92 (1998) standard. All the tensile tests were conducted by Westmoreland Mechanical Testing & Research Inc. At each temperature, the tests were performed on six specimens.

The specimens were mounted and polished using well-known metallographic procedures. The HPDC As-polished metallographic sections were used to measure the volume fraction and other attributes of porosity in the bulk microstructure using standard

stereological and digital image analysis techniques developed in this study. Fracture surfaces of the tensile test specimens were examined using a Hitachi S-4100 scanning electron microscope equipped with an energy dispersive x-ray analyzer.

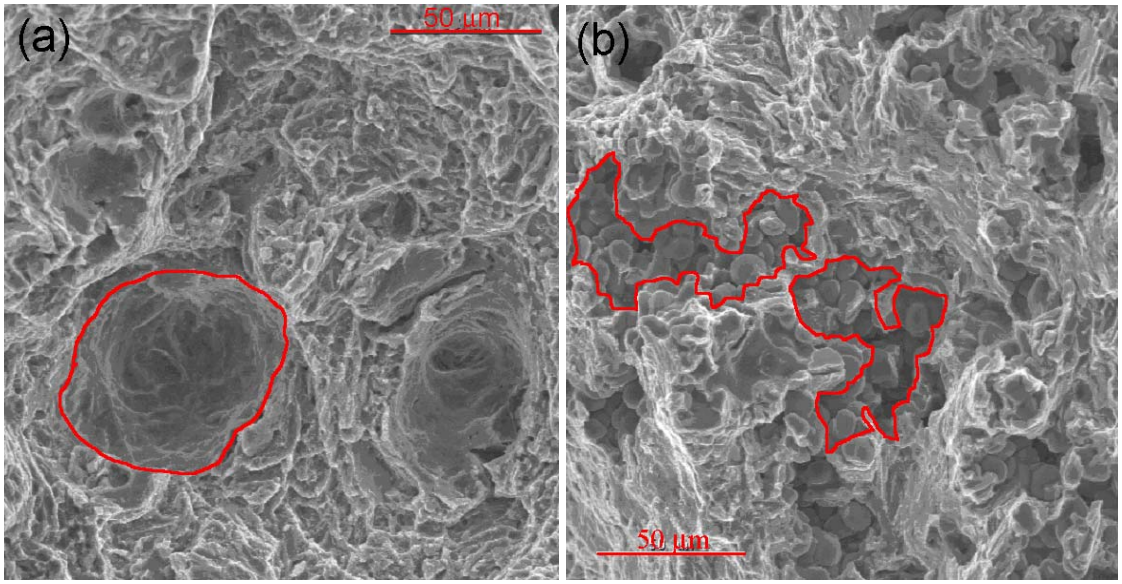

Figure 3.12: Typical SEM fractographs of a tensile fracture surface.

In these fracture surfaces, the pre-existing porosity can be detected due to presence of unfractured dendrites below the pores. The fracture surfaces contain shrinkage porosity as well as gas (air) porosity. The gas porosity is due to the entrapped air in the mold cavity as well as due to hydrogen and other gases dissolved in the liquid alloy. The porosity can be identified in the fracture surfaces due to the presence of intact (unfractured) dendrites below the pores. Thus, all the regions of the fracture surface that contain intact dendrites are essentially the areas occupied by either shrinkage pore or gas pores. One such region is outlined in Figure 3.12. The area fractions of porosity in the fracture surfaces were measured using well known quantitative fractographic techniques [71]. Entire fracture surfaces were scanned for these measurements.

3.5.2 Fatigue Test

For numerous structural automotive applications, fatigue resistance is of prime concern, since most of the components are subjected to cyclic loading conditions. Therefore, it is of interest to understand the effects of microstructure and microstructural defects on the fatigue behavior of HPDC Mg-alloys. In general, HPDC Mg-alloys contain considerable amount of micro-porosity [10, 11], and consequently, the effects of micro-porosity on the fatigue behavior of have been studied by numerous researchers [72, 73]. These investigations show that the fatigue cracks often initiate at the micro-pores, and propagate along the inter-dendritic regions as well as through the dendrites.

The experiments were performed on high-pressure die-cast commercial AM60 rectangular thin plates. The fatigue tests were performed on dog bone type fatigue test specimens machined from AM60 thin plates. The fatigue specimens were fabricated without removal of cast surfaces (skin) of the plates. Specimens were tested at room temperature using a triangular waveform at a frequency of 30 cpm with an R-ratio of –1. Specimens were switched to load control after reaching 43,200 cycles using a frequency of 10Hz. The tests were performed at room temperature at strain amplitudes ranging from 0.1% to 0.6%. The tests were carried out on the specimens fabricated from two sets of plates (B and W) high-pressure die-cast using different combinations of process parameters. All fatigue tests were performed at the Westmoreland Testing and Research Laboratories.

CHAPTER 4

RESULTS AND DISCUSSIONS

The central objective of this research is to study the relationships between processing, microstructure, and mechanical properties of important high-pressure die-cast (HPDC) Mg-alloys. For this purpose, a series of experiments were performed to generate a set of HPDC microstructures and these microstructures have been quantitatively characterized as reported in chapter 2 and 3. In addition, computer simulations of the HPDC process as well as mechanical response of typical HPDC microstructures have been conducted, which are reported in chapter 4. The experimental quantitative data on the microstructural geometry and its relationships with the HPDC process parameters, and the results of the numerical simulations are analyzed in detail in this chapter to arrive at an in-depth understanding of how HPDC processing determines the microstructure and how the microstructure in turn affects the mechanical properties of important Mg-alloys. The next section of the chapter describes the detailed quantitative microstructural data, which is followed by analysis of the relationships between the HPDC process parameters and the microstructural parameters; the results of the numerical simulations are presented in the subsequent sections.

4.1 Effects of Process Parameters on Microstructure

4.1.1 Introduction

In this research, a detailed systematic investigation has been carried out on the effects of HPDC process parameters on the volume fraction of gas and shrinkage pores, their size distributions, and their spatial variations in the microstructures. In particular, the effects of gate velocity (injection rate), intensification, and melt temperature on these attributes of the pores are quantitatively characterized in AM50 and AM60 Mg-alloys. To

the best knowledge of the author, this is the first investigation where the effects of these individual process parameters on the microstructural porosity have been clearly deconvoluted. The details of these HPDC experiments, and the images analysis and stereology based procedures for microstructure quantification are given in chapter 3. The porosity measurements have been performed as a function of the distance along the length, width, and thickness of the cast plates to obtain detailed porosity distribution maps and the dependence of these distributions on the individual process parameters. Further, in addition to pore volume fractions, the average size, size distribution, and other attributes of the pore geometry have also been measured and correlated to the process parameters. These detailed porosity data are useful for establishing the correlations between the process parameters and the amounts of gas and shrinkage porosity, average gas pore size, and distributions.

4.1.2 Effects of Process Conditions on the Porosity in AM50 Thick Plates

The matrix of the process parameters investigated in this work is given in Table 3.2. This design of experiments permits deconvolution of the individual effects of intensification (plates I and W), gate velocity (plates G and W), and melt temperature (plates M and W) on the pore geometry in the cast microstructures of the high-pressure die-cast AM50 Mg-alloy.

4.1.2.1 Microstructural Observations

Figure 4.1 shows the unetched microstructural montages depicting gas and shrinkage porosity in plates I, G, M, and W, at the same location in each plate. In these montages, the Y-direction is the thickness direction of the plate and the montages cover the complete thickness (14.3 mm) of the plate. Observe that most of the gas pores (particularly the large ones) are located in the middle one-third of the plate thickness; the amount of gas porosity is quite small near the plate surfaces at the top and bottom.

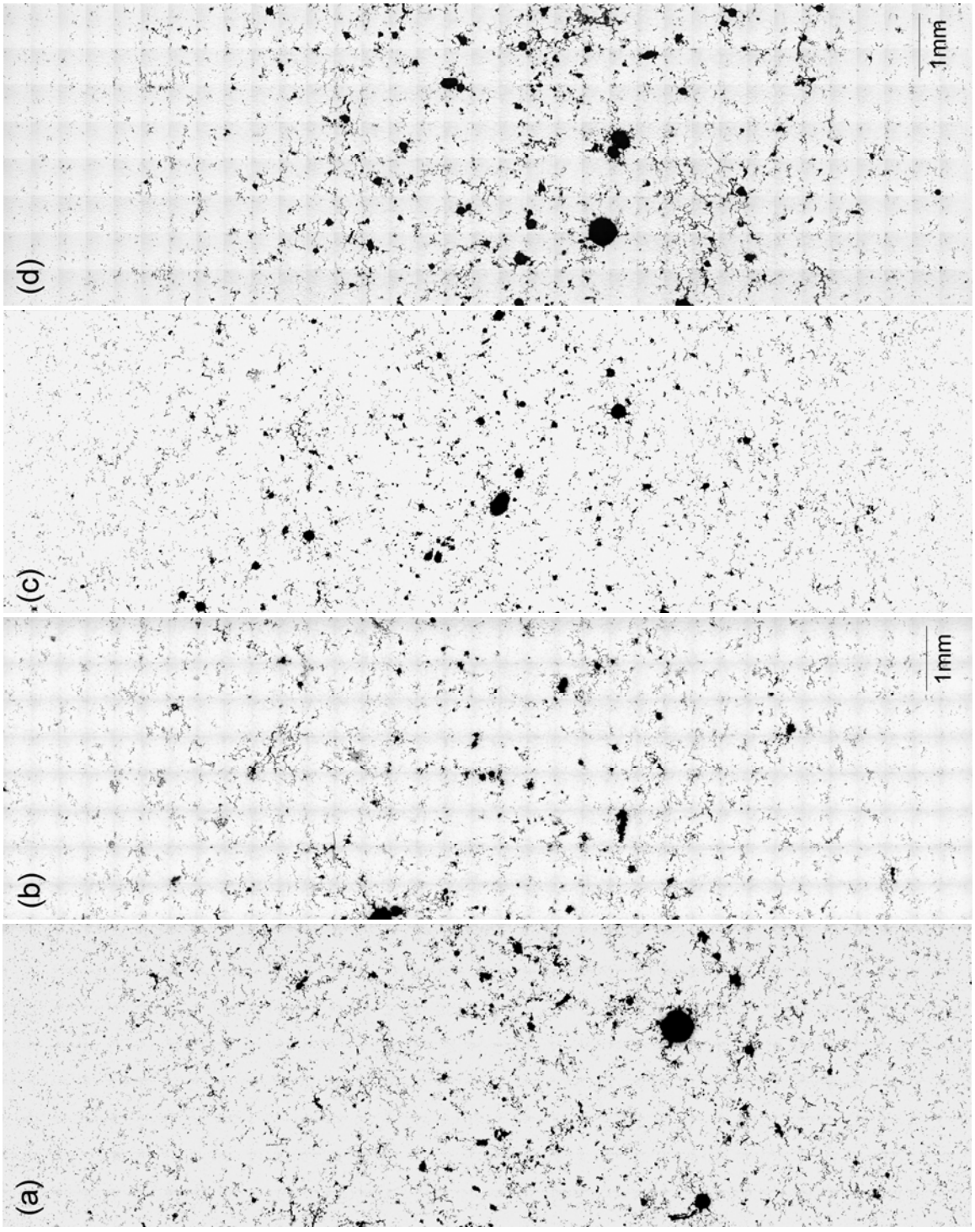

Figure 4.1: Gray scale montages of (a) plate I, (b) plate G, (c) plate M, and (d) plate (W).

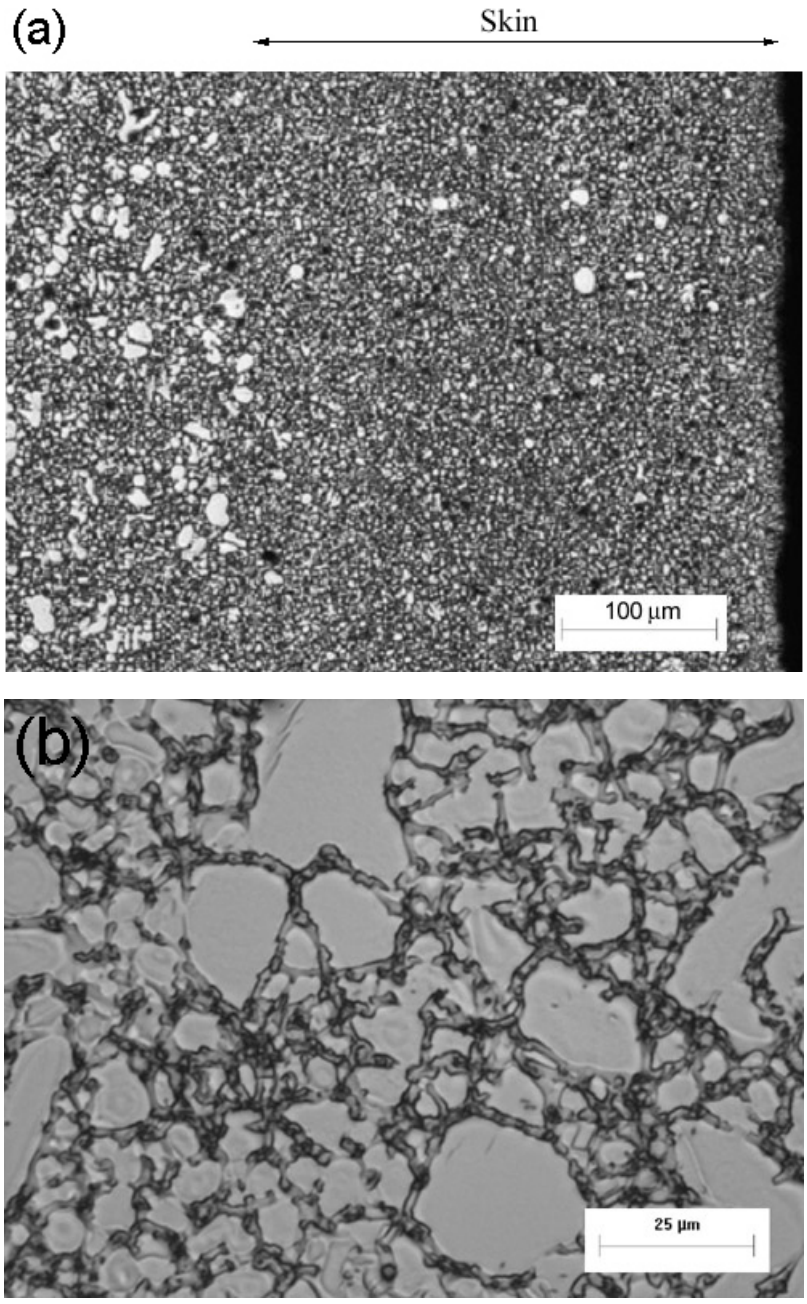

Figure 4.2: (a) Fine-grained skin region at the cast surface containing a very low amount of gas porosity. (b) Typical cast microstructure showing cored Mg-rich dendrites and $Mg_{17}Al_{12}$ eutectic phase in the inter-dendritic regions.

This is expected because a rapidly solidified fine-grained “skin” region is present below the cast surfaces (see etched microstructure in Figure 4.2a), as the skin solidifies, the gas pores are pushed to the interior. On the other hand, the pre-solidified dendrites

(i.e., those formed in the shot sleeve) present in the center lead to the formation of a second solidification front that moves from the center to the surface. The junction of these two solidification fronts often contains bands containing highly clustered pores, particularly in castings having small section thickness. Such porosity bands are not observed in the present cast plates due to their significantly large thickness (14.3mm); rather, the gas pores are pushed towards the middle of the thickness as observed. Interestingly, in the present cast plates, the shrinkage pores are uniformly distributed across the thickness of the plates. Further, the large gas pores are usually surrounded by shrinkage porosity, but the shrinkage pores do not always have gas pores around them.

Table 4.1. Average volume percentage of gas, shrinkage, and total porosity.

Plate ID	Gate Velocity (m/sec)	Intensification	Melt Temp (ºC)	Gas (%)	Shrinkage (%)	Total (%)
B	35	On	682	1.07	0.85	1.92
I	56	On	705	1.23	0.90	2.13
G	35	Off	705	1.20	0.58	1.78
M	56	Off	682	1.34	0.91	2.25
W	56	Off	705	1.93	0.87	2.80

Table 4.1 summarizes the average volume percentage of gas, shrinkage, and total porosity. This Table demonstrates low gate velocity, or low melt temperature, or application of intensification pressure can reduce the total amount of porosity, i.e., each of these individual process parameters or their combinations can be optimized to reduce the total amount of porosity in the HPDC microstructure of AM50 alloy. The decrease in the total amount of porosity is mainly due to the reduction of gas pores, whereas the amount of shrinkage porosity does not vary significantly with the process conditions except in plate G. More detail observations are described in the following sub-sections.

4.1.2.2 Effects of Intensification on the Porosity

The plates I and W have been high-pressure die-cast with the same values of all process parameters except the intensification: the intensification pressure was applied for casting plate I, whereas it was not applied for casting plate W. Therefore, the differences in the porosity attributes in these two plates essentially reflect the effect of intensification pressure on the porosity in this high-pressure die-cast AM50-alloy. Figure 4.3 shows plots of the spatial distribution of total porosity in the three-dimensional space of the cast plate I (a) and W (b) (see Table 3.2 for the process parameters, and Figure 3.1 for the sampling scheme). The color represents the percentage of porosity at different locations along the length, width, and thickness directions of the plate. Figure 5.4 shows the corresponding plots for the spatial distribution of gas porosity and Figure 4.5 shows the plots for shrinkage porosity. The data in Figure 4.5 reveal that the shrinkage porosity is *uniformly* distributed at different locations in the plate, whereas Figure 4.4 shows that the gas porosity distribution is spatially non-uniform; the majority of the gas pores are located in the middle one third of the plate thickness and also away from the edges of the plate along the width direction. These Figures clearly show that the decrease in the total amount of porosity is mainly due to the significant reduction of the amount of gas pores. Figure 4.6 shows the spatial location of each large pore (pores larger than 100 μm diameter) in the plate I (a) and plate W (b). Note that the gaps between the points along the plate length and width are because of the fact that the porosity measurements were performed only at selected locations (see Figure 3.1) and should not be misconstrued as the absence of porosity at those locations. Observe that most of these large pores are located in the middle one third of the plate thickness and away from the plate edges in the width direction.

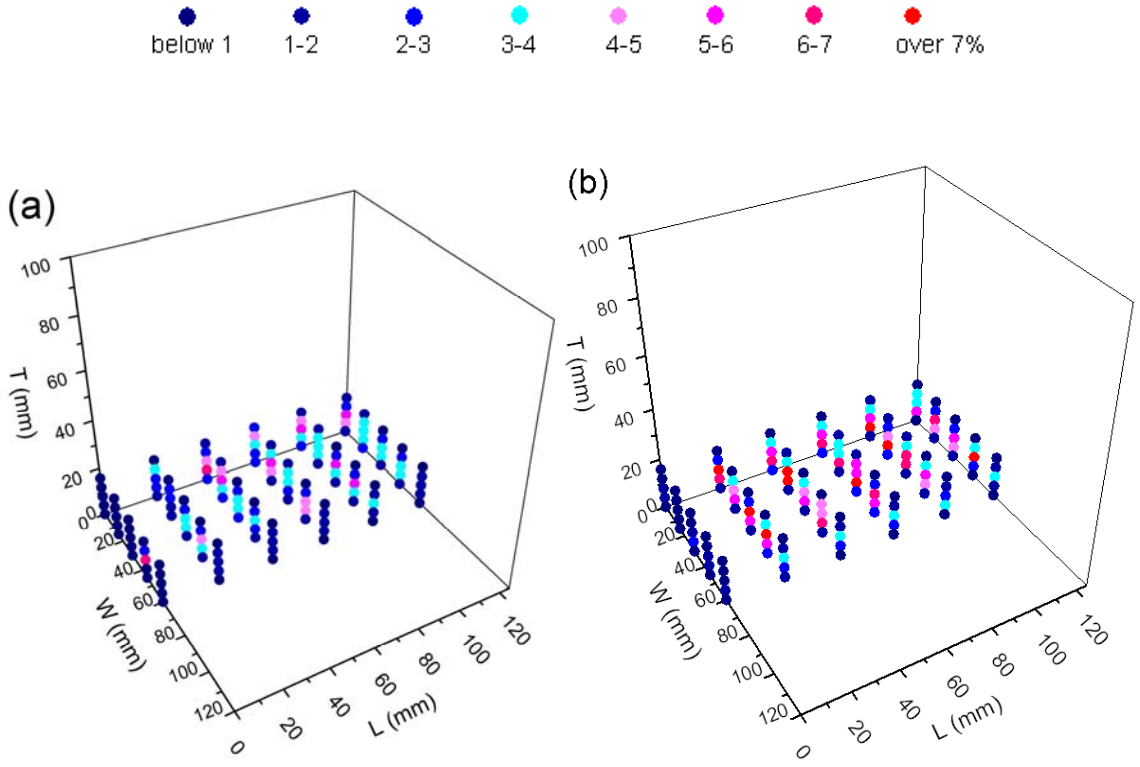

Figure 4.3: Spatial distributions of the percentage of total porosity of (a) plate I and (b) plate W at different locations along the length, width, and thickness of plates.

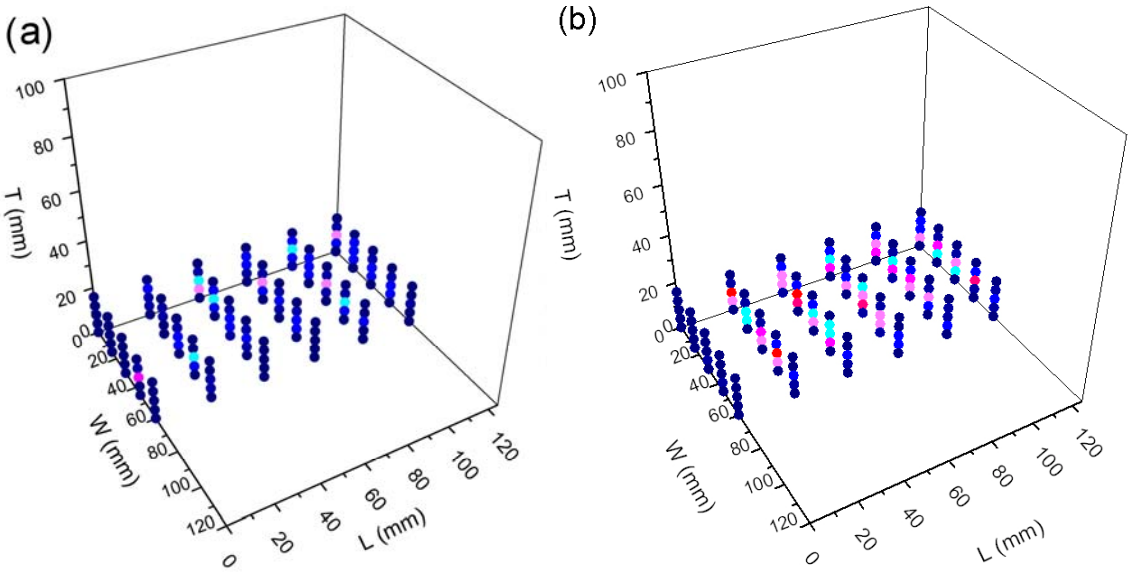

Figure 4.4: Spatial distributions of the percentage of gas porosity of (a) plate I and (b) plate W at different locations along the length, width, and thickness of plates.

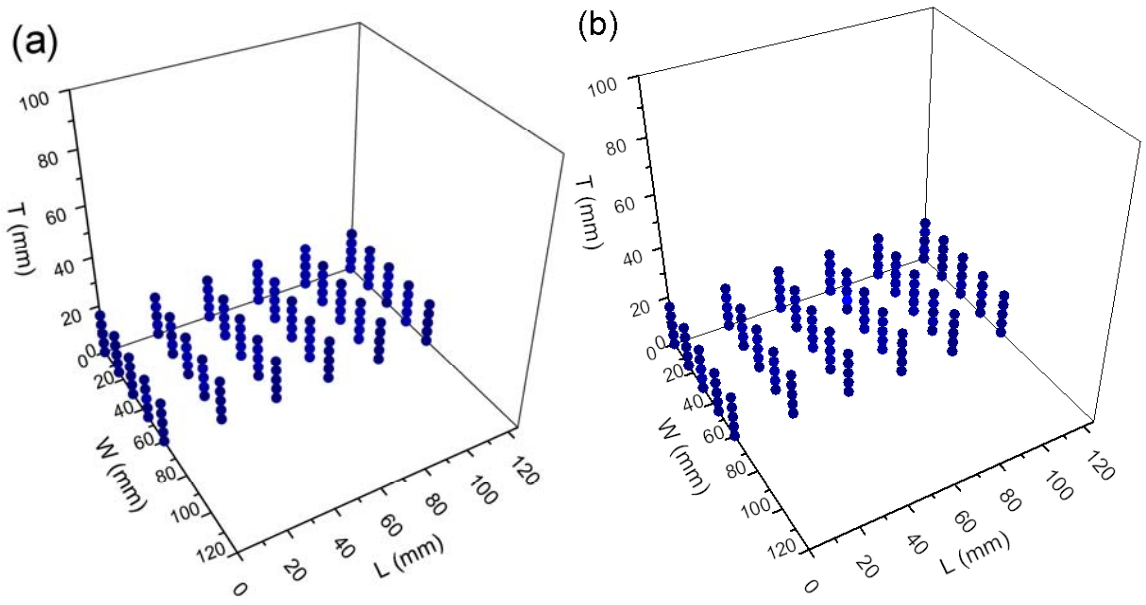

Figure 4.5: Spatial distributions of the percentage of shrinkage porosity of (a) plate I and (b) plate W at different locations along the length, width, and thickness of plates.

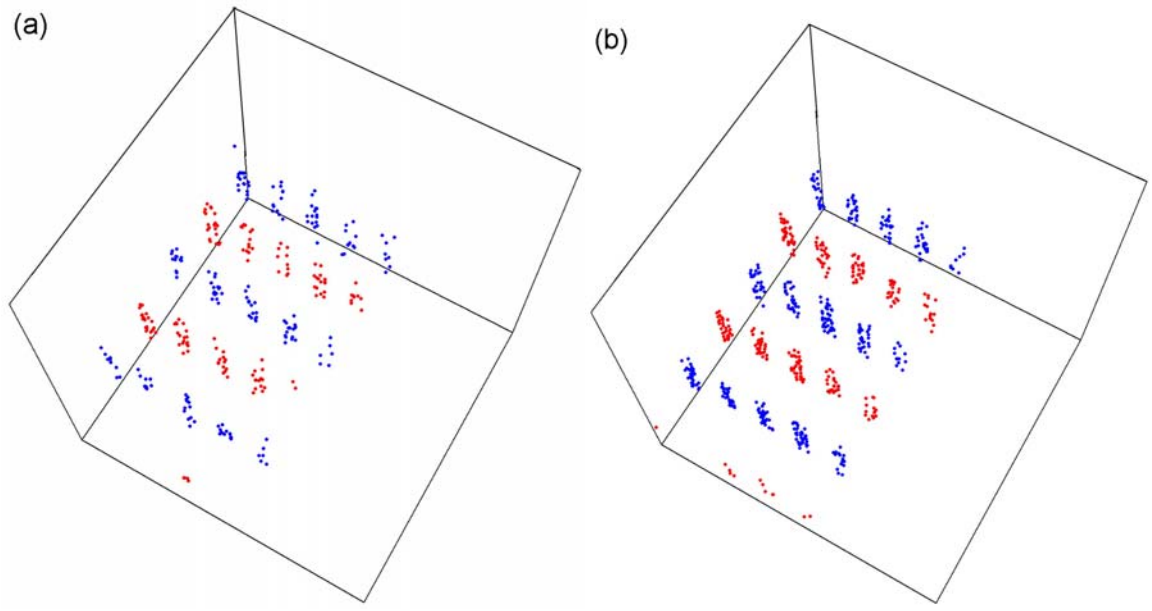

Figure 4.6: Location of each pore larger than 100 μm diameter in (a) plate I and (b) plate W. Note that in this figure each "dot" represents the location of a large pore.

Therefore, the non-uniform spatial distribution of the percentage of gas porosity (and total porosity) is primarily due to the non-uniform spatial arrangement of the gas pores having diameters larger than 100 μm. These general trends concerning spatial distribution of pores are also observed in the plate casts with other combinations of the process parameters, but the amounts of gas and shrinkage pores, pore size distributions, etc., depend on the process parameters.

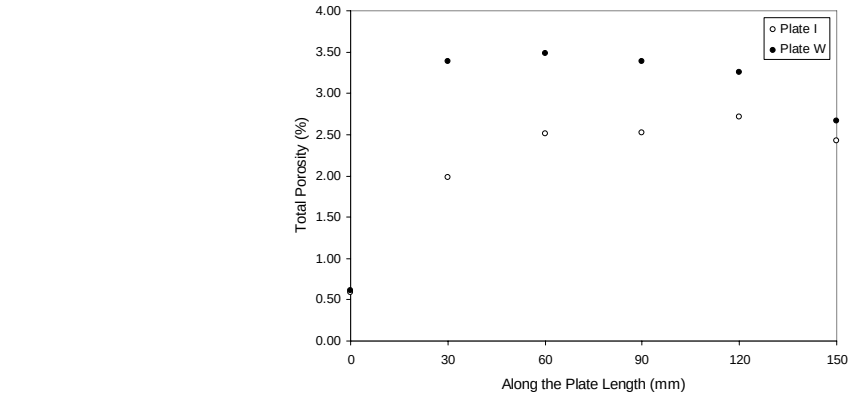

(a)

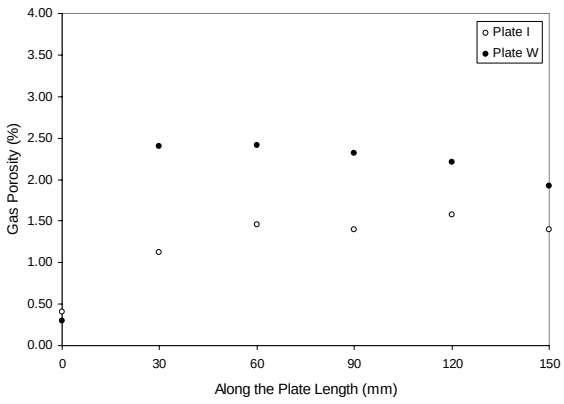

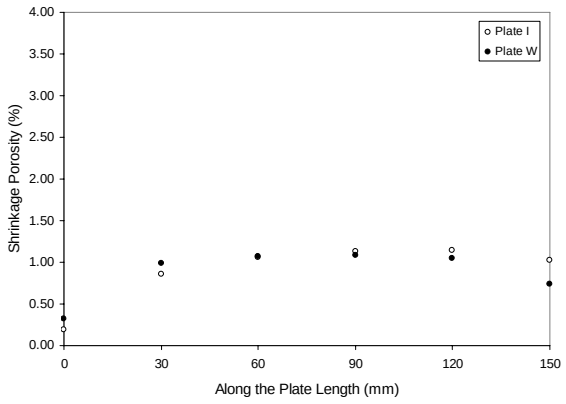

(b) (c)

Figure 4.7: Plot of the percentage of (a) total porosity, (b) gas, and (c) shrinkage porosity as a function of the distance along the plate length.

Figure 4.7a shows the variation of the total porosity (gas and shrinkage) as a function of distance along the length of the plates. In this plot, the x-axis origin is at the location of the liquid metal inlet. These data are obtained by averaging the percentage porosity over the width and thickness at a given location along the plate length. Observe that at every location along the length of the plates, the percentage of the total porosity in the I plates is significantly lower than that at the corresponding location in the plate W (no intensification). Figure 4.7b shows the variation of the percentage of the gas (air) pores with the distance along the length of the two types of plates. Again, at most of the locations along the length of the plates, the percentage of gas (air) porosity in the I plates is significantly lower than that at the corresponding location in the W plates. This is because the intensification pressure compresses the gas pores, and consequently, the reduction in the sizes (volumes) of the pores leads to the lower volume percentage of the gas porosity. It is of interest to know if the intensification pressure decreases the amount of shrinkage porosity as well. Figure 4.7c shows the variation of the percentage of shrinkage porosity as a function of distance along the length of the plates. It is interesting to note that at all locations along the length of the plate, there is no significant difference in the amount of shrinkage porosity in the two plates. Therefore, the application of intensification pressure does not appear to decrease the amount of shrinkage porosity, but it significantly decreases the gas porosity. This result is somewhat surprising because the incremental pressure experienced by the liquid metal due to intensification should facilitate the feeding in the inter-dendritic channels, which may then lead to a decrease in the shrinkage porosity. It is likely that in these relatively thick plates (14.3 mm thickness), a higher intensification pressure may be essential to decrease the amount of shrinkage porosity significantly.

As the intensification pressure may compress the gas pores, and consequently, decrease their size, it is of interest to examine the effects of intensification on the size distribution of the gas pores. Figure 4.8a shows the conventional number distribution of

the gas pores in the plates I and W. On the other hand, Figure 4.8b shows the area fraction distribution of the gas pores in the same two plates, which clearly brings out the contribution of the large pores as well as the effect of intensification.

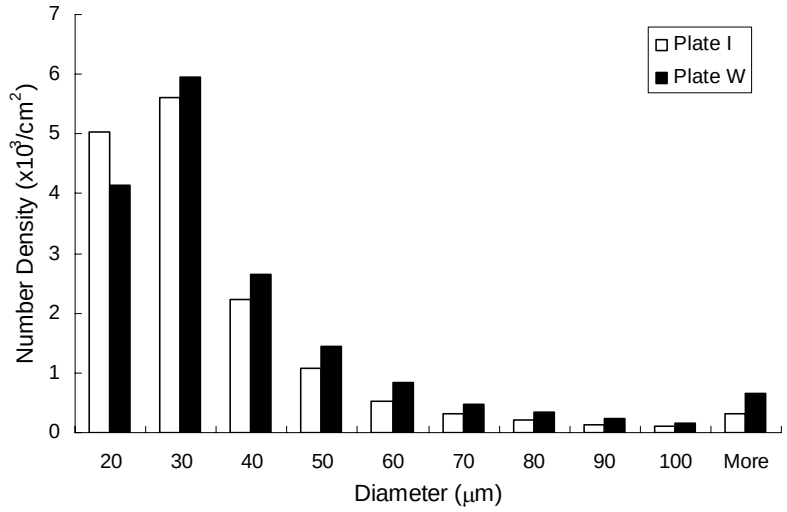

(a)

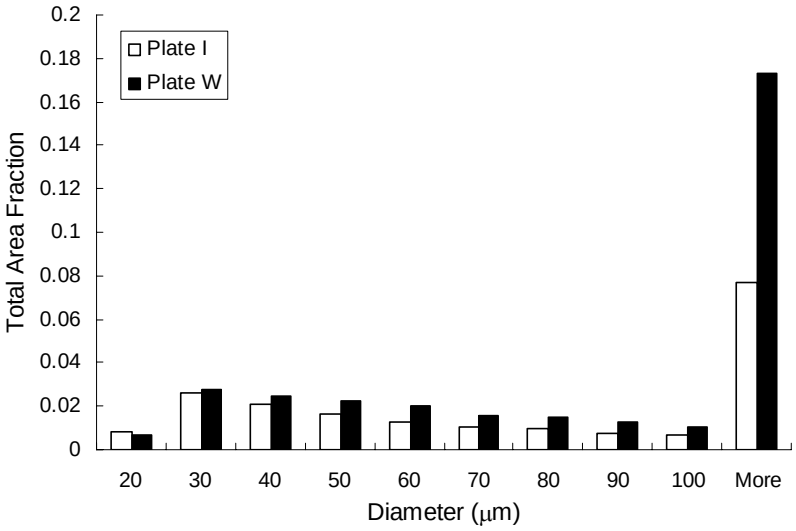

(b)

Figure 4.8: (a) Number based size distribution of gas pores in plates I and W. (b) Area fraction distribution of gas pores in plates I and W. The Y-axis is the area fraction of the metallographic plane occupied by the gas pores of different sizes.

In Figure 4.8b, the Y-axis is the area fraction of the metallographic plane occupied by the pores in a given size range, and therefore, it is the contribution of the pores in the given size range to the total amount (overall area fraction or percentage) of the gas porosity. Observe that (1) most of the overall amount (percentage) of the gas porosity resides in the pores with diameters larger than 100 μm, although the number density of such pores is quite small (Figure 4.8a), and (2) the intensification substantially decreases the area fraction of the metallographic plane occupied by pores larger than 100 μm in diameter. There is no significant difference in the area fraction distribution of pores smaller than 100 μm in diameter in the two plates. Therefore, the intensification pressure reduces the overall gas porosity primarily through reduction of the number density and area fraction contribution from the large pores, which can occur either via compression of the large pores and/or their break up into smaller pores.

4.1.2.3 Effects of Gate Velocity on the Porosity

The plates G and W have been high-pressure die-cast with the same values of all high-pressure die casting process parameters *except* the gate velocity. Therefore, the differences in the micro-porosity attributes in these two plates essentially reflect the effect of gate velocity. Figure 4.9 shows plots of the spatial distribution of gas porosity in the three-dimensional space of the cast plate G (a) and W (b). These general trends of porosity distribution are similar to all the casting plates and clearly show that the decrease in the total amount of porosity is mainly due to the significant reduction of the amount of gas pores. Figure 4.10 shows the spatial location of each large pore (pores larger than 100 μm diameter) in the plate G (a) and plate W (b). In a similar way to Figure 4.6, decrease in the liquid melt gate velocity significantly reduces the number density of large gas pores having diameters larger than 100 μm.

The data in Figure 4.11a have been obtained by averaging the percentage of porosity over the width and thickness at a given location along the plate length.

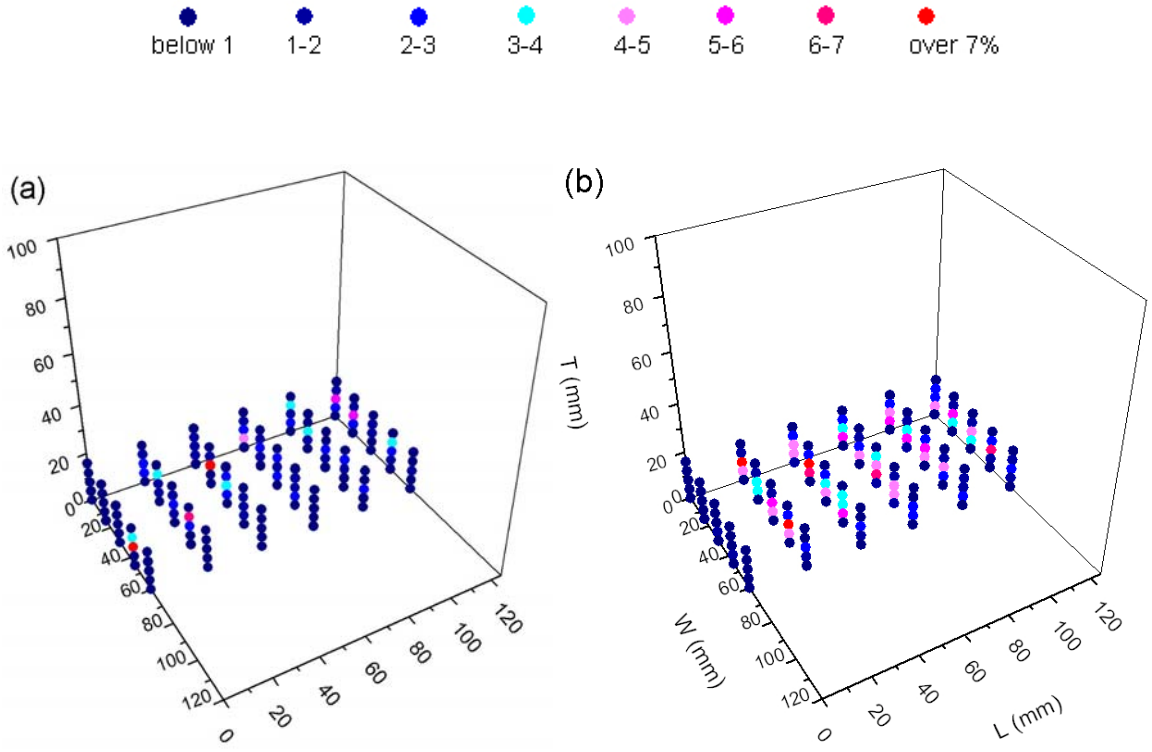

Figure 4.9: Spatial distributions of the percentage of gas porosity of (a) plate G and (b) plate W at different locations along the length, width, and thickness of plates.

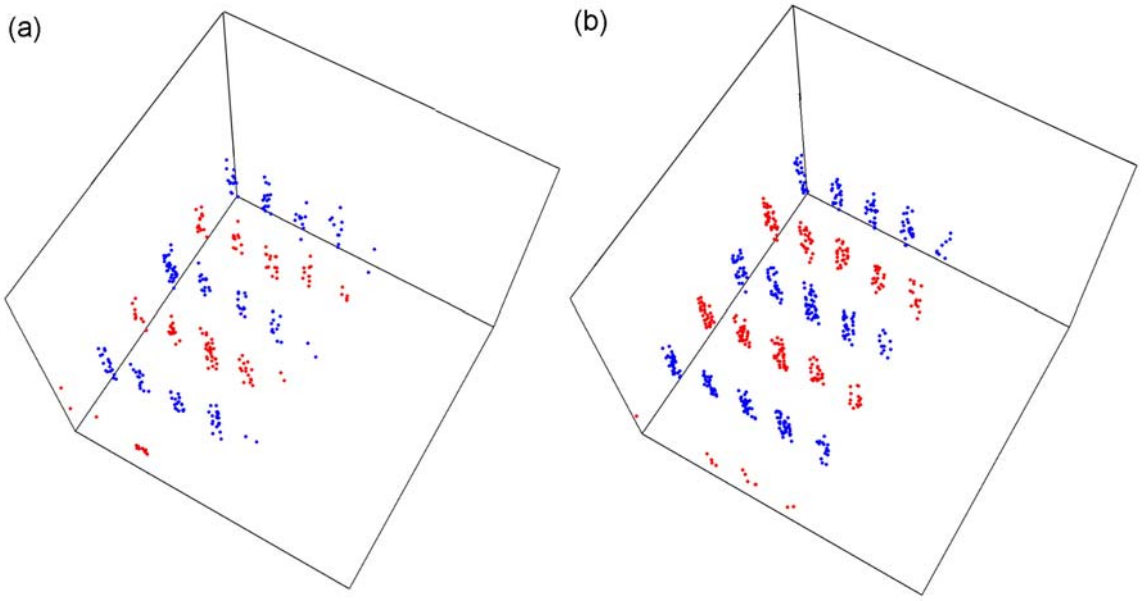

Figure 4.10: Location of each pore larger than 100 μm diameter in (a) plate G and (b) plate W.

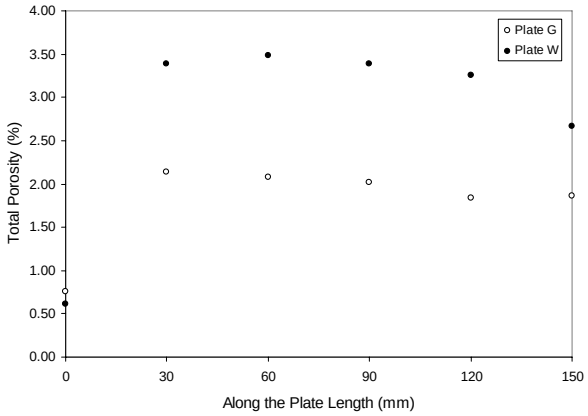

(a)

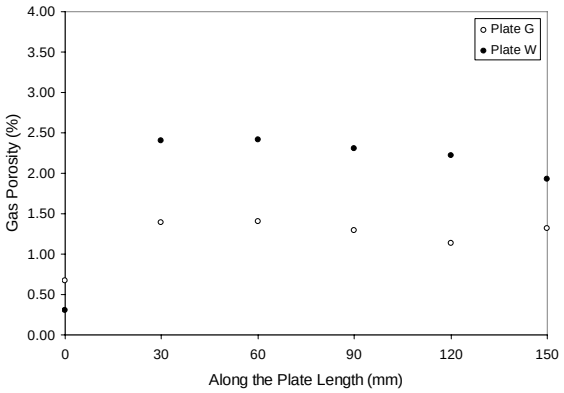

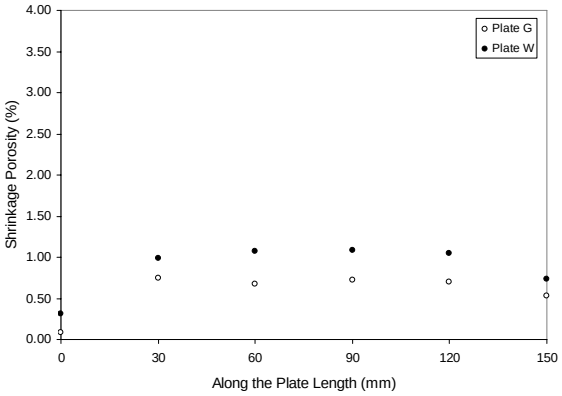

(b) (c)

Figure 4.11: Plot of the percentage of (a) total porosity, (b) gas, and (c) shrinkage porosity as a function of the distance along the plate length.

Observe that at almost every location along the length of the plates, the percentage of total porosity in the G plate cast at a gate velocity of 35 m/sec is significantly lower than that at the corresponding location in the W plate cast at a 55 m/sec gate velocity.

This can be explained by the reduction of liquid melt turbulence caused by the slower gate velocity. Figure 4.11b shows the variation of the percentage of the gas (air) pores with the distance along the length of the two types of plates. Again, at almost every location along the length of the plates, the percentage of gas (air) porosity in the G plate

is significantly lower than that at the corresponding location in the W plate. Figure 4.11c shows the variation of the percentage of shrinkage porosity as a function of the distance along the length of the plates. There is a consistent difference in the shrinkage porosity in the two plates: the lower gate velocity decreases the shrinkage porosity to some extent. Therefore, the decrease in the total amount of porosity arising from the lower gate velocity is also primarily due to the significant reduction of the amount of gas pores, with some contribution from the reduction in the shrinkage porosity.

Besides the average porosity variations at different locations of the plates, it is also important to analyze the changes of the pore size distribution to identify the pore size regimes that are affected by the gate velocity. Figure 4.12a compares the number distribution of pores in different size ranges. Interestingly, the decrease in the gate velocity from 55 m/sec (Plate W) to 35 m/sec (Plate G) uniformly decreases the number density of the gas pores in each size class to approximately the same extent. This is further confirmed by Figure 4.12b that shows the plots of the *area fraction* distribution of the gas pores having different sizes. Thus, the lower gate velocity decreases the area fraction of the gas pores in all size ranges. It follows that the intensification pressure and gate velocity affect the porosity in a somewhat different manner. The reduction in the gas porosity (and total porosity) due to the application of intensification pressure is primarily due to the decrease in the number density and area fraction of the large pores (pores larger than 100 μm diameter), whereas the decrease in the gas porosity caused by the decrease in the gate velocity is primarily through the decrease in the number density and area fraction of pores of all sizes (small as well as large pores). Further, application of the intensification with that pressure level has no effect on the shrinkage porosity, whereas the gate velocity has a measurable effect on the shrinkage porosity.

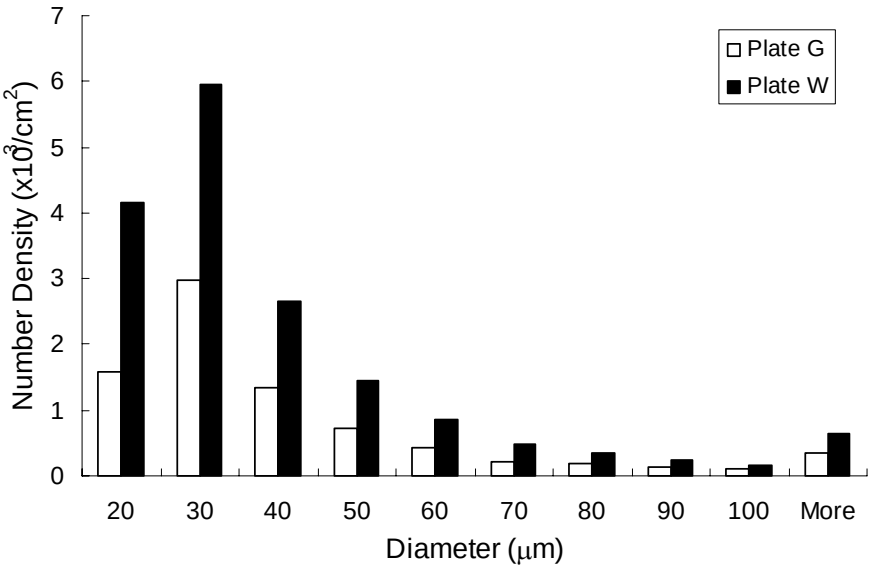

(a)

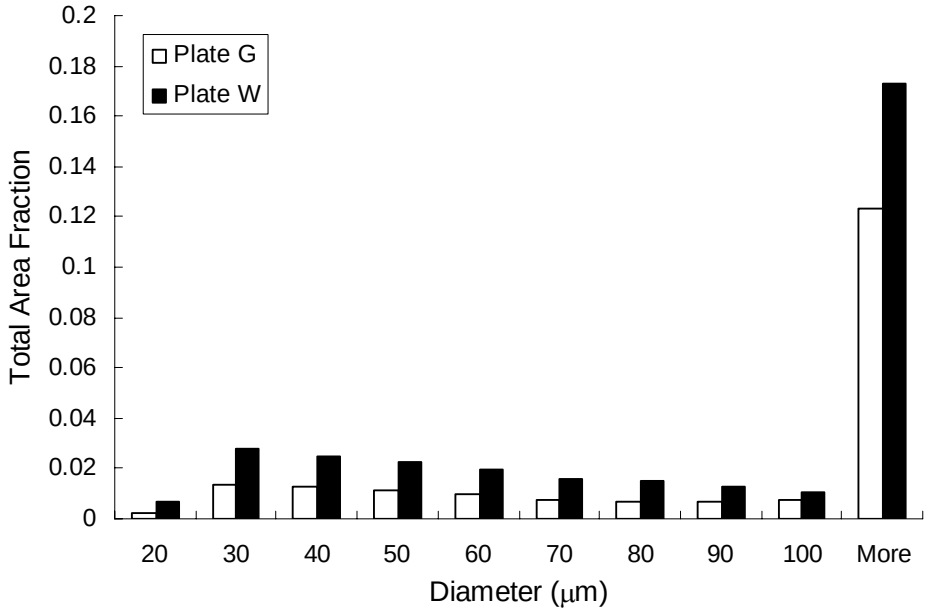

(b)

Figure 4.12: (a) Number based size distribution of gas pores in plates G and W. (b) Area fraction distribution of gas pores in plates G and W.

4.1.2.4 Effects of Liquid Melt Temperature on the Porosity

The plates M and W have been high-pressure die-cast with the same values of all high-pressure die casting process parameters *except* the melt temperature. Therefore, the differences in the micro-porosity attributes in these two plates essentially reflect the effect of melt temperature. Figure 4.13 shows plots of the spatial distribution of gas porosity in the three-dimensional space of the cast plate M (a) and W (b). These general trends of porosity distribution are similar to all the casting plates and clearly show that the decrease in the total amount of porosity is mainly due to the significant reduction of the amount of gas pores. Figure 4.14 shows the spatial location of each large pore (pores larger than 100 μm diameter) in the plate M (a) and plate W (b). In a similar way to Figure 4.6 and 4.10, decrease in liquid melt temperature significantly reduces the number density of large gas pores having diameters larger than 100 μm.

Figure 4.15a shows the variation of the total porosity (gas and shrinkage) as a function of the distance along the length of the plates. At every location along the length of the plates, the percentage of total porosity in the M plate cast at the melt temperature of 682 ºC is significantly lower than that at the corresponding location in the W plate cast at the melt temperature of 705 ºC. Figure 4.15b shows the variation of the percentage of the gas (air) pores with the distance along the length of the two types of plates. Again, at every location along the length of the plates, the percentage of gas (air) porosity in the M plate (cast at 682 ºC) is significantly lower than that at the corresponding location in the W plate (cast at 705 ºC). The lower melt temperature decreases the amount of dissolved gases in the melt and thereby decreases the gas porosity, rather than affecting the contribution to the gas porosity from the trapped air. Figure 4.15c shows the variation of the percentage of shrinkage porosity as a function of the distance along the length of the plates.

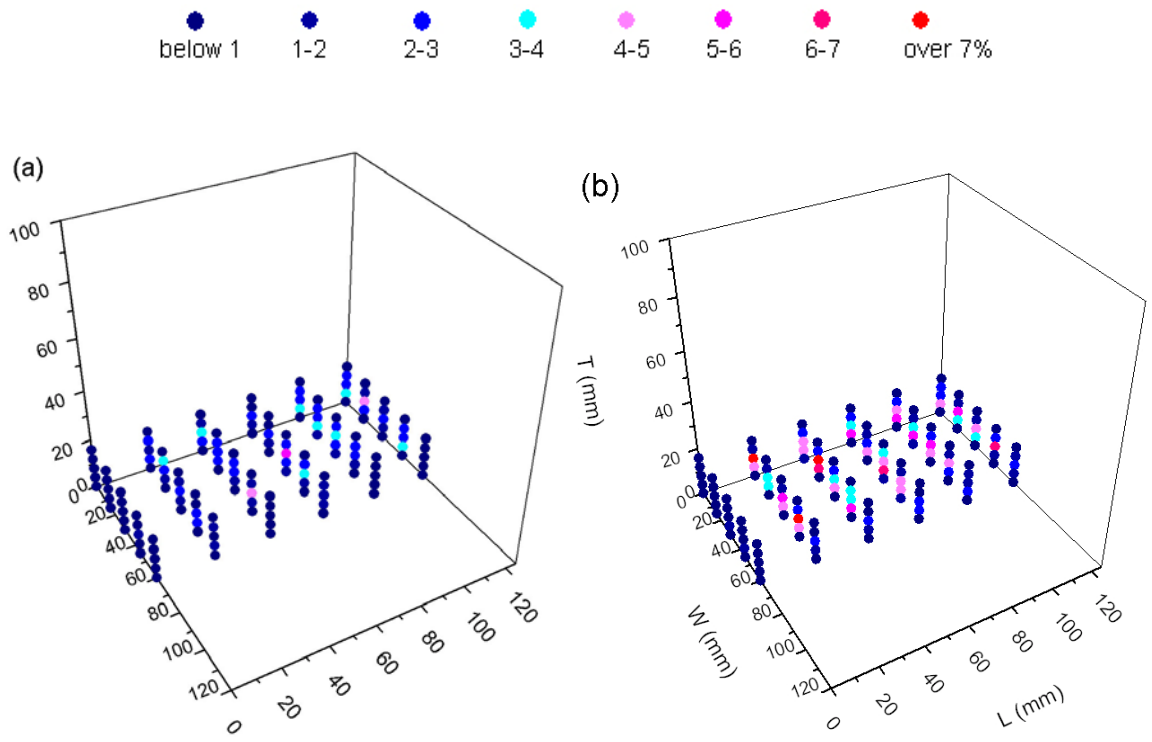

Figure 4.13: Spatial distributions of the percentage of gas porosity of (a) plate M and (b) plate W at different locations along the length, width, and thickness of plates.

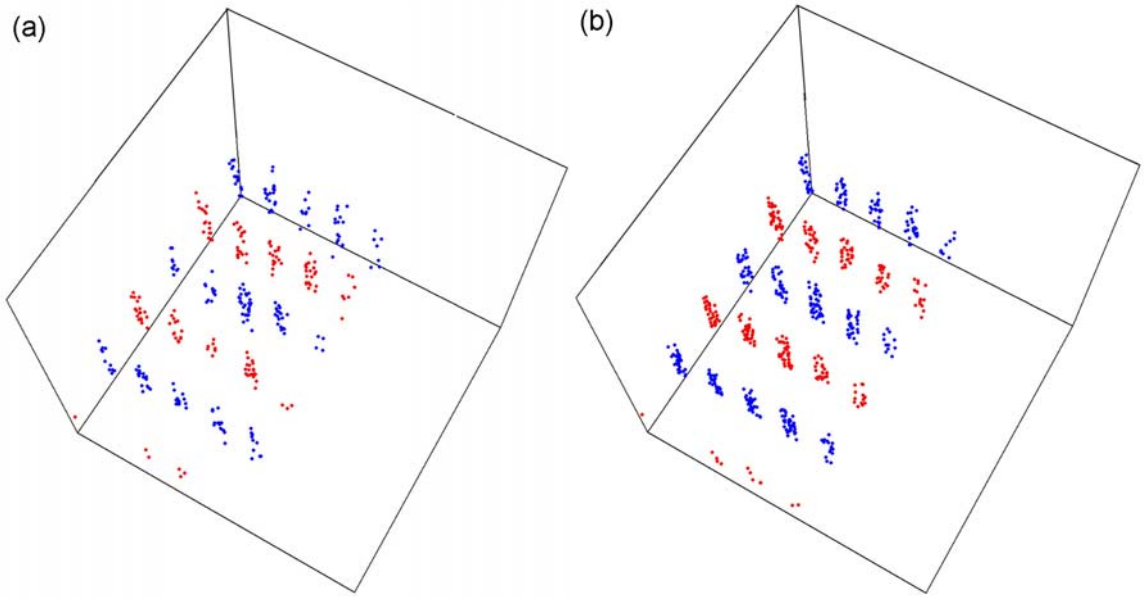

Figure 4.14: Location of each pore larger than 100 μm diameter in (a) plate M and (b) plate W.

There is no significant difference in the amount of shrinkage porosity at any given location in the two plates. Therefore, the melt temperature affects the amount of gas porosity but not the shrinkage porosity in this high-pressure die-cast AM50 alloy.

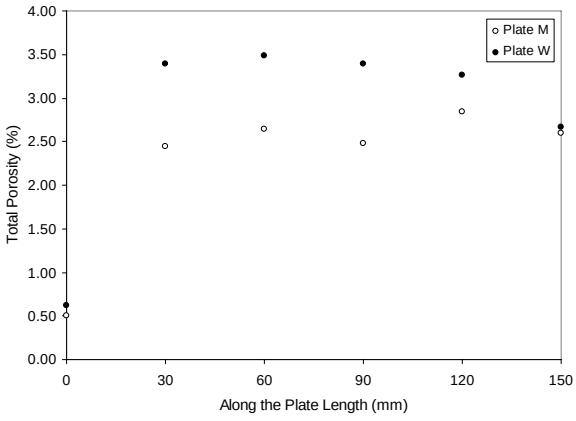

(a)

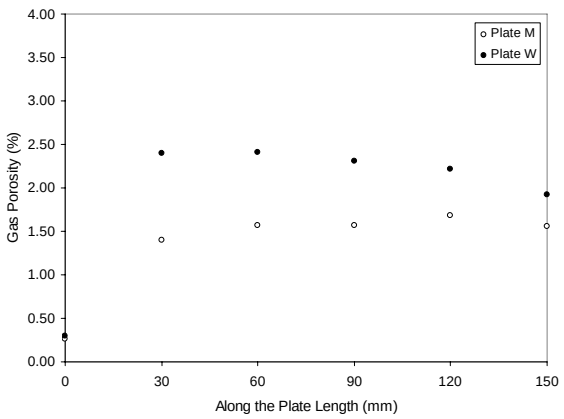

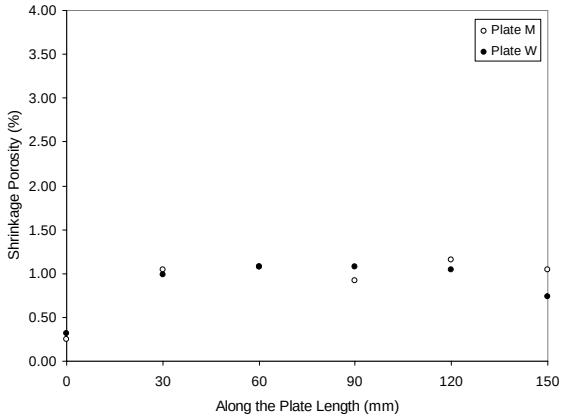

(b) (c)

Figure 4.15: Plot of the percentage of (a) total porosity, (b) gas, and (c) shrinkage porosity as a function of the distance along the plate length.

Figure 4.16a compares the number distribution of pores in different size ranges. Interestingly, the decrease in the melt temperature from 705 ºC (Plate W) to 682 ºC (Plate M) decreases the number density of the gas pores larger than 30 μm diameter to

approximately the same extent, which gives rise to a significant decrease in the area fraction contribution from the pores larger than 100 μm as illustrated in Figure 4.16b.

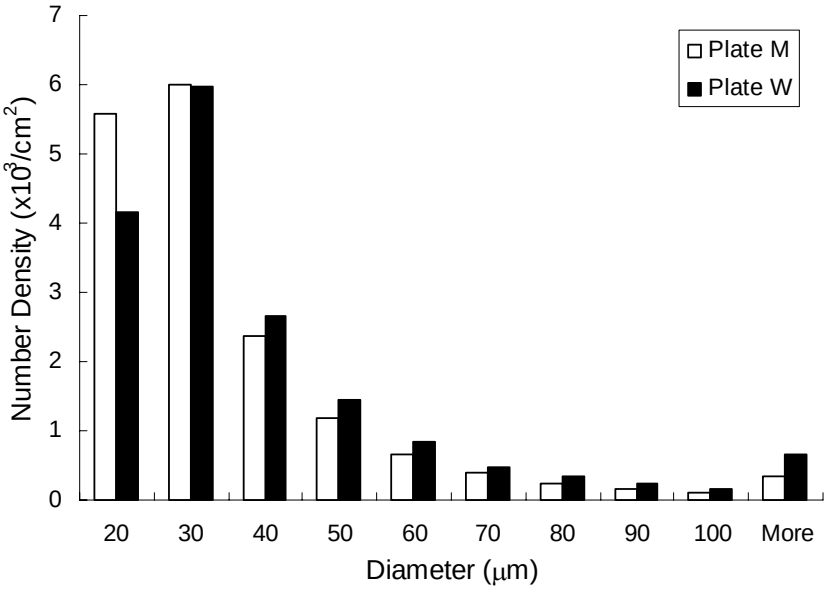

(a)

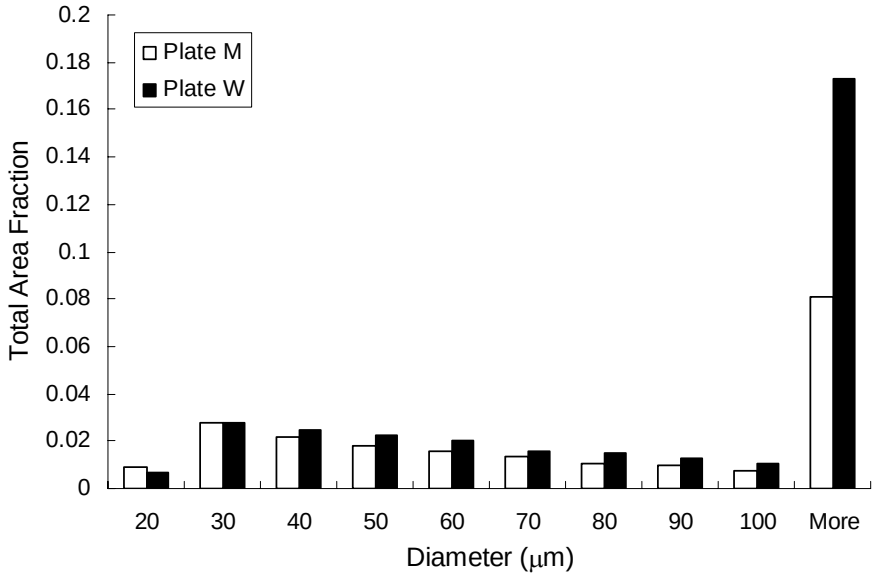

(b)

Figure 4.16: (a) Number based size distribution of gas pores in plates M and W. (b) Area fraction distribution of gas pores in plates M and W.

4.1.2.5 Effects of Combined Process Conditions on the Porosity

The present data show that gate velocity, intensification, and melt temperature individually affect the porosity distributions in the high-pressure die-cast microstructure of AM50 alloy. It is of interest to see the combined effect of all three variables. Figure 4.17a shows the variation of total porosity along the length of plates B and W.

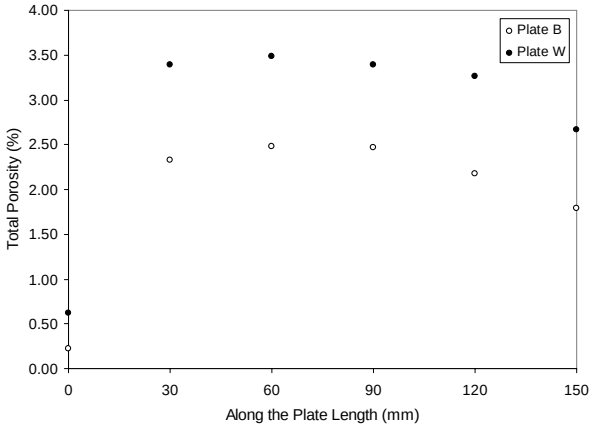

(a)

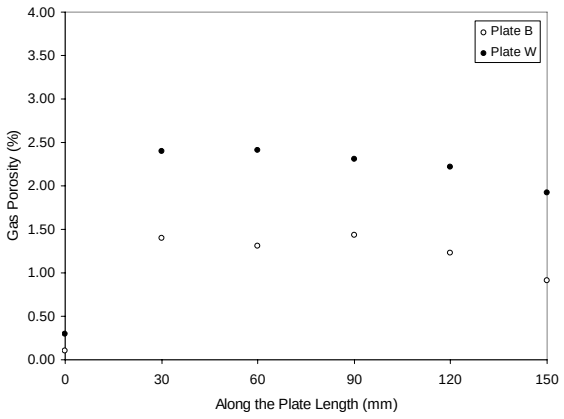

(b)

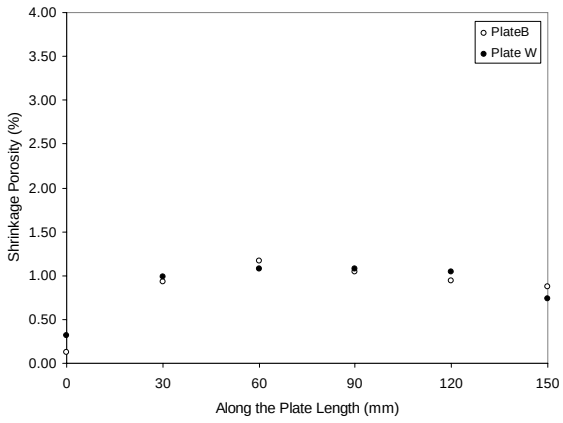

(c)

Figure 4.17: Plot of the percentage of (a) total porosity, (b) gas, and (c) shrinkage porosity as a function of the distance along the plate length.

Plate B was cast at a lower melt temperature and gate velocity as compared to plate W. Further, intensification was used for casting plate B but not plate W. At every location along the length of the plates, the percentage of total porosity in plate B is significantly lower than in plate W. There is a synergistic beneficial effect of lower gate velocity, lower melt temperature, and intensification pressure on the total porosity and gas porosity in the high-pressure die-cast AM50 alloy. Nevertheless, there is no significant difference in the shrinkage porosity in plates B and W. Therefore, it can be concluded that there is no beneficial synergistic effect of any of these process parameters in decreasing the shrinkage porosity. With current casting geometry and process conditions, the beneficial effect of varying only one process condition on the porosity amount in the component is comparable to that obtained by varying some or all of the process conditions. Therefore, only the most cost effective and easily controlled process would need to be taken into consideration along with how it affects the microstructure and shape and spatial arrangements of porosity.

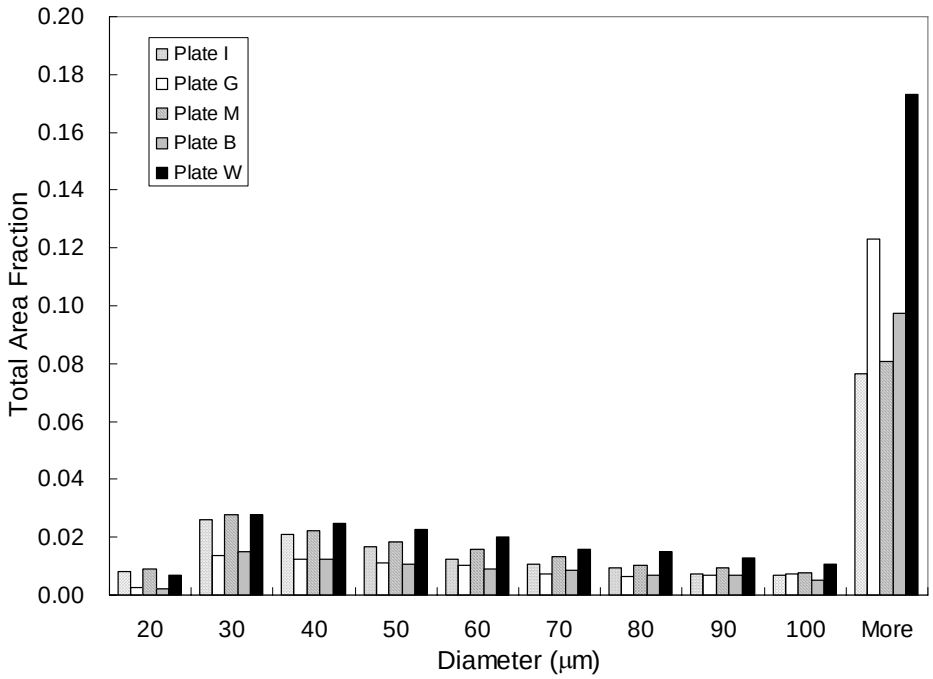

Figure 4.18: Comparison of area fraction distribution of gas pores in all the plates.

4.1.2.6 Summary on the Effects of Process Conditions on the Porosity in AM50 Alloy

An experimental parametric study has been carried out to quantitatively characterize the effects of intensification pressure, gate velocity, and melt temperature on the porosity distributions in the high-pressure die-cast AM50 Mg-alloy. The effects of these process parameters on amount of total porosity, gas porosity, shrinkage porosity, and pore size distributions are studied and they are illustrated in all at Figure 4.18. The experimental data lead to the following important observations and conclusions.

1. Application of intensification pressure significantly reduces the total amount of porosity primarily via reduction in the gas porosity. The intensification pressure significantly reduces the number density and area fraction of the gas pores larger than 100μm diameter.
2. A decrease in the gate velocity decreases the total amount of porosity predominantly via a decrease in the gas porosity and a small extent of decrease in the shrinkage porosity. The lower gate velocity uniformly decreases the number density and area fraction of gas pores of all sizes (small and large).
3. A decrease in the melt temperature also reduces the total amount of porosity primarily via reduction in the gas porosity. The lower melt temperature reduces the number density and area fraction of the gas pores larger than 30 μm.
4. There is no beneficial synergistic effect of any of these process parameters in decreasing the shrinkage porosity. The beneficial effect of varying only one process condition on the porosity amount in the component is comparable to that obtained by varying some or all of the process conditions.

4.1.3 Effects of Process Conditions on the Porosity in AM60 Thin Plates

The effects of process conditions such as intensification (plate I), gate velocity (plate G), and melt temperature (plate M) on the porosity distribution in the microstructure of AM60 thin plates (4.3 mm thickness) have been studied using the design of experiments similar to the one used for AM50 thick plates described in the previous section. These process conditions and sampling scheme are described in Table 3.2 and Figure 3.2, respectively. In addition to the effects of process conditions, these experiments also permit study of the effects of section thickness (4.3 mm versus 14.3 mm) on the HPDC microstructure, as the compositions of AM50 and AM60 alloys are not very different. Further, the detailed microstructural investigations on these thin plates (4.3 mm thickness) have led discovery of two other phenomena that affect the microstructure and the properties, namely, formation of gas induced shrinkage porosity, and inverse surface macro-segregation. To the best of author's knowledge, these phenomena have been observed and analyzed for the first time in the HPDC microstructures. The next sub-section describes the effects of process parameters on the porosity attributes, whereas the subsequent sub-sections present the detailed experimental evidence and analysis of the formation of gas induced shrinkage porosity and inverse surface macro-segregation.

4.1.3.1 Microstructural Observations

Figure 4.19 shows the unetched microstructures depicting gas and shrinkage porosity in plate I, G, M, and W taken from the same location of each plate. In these montages, the Y-direction is the thickness direction of the plate and the montages cover the complete thickness (4.3 mm) of the plate. Most of the gas pores (particularly the large ones) are located in the middle of the plate thickness. In all of the AM60 thin plates, defect (porosity) bands have been observed. Formation of these porosity bands can be explained as follows.

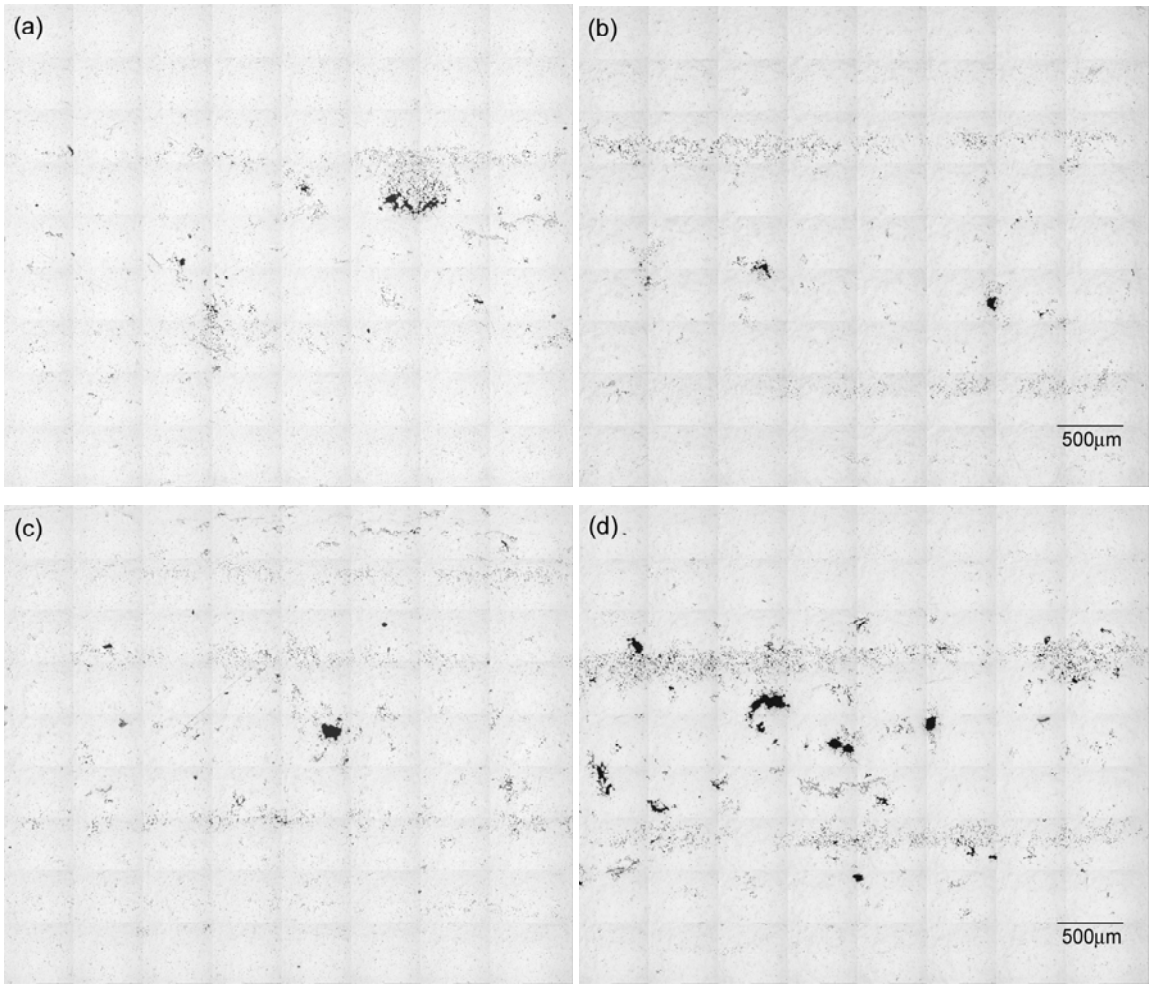

Figure 4.19: Gray scale montages of plate (a) I, (b) G, (c) M, and (d) W.

In the HPDC process, one solidification front initiates the mold cavity surfaces and moves inwards. On the other hand, the pre-solidified dendrites (i.e., those formed in the shot sleeve) present in the center lead to the formation of a second solidification front that moves from the center to the surface. The junction of these two solidification fronts, therefore solidifies last, and consequently contains lot of shrinkage porosity due to lack of liquid metal feeding. These bands often contain highly clustered pores, particularly in castings having small section thickness as observed in these thin plates. However interestingly such porosity bands are not observed in the microstructures of AM50 thick plates (14.3 mm thickness) presented earlier. The porosity bands mainly consist of shrinkage porosity. Since whether or not the porosity bands form is a function of process conditions and dimensions of the sections, it can be expected that the process conditions and plate thickness in the present AM60 plates are more favorable to form porosity bands as compared to those in AM50 thick plates. Figure 4.20 shows etched microstructures of surface (a) and center region (b) of the casting plates.

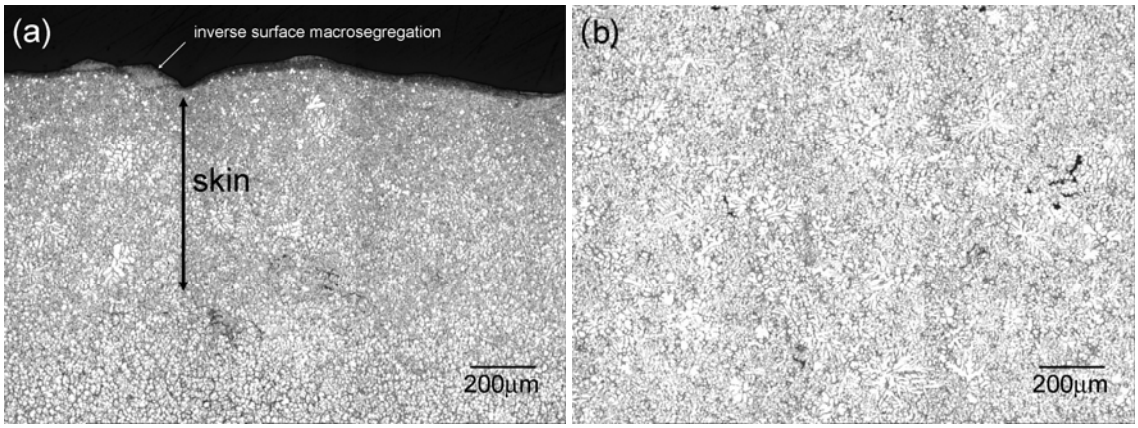

Figure 4.20: (a) Fine-grained skin region at the cast surface and (b) Typical cast microstructure showing cored Mg-rich dendrites. The larger grains have probably formed in the shot sleeve prior to liquid metal injection in the die cavity.

These microstructures show some of very interesting microstructural aspects. The skin regions are not well developed, although the solidification rate could be very fast as

compared to AM50 thick plates. Further, there are a few large dendrites in the skin regions, which are not observed at the skin regions of AM50 thick plates. In general, dendrites in the center regions of the microstructure are larger in size than those in the skin regions and the larger grains have probably formed in the shot sleeve prior to liquid metal injection in the die cavity.

Table 4.2. Average volume percentage of gas, shrinkage, and total porosity.

Plate ID	Gate Velocity (m/s)	Intensification	Melt Temp (ºC)	Gas (%)	Shrinkage (%)	Total (%)
I	5.2	On	705	0.16	0.28	0.44
G	2.7	Off	705	0.15	0.29	0.44
M	5.2	Off	682	0.24	0.43	0.67
W	5.2	Off	705	0.34	0.52	0.86

Table 4.2 summarizes the average volume percentage of gas, shrinkage, and total porosity. This Table demonstrates low gate velocity, or low melt temperature, or application of intensification pressure can reduce the total amount of porosity, i.e., each of these individual process parameters or their combinations can be optimized to reduce both gas and shrinkage porosity in the HPDC microstructure of AM60 alloy. It is important to note that in these thin plates, the shrinkage porosity has more contribution to the total porosity than the gas porosity. Shrinkage porosity is mainly from the solidification contraction; and therefore, the amount of shrinkage porosity may not be expected to vary significantly with the process conditions, as observed in the thick AM50 alloy plates. However, this is not true due to the formation of gas induced shrinkage porosity in these thin AM60 plates, which is discussed in detail in a subsequent section.

4.1.3.2 Effects of Intensification on the Porosity

The differences in the porosity attributes of I and W plates essentially reflect the effect of intensification pressure on the porosity: the intensification pressure was applied for casting plate I, whereas it was not applied for casting plate W. Figure 4.21 shows plots of the spatial distribution of total porosity in the three-dimensional space of the cast plate I (a) and W (b). Figure 4.22 shows the corresponding plots for the spatial distribution of gas porosity and Figure 4.23 shows the plots for shrinkage porosity. The majority of the gas pores are located in the middle of the plate thickness and also away from the edges of the plate along the width direction. Unlike the porosity distribution in the AM50 thick plates, shrinkage porosity has more contribution to the total porosity than the gas porosity as shown in Figure 4.23. In general, as these plates are thinner, less gas pores are formed. However, formation of shrinkage porosity is mainly from the solidification contraction followed by insufficient liquid melt feeding. Therefore, at the small section thickness levels, shrinkage porosity becomes prominent, whereas at higher section thickness levels, gas porosity is more prominent. The application of intensification effectively decreases the amount of gas as well as shrinkage porosity in these thin AM60 plates. This is probably because at this section thickness level, applied level of intensification pressure is sufficient to compress the large gas pores as well as to facilitate the feeding in the inter-dendritic channels leading to a decrease in the shrinkage porosity as well. Figure 4.24 shows the spatial location of each large pore (pores larger than 50 μm diameter) in the plates I and W. These data clearly show that intensification pressure effectively reduces the number density of large pores.

Figure 4.25a shows the variation of the total porosity as a function of distance along the length of the plates. At every location along the length of the plates, the percentage of total porosity in the plate I is lower than that at the corresponding location in the plate W. Figure 4.25b shows the variation of the percentage of the gas (air) pores with the distance along the length of the two types of plates.

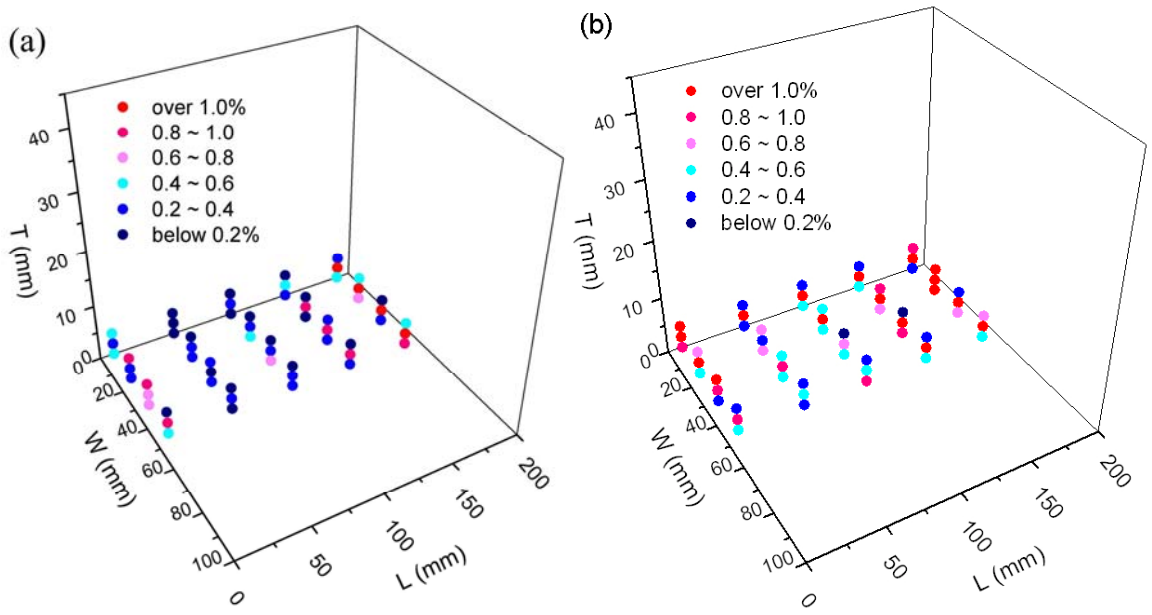

Figure 4.21: Spatial distributions of the percentage of total porosity of (a) plate I and (b) plate W at different locations along the length, width, and thickness of plates.

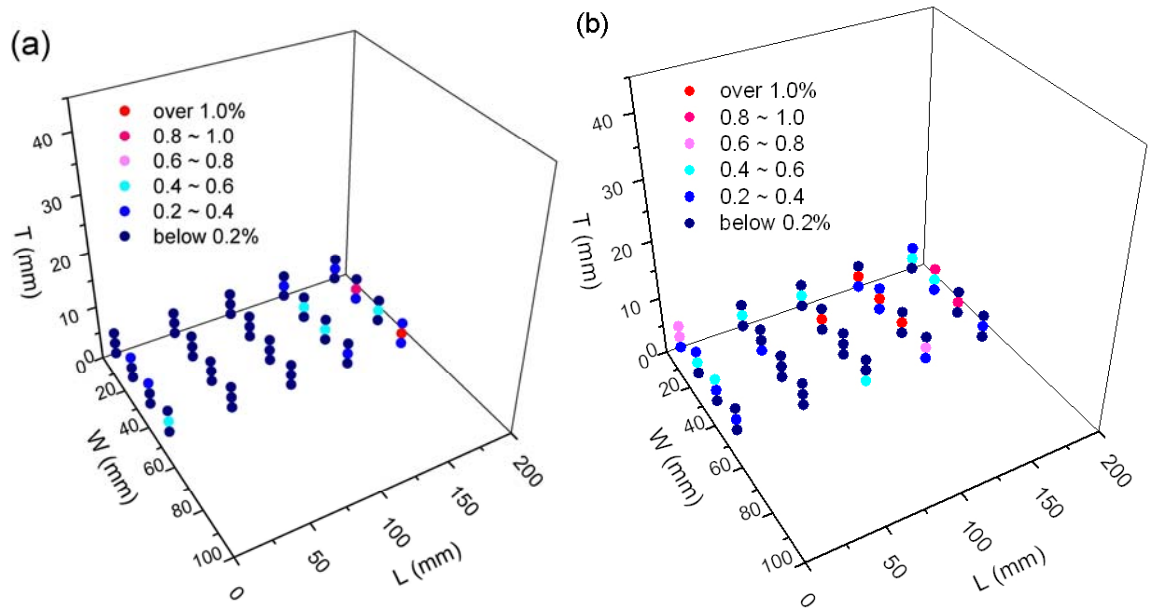

Figure 4.22: Spatial distributions of the percentage of gas porosity of (a) plate I and (b) plate W at different locations along the length, width, and thickness of plates.

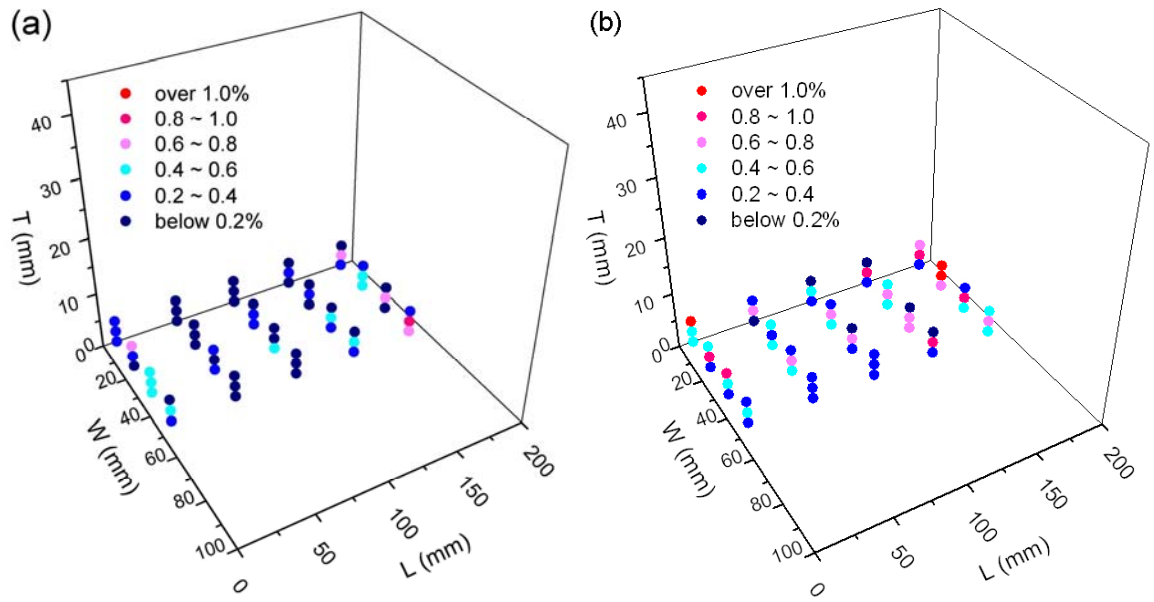

Figure 4.23: Spatial distributions of the percentage of shrinkage porosity of (a) plate I and (b) plate W at different locations along the length, width, and thickness of plates.

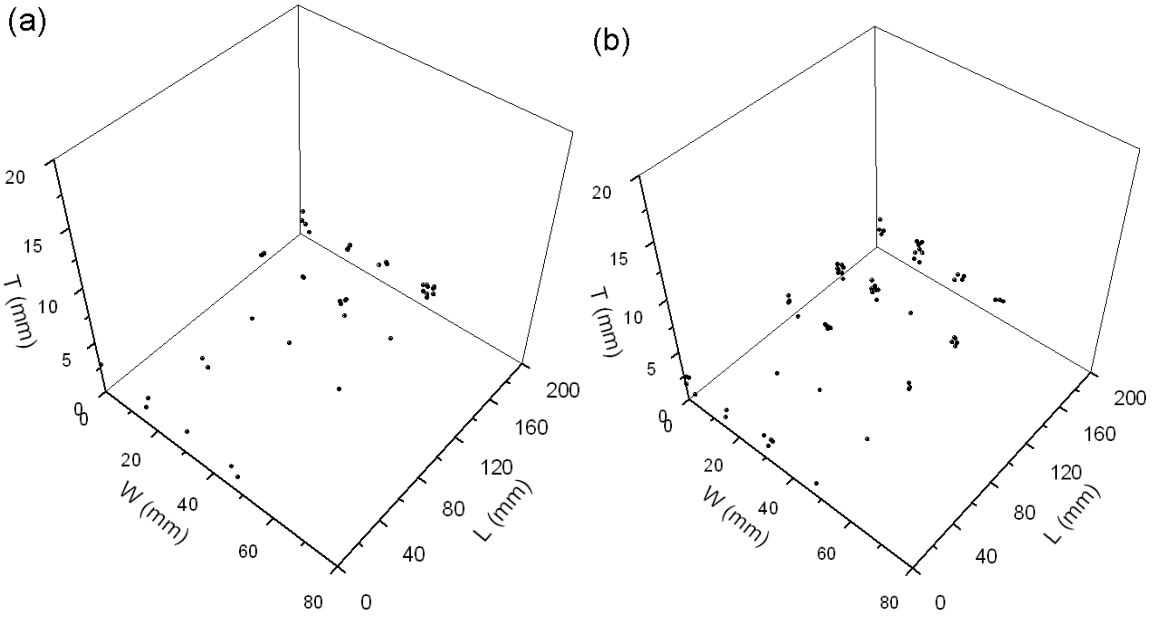

Figure 4.24: Location of each pore larger than 50 m diameter in (a) plate I and (b) plate W. Note that in this figure each "dot" represents the location of a large pore.

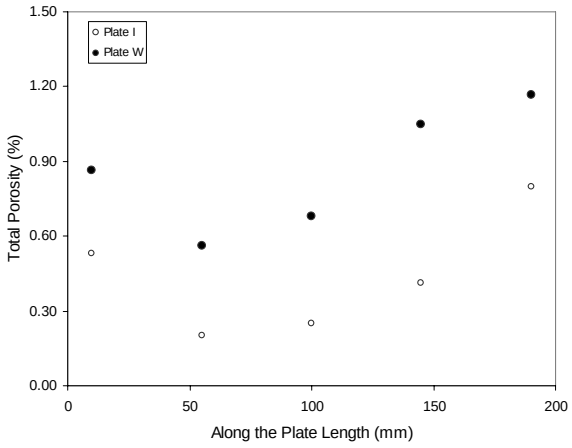

(a)

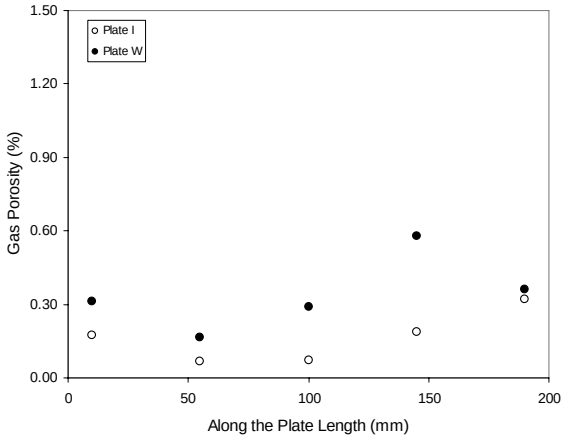

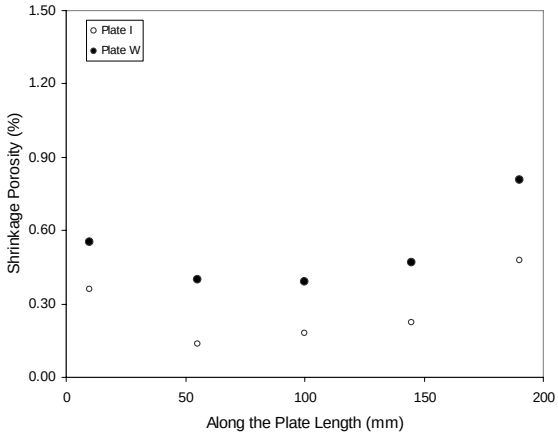

(b) (c)

Figure 4.25: Plot of the percentage of (a) total porosity, (b) gas, and (c) shrinkage porosity as a function of the distance along the plate length.

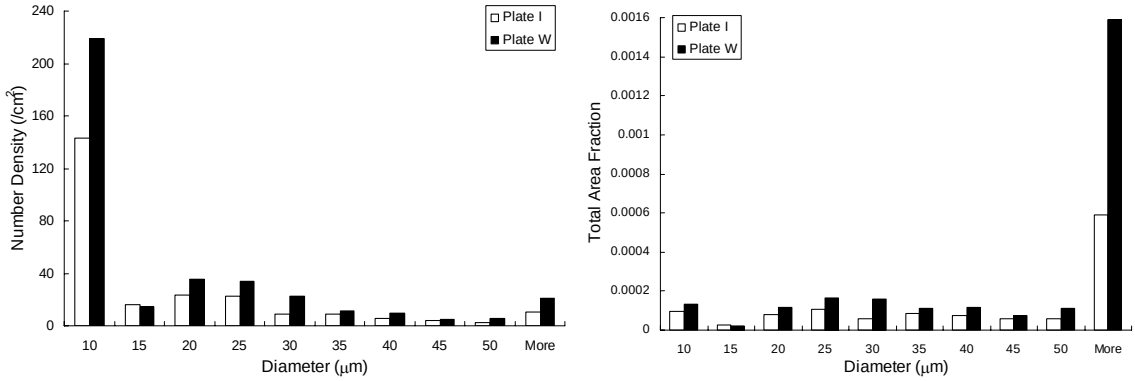

(a) (b)

Figure 4.26: (a) Number based size distribution of gas pores in plates I and W. (b) Area fraction distribution of gas pores in plates I and W.

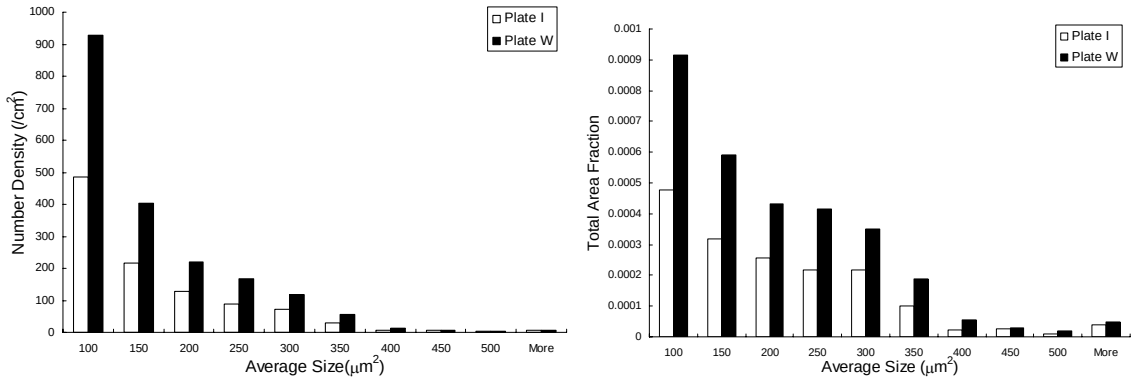

(a) (b)

Figure 4.27: (a) Number based size distribution of shrinkage pores in plates I and W. (b) Area fraction distribution of gas pores in plates I and W.

Again, at most of the locations along the length of the plates, the percentage of gas porosity in the plate I is lower than that at the corresponding location in the W plates. This is because the intensification pressure compresses the gas pores, and consequently, the reduction is the sizes (volumes) of the pores leads to the lower volume percentage of the gas porosity. The amount of shrinkage porosity is reduced to some extent by intensification as shown in Figure 4.25c, therefore the application of intensification pressure decreases the amount of shrinkage porosity via the facilitation of the liquid feeding in the inter-dendritic channels and gas porosity via the compression of the gas pores. It is likely that in these relatively thin plates (4.3 mm thickness), the applied intensification pressure is effective enough to decrease the amount of shrinkage porosity.

As the intensification pressure is effective in reducing porosity, it is of interest to examine the effects of intensification on the size distribution of the gas and shrinkage pores. Figure 4.26 shows the conventional number distribution and the area fraction distribution of the gas pores in the plates I and W, which clearly brings out the contribution of the large pores. The contribution of decrease in the amount of gas pores due to application of intensification pressure is mainly through reduction of the number density and area fraction contribution from the large pores larger than 50 μm diameter, which is due to compression of the large pores. However, as mentioned earlier, in these plates, reduction in the total porosity is predominantly due to the reduction in the shrinkage porosity. Therefore, it is of interest to examine the effects of intensification on the size distribution of the shrinkage pores. Figure 4.27 shows the number distribution and the area fraction distribution of the shrinkage pores in the same two plates, which clearly shows the effect of intensification for all of the shrinkage size range. The decrease in the amount of shrinkage is mainly from the reduction in the number of shrinkage at every size range, which is facilitated by the liquid feeding in the inter-dendritic channels. Therefore, the intensification pressure used in this study is very effective to compress large pores and also to facilitate the inter-dendritic liquid feeding.

4.1.3.3 Effects of Gate Velocity in the Porosity

The differences in the porosity attributes in the plates G and W reflect the effect of gate velocity. Figure 4.28 shows that that at every location along the length of the plates, the percentage of both the gas and shrinkage porosity in the G plate cast at gate velocity of 2.7 m /sec is lower than that at the corresponding location in the W plate cast at 5.2 m/sec gate velocity.

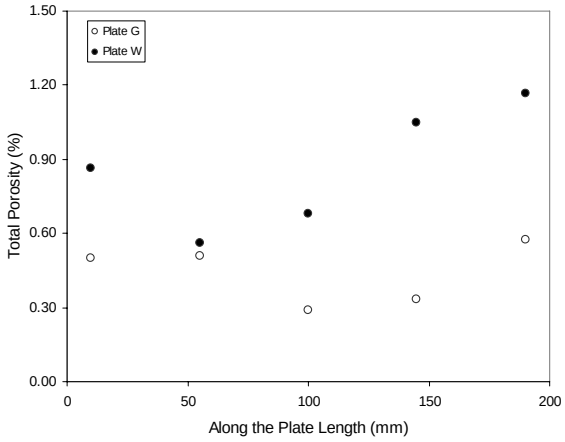

(a)

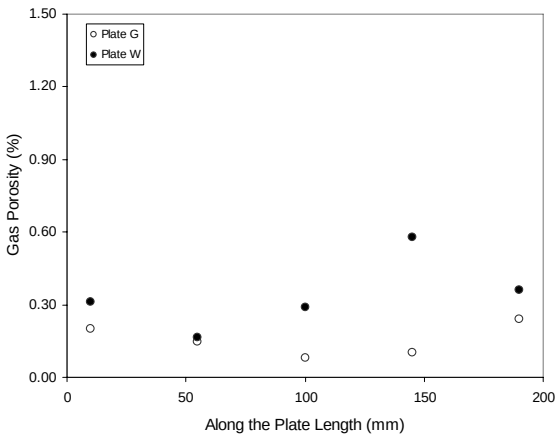

(b)

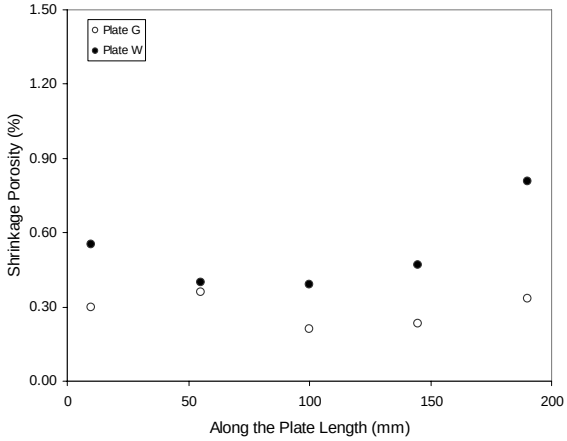

(c)

Figure 4.28: Plot of the percentage of (a) total porosity, (b) gas, and (c) shrinkage porosity as a function of the distance along the plate length.

This can be explained by the reduction of liquid melt turbulence caused by the slower gate velocity. Figure 4.29 compares the number distribution of gas pores in different size ranges. The decrease in the gate velocity from 5.2 m/sec (Plate W) to 2.7 m/sec (Plate G) uniformly decreases the number density of the gas pores in each size class, however the reduction in the amount of gas pores is mainly due to the decrease in the area fraction of the large pores (pores larger than 50 μm diameter).

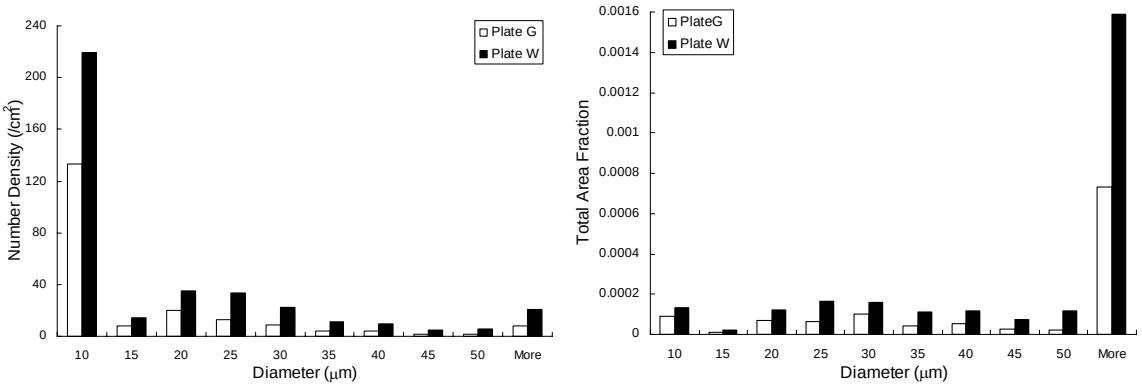

(a) (b)

Figure 4.29: (a) Number based size distribution of gas pores in plates G and W. (b) Area fraction distribution of gas pores in plates G and W.

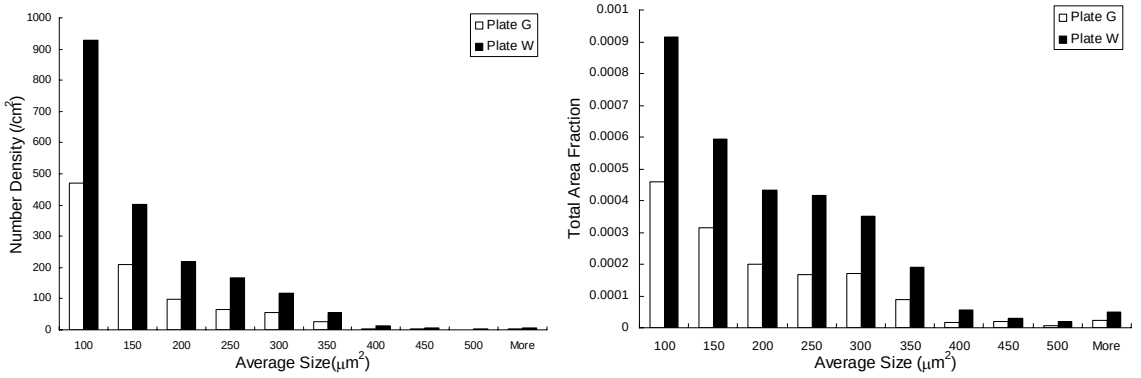

(a) (b)

Figure 4.30: (a) Number based size distribution of shrinkage pores in plates G and W. (b) Area fraction distribution of gas pores in plates G and W.

Interestingly, Figure 4.30 shows that the number density and area fraction of shrinkage are very effectively decreased in a similar way to those in the application of intensification pressure at every size range whose reduction is very comparable to plate I. This result is somewhat surprising because liquid melt velocity at the gate affects the melt turbulence, and therefore, it is likely to affect the attributes of gas pores not the shrinkage pores. This issue is discussed in more detail in section 4.1.5.

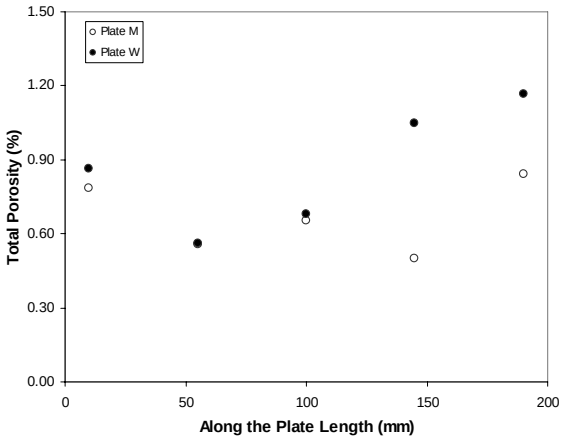

(a)

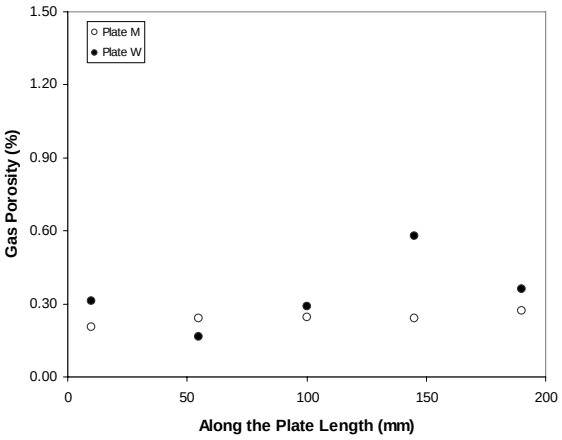

(b)

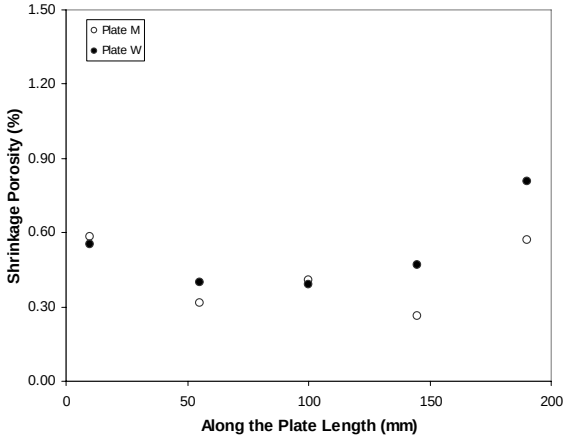

(c)

Figure 4.31: Plot of the percentage of (a) total porosity, (b) gas, and (c) shrinkage porosity as a function of the distance along the plate length.

4.1.3.4 Effects of Liquid Melt Temperature on the Porosity

The differences in the porosity attributes in the plate M and W essentially reflect the effect of melt temperature. Figure 4.31 shows that at every location along the length of the plates, the percentage of both the gas and shrinkage porosity in the M plate cast at the melt temperature of 682 ºC is lower than that at the corresponding location in the W plate cast at 682 ºC. The lower melt temperature mainly decreases the amount of dissolved gases in the melt and thereby decreases the gas porosity. These trends are observed at Figure 4.32 and 4.33. The decrease in the total porosity is mainly from the reduction of area fraction of large gas pores larger than 50 μm diameter, but a little contribution by shrinkage porosity. The lower melt temperature decreases the amount of dissolved gases in the melt and thereby decreases the gas porosity, rather than affecting the contribution to the gas porosity from the trapped air.

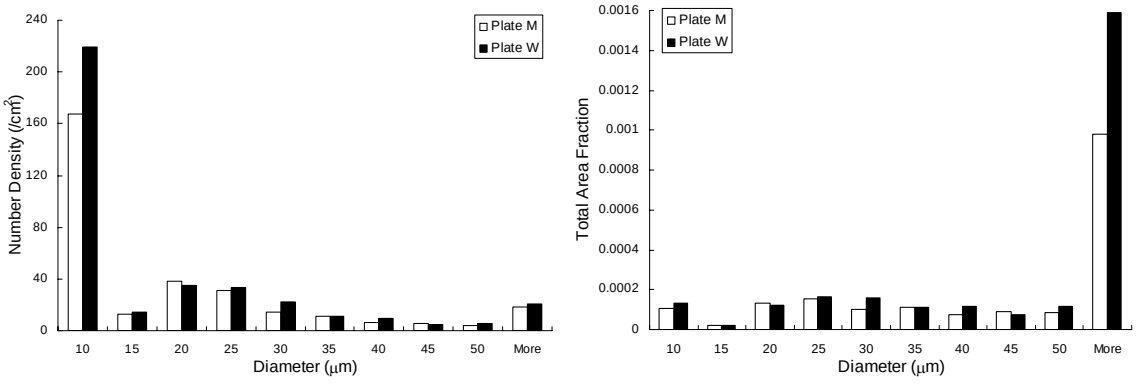

(a) (b)

Figure 4.32: (a) Number based size distribution of gas pores in plates M and W. (b) Area fraction distribution of gas pores in plates M and W.

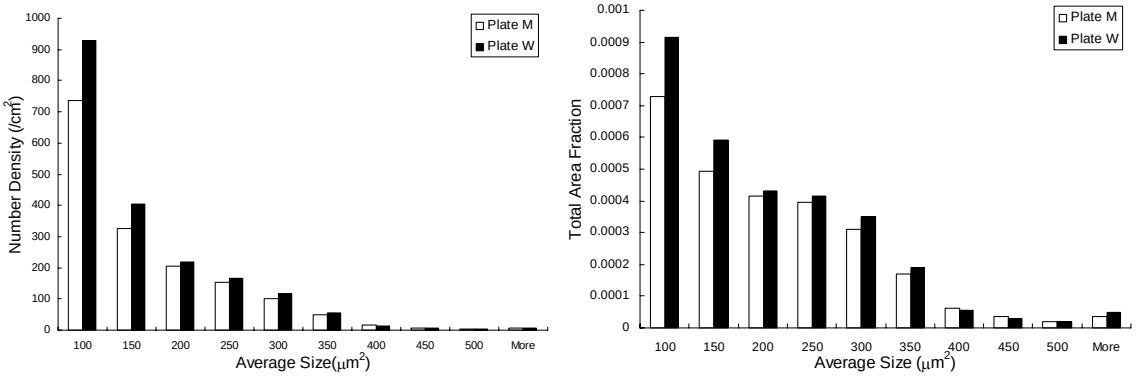

(a) (b)

Figure 4.33: (a) Number based size distribution of shrinkage pores in plates M and W. (b) Area fraction distribution of gas pores in plates M and W.

4.1.3.5 Summary on the Effects of Process Condition on the Porosity in AM60 Alloy

An experimental parametric study has been carried out to quantitatively characterize the effects of intensification pressure, gate velocity, and melt temperature on the porosity distributions in the high-pressure die-cast AM60 Mg-alloy. With current casting geometry and process conditions, varying any of the process conditions has a beneficial effect on the decrease in the total amount of porosity. However, shrinkage porosity has more contribution on the reduction in the total porosity and varies significantly in amount with process conditions, which was not observed in AM50 alloy. This is due to formation of gas induced shrinkage porosity at lower section thickness levels, which is discussed in detail in the next sub-section.

4.1.4 Formation of Gas Induced Shrinkage Porosity

The previous study on the effects of process conditions on the attributes of shrinkage porosity in AM60 thin plates has led to puzzling observation s related to effects of process conditions on the shrinkage porosity. It is usually believed that the gas and shrinkage porosity can be regarded as independent microstructural attributes. This is the basic under pinning of the majority of approaches for improvement of fracture sensitive

mechanical properties of the HPDC Mg-alloys via control of process parameters such as molten metal temperature, intensification pressure, gate velocity, and casting geometry that affect porosity. Numerous microstructural observations and numerical simulations will be now presented to show that presence of gas pores has a bearing on the formation of shrinkage porosity, and therefore, approaches to understand the effects of process conditions on gas and shrinkage porosity should take into account such dependencies.

4.1.4.1 Hypothesis of Gas induced Shrinkage Porosity

It is shown for the first time that, under specific conditions, in high-pressure die-castings, presence of gas pores can facilitate formation of shrinkage porosity, namely gas induced shrinkage porosity, and therefore, gas and shrinkage pores cannot be treated as independent microstructural features. The gas porosity induces formation of shrinkage porosity because the air in the gas pores is an efficient heat-insulating medium, and consequently, the presence of gas pores can decrease the heat transfer rate in the liquid melt as compared to similar regions without gas porosity, leading to lower the local solidification rate in regions containing gas pores, which induces formation of shrinkage pores around the gas pores. To support this hypothesis, evidence is presented from (i) experimental metallographic observations involving three-dimensional microstructure reconstruction, and (2) computer simulations of heat transfer to analyze the mechanism of the formation of gas induced shrinkage porosity. In addition, finite elements (FE) based simulations are presented to illustrate the effects of the presence of shrinkage porosity around gas pores on the local stresses and strains.

4.1.4.2 2D Microstructural Observation of Gas Induced Shrinkage Porosity

Figure 4.34a and b depict magnified images of large gas pores and *gas induced* shrinkage porosity clustered around these gas pores. Note that, at least in the 2D section, the shrinkage pores in Figure 4.34a and b do <u>not</u> appear to be connected the

corresponding central gas pore(s) around which they are clustered. It will be shown in the next chapter that these gas induced shrinkage pores are not connected to corresponding gas pore(s) in the three-dimension as well, which distinguishes the gas induced shrinkage porosity form the conventional shrinkage porosity that is usually topologically connected to the gas pores present in its immediate vicinity. Figure 4.34c illustrates such conventional shrinkage porosity around gas pores. However, as opposed to gas induced shrinkage porosity in Figures 4.34a and b, the conventional shrinkage porosity in Figure 4.34c is topologically connected to the corresponding gas pores in 2D sections (and therefore, in 3D microstructure as well). It must be pointed out that the conventional shrinkage porosity can be present in the regions that do not contain gas pores as illustrated in Figure 4.34d, whereas gas induced shrinkage porosity is present only in the vicinity of gas pores but not topologically connected to them. It is interesting to note that the "sponge" type gas induced shrinkage porosity is not observed in the regions that do not contain gas pores. The gas (mostly trapped air in the mold cavity) in the gas porosity is an efficient heat-insulating medium; therefore the presence of gas porosity can retard the heat transfer in the liquid melt as compared to similar regions without gas porosity. Consequently, the local solidification rate is lower in such region, leading to shrinkage porosity formation. It is very essential to reconstruct the 3D microstructure to understand the complex real 3D geometry and topological connectivity of porosity to demonstrate that the gas induced shrinkage porosity is not topologically connected to the corresponding gas pores in the three-dimension either. Figure 4.35a shows surface rendered 3D microstructure depicting only the pores.

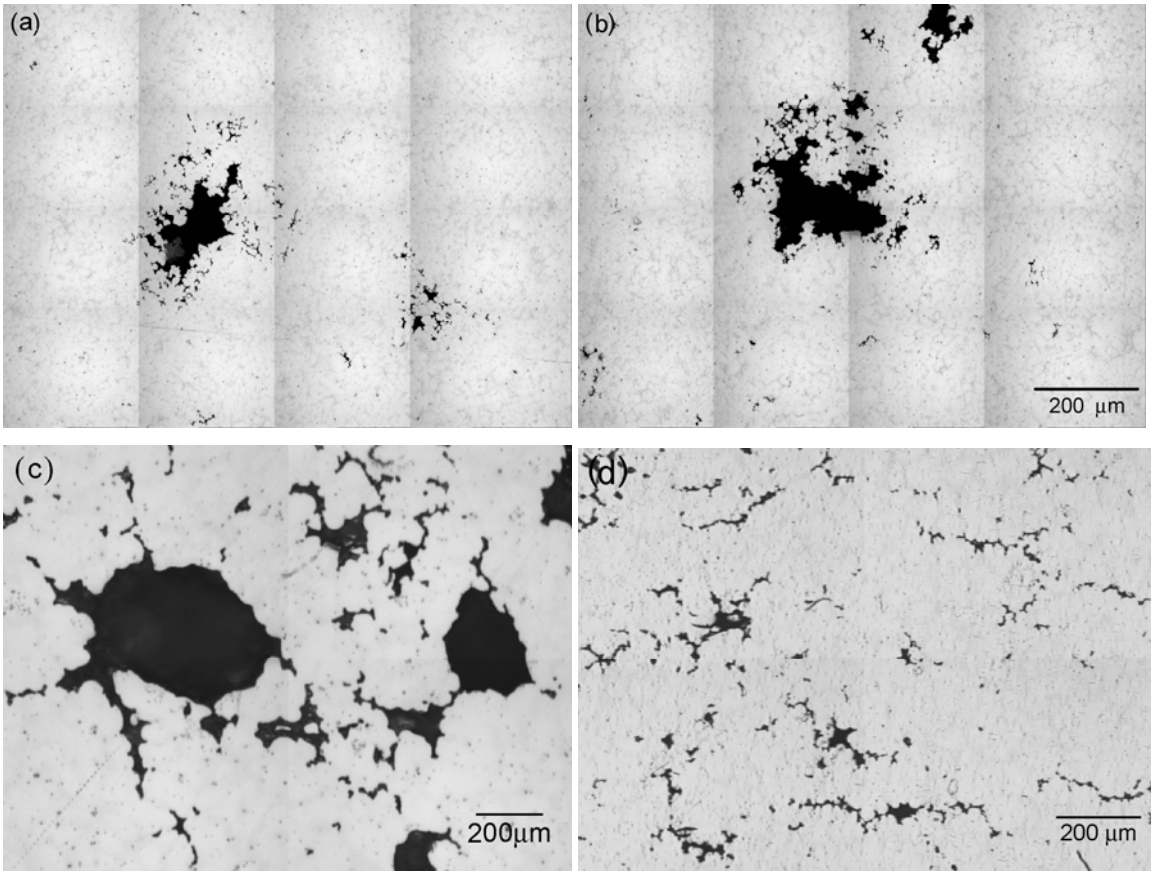

Figure 4.34: (a) and (b) large gas pores and gas induced shrinkage porosity clustered around these gas pores, (c) conventional shrinkage porosity around gas pores, and (d) conventional shrinkage porosity in a region not containing gas pores.

This 3D image contains the central large gas pore and the surrounding shrinkage porosity. It needs to be shown that the shrinkage porosity in Figure 4.35a is not topologically connected to the central gas pore. To show this, the central gas pore is separately shown in Figure 4.35b. This image contains only those bright voxels (3D pixels) that are connected together, i.e., one can traverse from any one bright voxel in this image to any other bright voxel without ever entering any dark voxel. Note that this segmentation of the central gas pore is done *automatically* via image analysis. Such separation is possible *if and only if* corresponding shrinkage porosity is not connected to the gas pore. The image analysis software does not permit such separation if the shrinkage porosity were connected to the central gas pore. The image processing also permits separate visualization of the gas induced shrinkage porosity in the three-dimensions as shown in Figure 4.35c. Such clear separation of gas and shrinkage porosity is not possible if the shrinkage porosity is connected to the gas pore. Figure 4.35d shows 3D microstructure for conventional porosity image depicting the complexity of the porosity shape and random spatial arrangement of the gas (air) and shrinkage porosity [14]. In Figure 4.35d, most of gas (air) and shrinkage pores are connected, except a few that is in very small size ranges, which is very different from porosity distribution in Figure 4.35a. These 3D microstructural observations clearly reveal the presence of gas induced shrinkage porosity, i.e., microstructure contains shrinkage pores that are clustered around gas pores but not topologically connected to the corresponding gas pore(s). This type of gas induced shrinkage porosity is of concern not only because of an increase in total amount of porosity, but also because it leads to higher local stress concentrations around the gas pores.

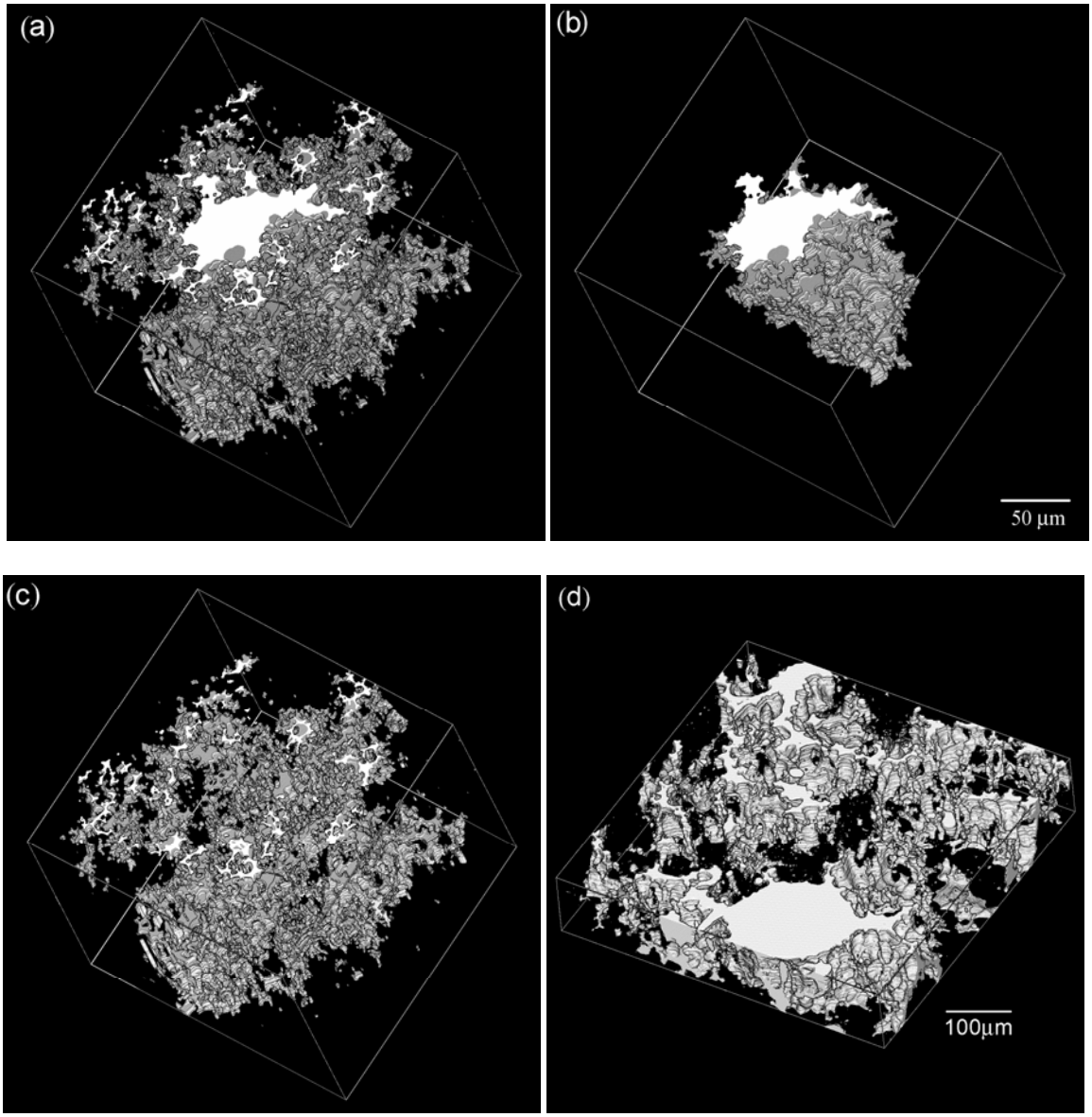

Figure 4.35: (a) Surface-rendered reconstructed 3D microstructure of gas induced shrinkage porosity clustered around central gas pore, (b) view of the center gas pore from the porosity shown in a, (c) view of gas induced shrinkage porosity in a; the Figure b and c can be combined to produce the image in a, and (d) 3D microstructure showing conventional shrinkage porosity usually connected to gas porosity.

4.1.4.4 Three-Dimensional Finite Element Analysis

The local stress distributions around the gas pores in the cast microstructure that have gas induced shrinkage porosity around them may not necessarily be same as those around the gas pores in the microstructural regions that do not contain gas induced shrinkage porosity. To gauge the extent of these differences in the local stress distributions, the digital image of the 3D microstructure reconstructed from serial sections is implemented in a 3D finite elements (FE) computational framework. The reconstructed 3D microstructure in STL (stereo lithography) format is exported into Harpoon (CEI), commercial automatic meshing software to mesh the geometry with tetrahedral elements. Only the external volume of the STL file is meshed leaving porosity free of elements. Figure 4.36a and b show FE mesh created from a segmented gas pore in Figure 4.35b and gas and shrinkage porosity combined in Figure 4.35c to study the effects of gas induced shrinkage porosity on the local stress distribution. The meshes for a segmented gas pore and gas induced shrinkage porosity contain 481478 and 1113696 linear tetrahedral elements, respectively. The FE meshes are then exported to ABAQUS, commercial finite element code and analyzed for the elastic mechanical response to a tensile load. Figure 4.36c and d show the local von Mises stress distribution in the microstructural volume due to an applied uniaxial tensile load. These figures clearly demonstrate that the local stress distribution is significantly affected by the presence of gas induced shrinkage porosity: the local Von Mises stresses are higher in the regions around gas induced shrinkage porosity. This is the reason why the gas induced shrinkage porosity can adversely affect the fracture related mechanical properties of the HPDC Mg-alloy casting.

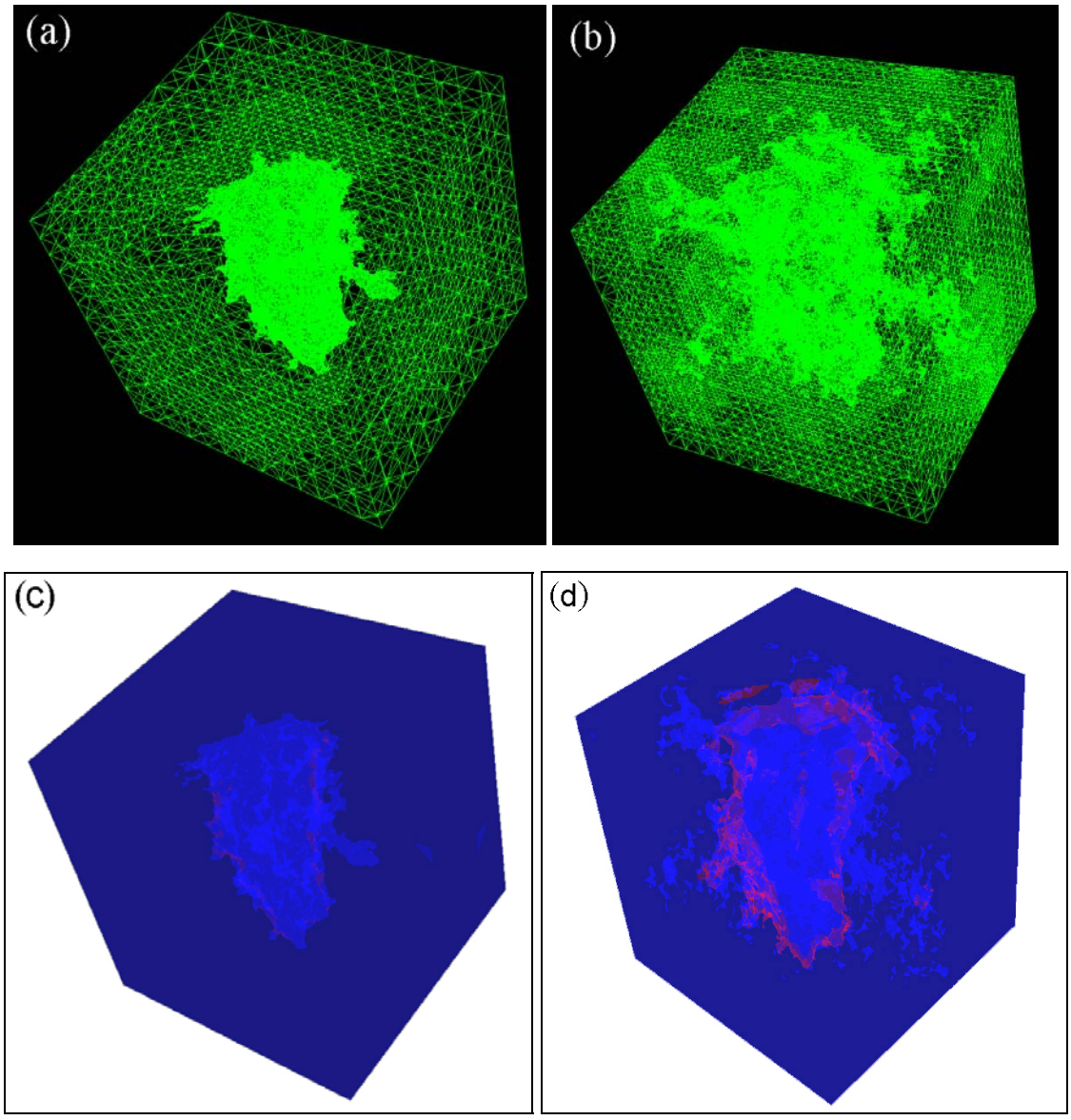

Figure 4.36: (a) Three-dimensional finite element mesh only for gas, (b) gas and shrinkage porosity combined, (c) local stress distributions for only gas pore, and (d) gas and shrinkage pores.

4.1.4.5 Numerical Simulation for Transient Heat Transfer

The heat transfer simulations were performed to study the effect of the presence of gas pore on the local heat transfer rate that subsequently determines the local solidification rate of the casting using the initial conditions and boundary conditions given in Table 4.3.

Table 4.3. Modeled geometry and initial and boundary conditions.

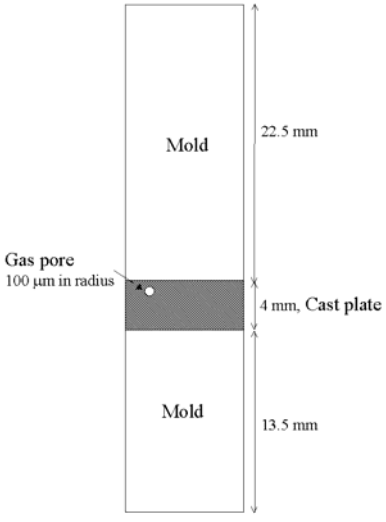

Initial and Boundary Conditions

Mold
H13 die steel, Initial Temp. : 100°C
Thermal convection at top and bottom surfaces
Film coefficient ($g/s^3 \cdot °C$) : 11539
Thermal conductivity ($cm \cdot g/s^3 \cdot °C$) : 2.05×10^6
Specific heat ($cm^2/s^2 \cdot °C$) : 4.6×10^6,Density (g/cm^3) : 7.76

Liquid Melt
Pure Mg, Initial Temp. : 703°C

Temp.	Thermal conductivity	Enthalpy (cm^2/s^2)
127	1.48×10^7	1.07×10^8
300	1.45×10^7	3.2×10^8
527	1.43×10^7	5.8×10^8
703	1.43×10^7	12.02×10^8

Gas Pore (air)
Temp. : 703°C
Heat transfer in liquid melt only by thermal conduction

These numerical simulations were carried out using commercial software ANSYS 7.1. A gas pore of 100μm radius was simulated in the cast plate to investigate the effects of the presence of gas porosity on the temperature distribution surrounding it as compared to the region without gas porosity. The initial liquid melt temperature was computed at the time when the liquid melt completely filled the die cavity from die casting simulation using CFD modeling software, FLOW 3D 8.2. These simulations assume utilize the thermo-physical data corresponding to pure Mg (as data on AM60 alloy are not available), neglect radiation effect within the gas pore, and have been

carried out for temperature of 703 °C at the interface between liquid melt and the gas pore. The simulation begins at the instant where the liquid metal has completely filled the mold cavity; therefore, liquid metal flow is not incorporated in the simulations.

Figure 4.37 shows the temperature distribution in cast plate and depicts that the local temperature distribution is changed due to the presence of gas pore.

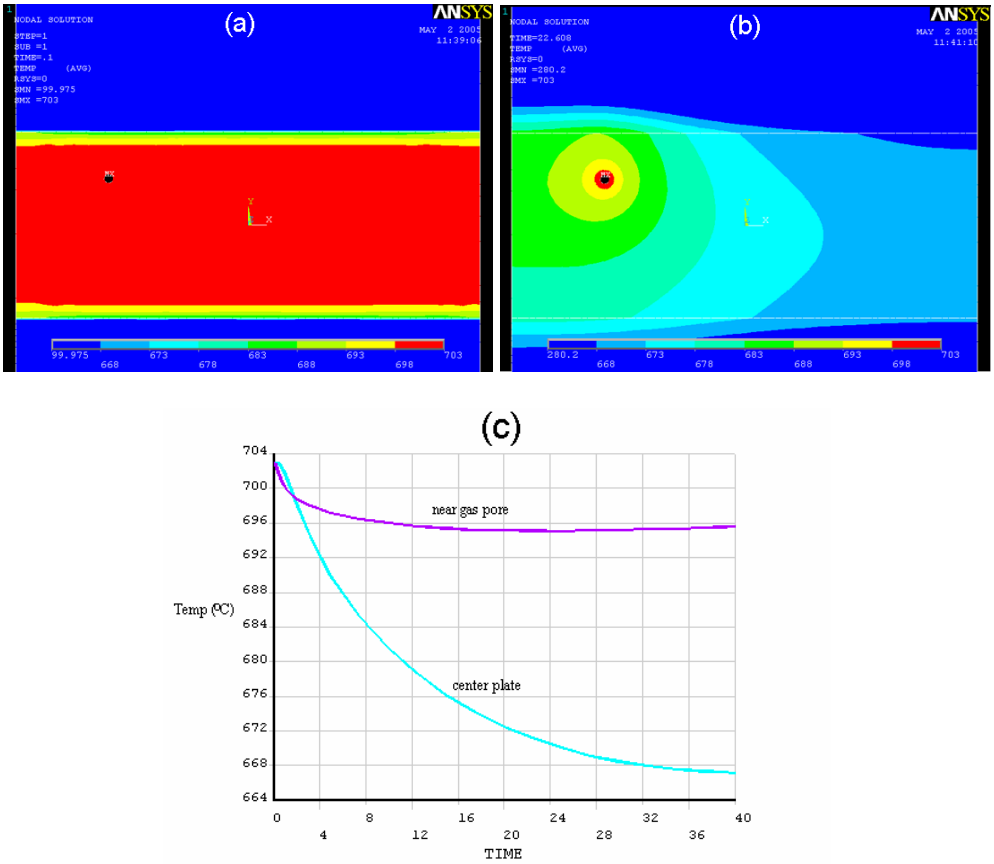

Figure 4.37: (a) Temperature distribution at time=0sec, (b) at time=22sec, and (c) Comparison of temperature profiles between near the gas pore region and center of the plate region.

Compared to the center region, the temperature near the large gas pore is much higher, and consequently that region is expected to solidify last leading to the formation of shrinkage porosity. This simulation is very simplified in that thermal radiation within

the gas pore is assumed to be negligible and other thermal effects of eutectic phases are also not considered. However, this result shows the feasible effect of gas pore in the liquid melt on the local heat transfer and solidification rate. Formation of gas induced shrinkage porosity has some distinctive dependencies on several factors essentially affecting the heat transfer and local solidification rate during the casting such as component thickness, alloy compositions, and process conditions.

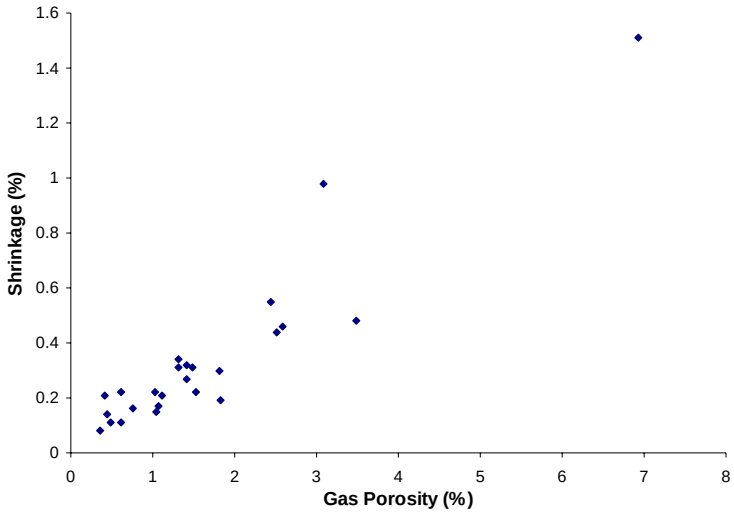

Figure 4.38: Variations of shrinkage porosity with corresponding gas porosity.

4.1.4.6 Correlation of Gas Induced Shrinkage Porosity with Total Porosity

If the hypothesis of formation of gas induced shrinkage porosity is correct, then amount of gas induced shrinkage porosity should increase with the increase in the amount of gas porosity. As the volume fraction of gas pores increases larger regions around the gas pores are susceptible to formation of gas induced shrinkage pores. To characterize the correlation between the volume fraction of gas porosity and gas induced shrinkage porosity, the measurements were performed on total of 26 microstructural montages. Each montage was converted into binary image and the porosity that is not directly related with the corresponding gas pores was digitally removed. Figure 4.38 depicts

strong quantitative correlation between the volume percentage of gas induced shrinkage porosity and the gas porosity. Therefore, contribution of shrinkage porosity in the total amount of porosity is partly due to the presence of gas porosity, which should be taken into account in the study of the effect of the process conditions on the porosity.

4.1.4.7 Summary on the formation of gas induced shrinkage porosity

The metallographic evidence is presented for existence of gas induced shrinkage porosity using 2D and 3D microstructural observations. The metallographic evidence is further substantiated using heat transfer simulations. Further, the importance of gas induced shrinkage porosity on the local stress distribution is studied. These experimental data and numerical simulations lead to the following important observations and conclusions.

1. The presence of gas porosity in the casting components can lead to the formation of a new type of shrinkage porosity, gas induced shrinkage porosity, under specific conditions. A numerical simulation for heat transfer during the casting process supports that the presence of gas porosity can retard the heat transfer and change the local solidification rate leading to the formation of gas induced shrinkage porosity.

2. The visualization of the reconstructed 3D microstructures yields the real morphologies of the gas and shrinkage porosity, their connectivity, and spatial correlations, which further support conclusions drawn from the numerical analysis and 2D microstructural observations

3. It is illustrated that the reconstructed 3D microstructures can serve as a representative volume element in the FE-based computational simulations of mechanical response. The FE simulations show that presence of shrinkage porosity around gas pores can significantly increase the local stresses in such regions that can adversely affect the fracture sensitive mechanical properties of HPDC castings.

4. Decrease in the amount of shrinkage porosity in the thin AM60 plates is partly due to the presence of gas porosity, and therefore shrinkage porosity increases with increasing gas porosity.

4.1.5 Formation of Inverse Surface Macrosegregation

High-pressure die-casting is inherently very complex process and phase transformation from liquid to solid phases takes place under non-equilibrium state and at a very fast rate, which creates defects such as inverse surface macrosegregation, which is reported for the first time in HPDC microstructures of Mg-alloys. In this section, strong metallographic evidence is presented to show that in HPDC Mg-alloys, inverse surface macrosegregation occurs under certain process conditions, and effects of the HPDC process parameters on the extent of such segregation are characterized to determine the process conditions that minimize such segregation.

The inverse surface macrosegregation significantly increases the amounts of brittle eutectic constituents (such as intermetallic compounds) that form at the cast surfaces. Therefore, it can be expected that the presence of inverse macrosegregation at the cast surfaces adversely affect the fracture related properties such as ductility, toughness, and fatigue resistance of the cast components. The effects of the segregation on the fatigue life of HPDC AM60 alloy are studied and described in another section.

4.1.5.1 Metallography

Metallographic samples were taken from five AM60 thin plates that permit “deconvolution” of the individual effects of intensification pressure (plates I and W), gate velocity (plates G and W), and liquid melt temperature (plates M and W) on the inverse surface macrosegregation as well as the porosity levels in the cast microstructure of the HPDC AM60 Mg-alloy. To characterize the extent of inverse surface macrosegregation as a function of distance along the length, width, and thickness of the plates, the

metallographic specimens were sampled at the locations illustrated in Figure 4.39. Only half of the cast plate was taken from the whole plate due to the symmetry of the casting geometry. Three sections of 5 mm thickness were cut at 80 mm intervals. The specimens were etched at room temperature using acetic glycol etching agent (20 ml acetic acid, 1 ml nitric acid, 60 ml ethylene glycol, and 19 ml water) to reveal the grain structure and eutectic constituents, and to detect the inverse macrosegregation. Hitachi S-4100 scanning electron microscope equipped with an energy dispersive X-ray analyzer was used to characterize the local compositions.

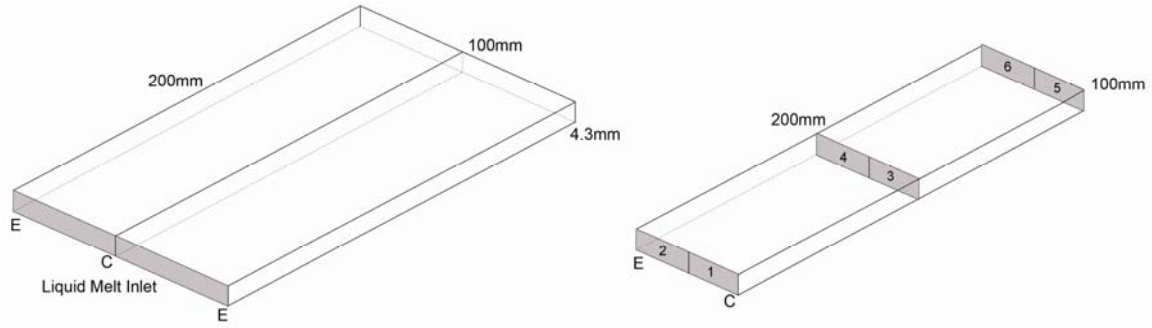

Figure 4.39: Sampling scheme for segregation characterization.

4.1.5.2 Metallographic Evidence of Inverse Surface Macrosegregation

Figure 4.40 depicts micrographs taken from various locations in type I, G, and M plates. These metallographic sections contain the thickness direction of the plates, which is the Y-axis of the micrographs. In these micrographs, the top contour is created by the intersection of the metallographic plane with the plate surface. The metallographic evidence suggests significant and profuse inverse macrosegregation at the surfaces of I, G, and M plates. On the other hand, significant macrosegregation is not observed at the surfaces of W plate specimens with the exception of a very few isolated locations.

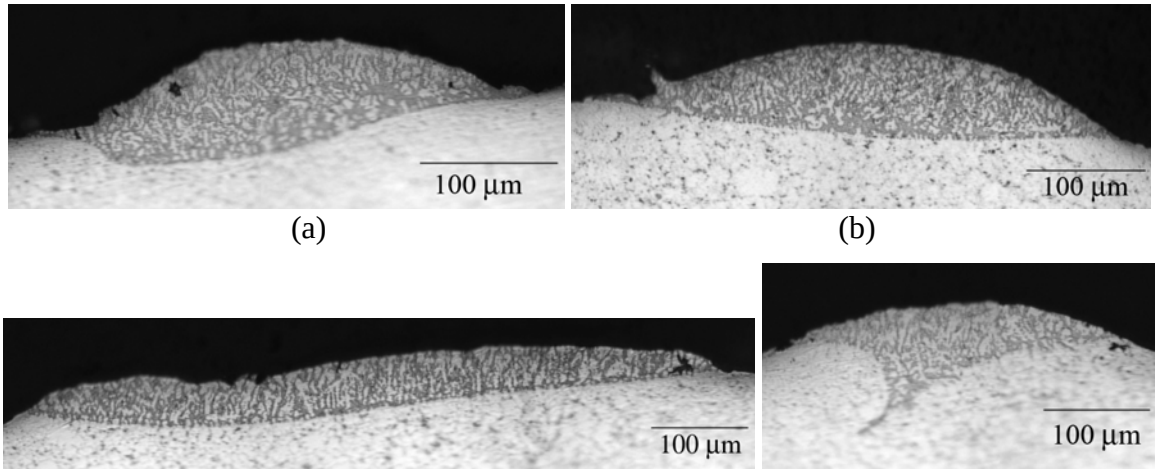

(a) (b)

(c) (d)

Figure 4.40: Metallographic evidence of inverse surface macrosegregation at various locations in the surfaces of I, G, M plate specimens. (d) Surface macrosegregation showing that interdendritic liquid has flowed to the surface.

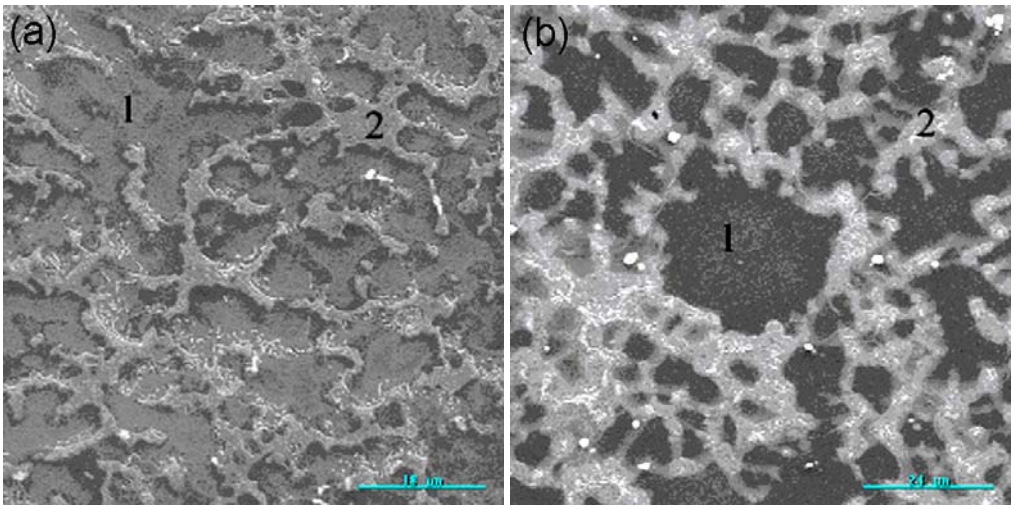

Figure 4.41: Microstructure of region with (a) and without (b) inverse surface macrosegregation observed in SEM depicting Mg-rich grain (1) and eutectic (2) constituents.

Table 4.4. Local percentage of Al in Mg-rich grains and eutectic in regions with and without segregation.

Location	% of Al in Mg-rich dendrites (1)	% of Al (Mg-rich dendrites + eutectic constituents) (2)
Inverse surface macrosegregation	6.9	16.0
No macrosegregation	2.0	6.1

Observe that in the inverse macrosegregation region (Figure 4.41a and Table 4.4), the percentage of Al is much higher in the Mg-rich dendrite grains as well as in the eutectic regions as compared to the corresponding constituents in the location without macrosegregation (Figure 4.41b and Table 4.4). Therefore, significant long-range compositional heterogeneity exists in the inverse surface macrosegregation regions detected by metallography in the three plates (I, G, and M). These observations reveal that a combination of high gate velocity, no intensification, and higher melt temperature (as in W plates) substantially decreases the tendency of inverse surface macrosegregation, whereas low gate velocity, and/or application of intensification pressure, and/or low melt temperature (as in I, G, and M plates) promote the inverse surface macrosegregation in the high-pressure die-cast AM60 alloy.

4.1.5.3 Quantitative Analysis of the Extent of Inverse Macrosegregation

To quantify the extent of inverse surface macrosegregation, the total number of inverse segregation regions and their average sizes were measured along each 25 mm and 80 mm segment along the width and length of the plates illustrated in Figure 4.39, to cover the complete width and length of the plates starting from the melt inlet. Interactive digital image analysis was used for these measurements. These data are reported in Tables 4.5 and 4.6.

Table 4.5. Frequency of inverse surface macrosegregation regions

Location	1 (Melt inlet)	2	3	4	5	6
Plate G	34	6	0	29	30	33
I	0	2	16	44	4	14
M	0	0	41	25	13	10
W	0	0	0	4	0	0

Table 4.6. Average area of inverse surface macrosegregation regions (in μm^2)

Location	1 (Melt inlet)	2	3	4	5	6
Plate G	2273	4732	-	2206	1293	1634
I	-	3500	2978	2066	1259	1232
M	-	-	5273	2089	1244	1076
W	-	-	-	2031	-	-

These data clearly demonstrate that a combination of high gate velocity, no intensification, or higher melt temperature (as in Plate W) substantially decreases the tendency of inverse macrosegregation in a HPDC AM60 alloy. On the other hand, low gate velocity (plate G), application of intensification pressure (plate I), and low melt temperature (plate M) facilitate the segregation. The observed effect of the application of intensification pressure on the macrosegregation is essentially due to the acceleration of the back flow of the solute-rich liquid through the interdendritic channels. However, more research is necessary to develop better understanding of the observed effects of gate velocity and melt temperature on inverse surface macrosegregation.

4.1.5.4 Porosity Distributions

It is important to recognize that the high-pressure die-cast Mg alloys also contain micro-porosity, and the amount of micro-porosity also depends on the HPDC process parameters. It is also known that the porosity adversely affects the mechanical properties of high-pressure die-cast Mg-alloys. Therefore, it is of interest to investigate whether the

combination of process parameters that significantly reduces the inverse surface macrosegregation tends to increase or decrease the amount of porosity. Figure 4.42 shows unetched microstructures of plate W (low macrosegregation) and plate G (high macrosegregation) depicting porosity.

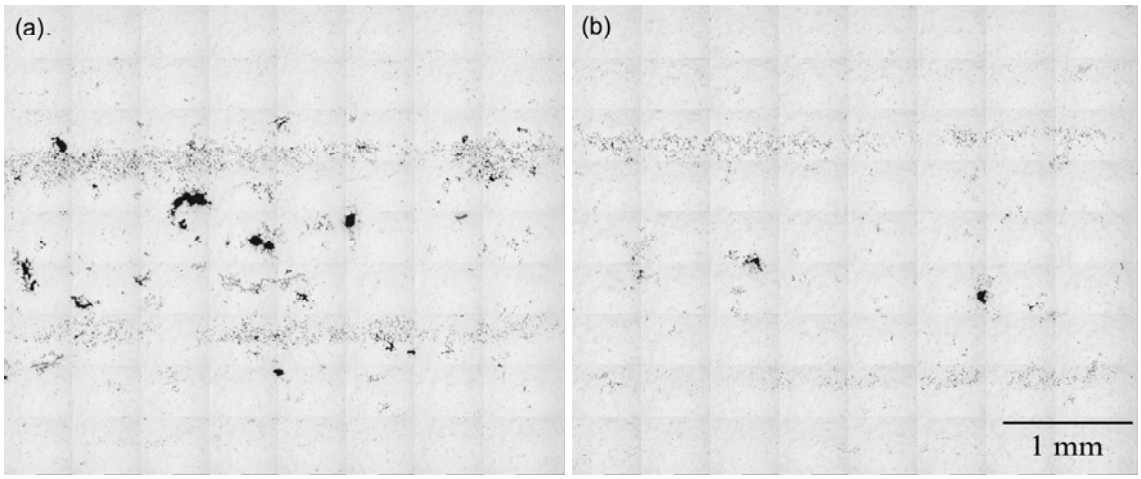

Figure 4.42: Gray scale montages for plate W (a) and G (b).

Observe that the amount of micro-porosity in plate W is significantly higher than that in other plates as shown in Table 4.2, although the extent of surface macrosegregation is significantly lower in plate W as compared to other plates. Therefore, the combination of process parameters that is observed to minimize the surface macrosegregation gives rise to higher levels of micro-porosity and vice versa. As both surface macrosegregation and micro-porosity adversely affect the mechanical properties, more research is required to identify the process conditions that can minimize both the surface macrosegregation and micro-porosity in high-pressure die-cast Mg-alloys. More detailed study on the effects of inverse surface macrosegregation is presented in the following chapter.

4.1.5.5 Fatigue Test Results

Figure 4.43 shows the plot of strain amplitude versus fatigue lives of the two sets of specimens at different strain amplitudes ranging from 0.1% to 0.6%. Observe that at the highest strain amplitude (0.6%, which is in the low cycle fatigue regime), the B-plate specimens having *lower* amount of micro-porosity have *lower* fatigue lives as compared to the W-plate specimens (that have a substantially higher amount of micro-porosity) tested at the same strain amplitude. The same trend is also observed at the lowest strain amplitude (0.1%, which is in the high cycle fatigue regime): the specimens having *lower* micro-porosity have *lower* fatigue lives. Further, the fatigue lives of the B-plate specimens are not substantially higher than those of the corresponding W-plate specimens at any intermediate strain amplitudes either. Obviously, there must be other microstructural factors (such as inverse surface macrosegregation) that are responsible for this unexpected trend.

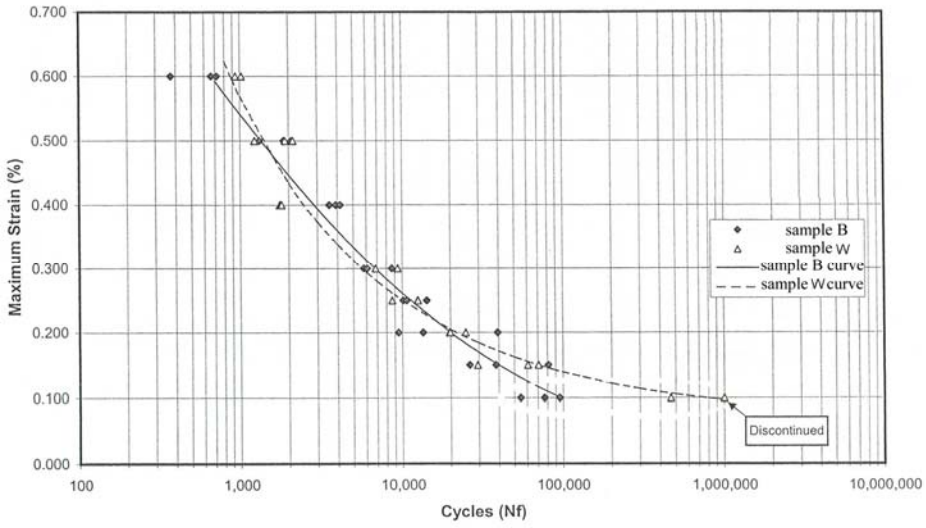

Figure 4.43: Semi-log plot of % strain amplitude versus number of cycles to failure.

To understand the fatigue fracture mechanisms and the microstructural effects, the fracture surfaces of the fatigue test specimens were examined using a scanning electron microscope (SEM). Figure 4.44a and b depict the general appearance of the fracture surfaces of the two specimen types. The amount of porosity in the fracture surface of B specimens (having lower fatigue life) appears to be lower than that in the W specimens having higher fatigue lives. Therefore, the internal porosity is not responsible for the differences in the high cycle fatigue lives for two types of specimens. In both specimen types, fatigue fracture zones are not well defined, but B specimen has more crack initiation sites as compared to the W specimens. To understand the fatigue fracture mechanisms and the microstructural effects, the fracture surfaces of the fatigue test specimens were examined using SEM fractography. Figure 4.44c depicts fracture surface of a fatigue specimen from B-plate. Observe that (1) the fatigue crack initiation is at the boundary between macrosegregation regions at the surface of the specimen, and (2) there is no significant amount of porosity in the fatigue fracture region. All fatigue specimens from B-plates exhibited similar fractographic trends. The role of macrosegregation is further illustrated in Figure 4.45, which shows the region of a metallographic plane near the fatigue fracture surface of fatigue specimen from B-plate. Observe that numerous secondary fatigue cracks are formed at the boundaries of the macrosegregation regions below the fracture surface. The macrosegregation at the bottom surface of the fatigue specimen is also clearly revealed. These observations indicate that the presence of macrosegregation on the cast surfaces can lead to an early initiation of fatigue cracks as compared to the initiation due to internal microporosity due to high slip incompatibility. The slip incompatibility arises because the macrosegregation regions contain large amounts of brittle intermetallic eutectic constituents such as $Mg_{17}Al_{12}$ intermetallic compound that have low plasticity as compared to the Mg-rich dendrite that can exhibit high local plasticity in certain orientations.

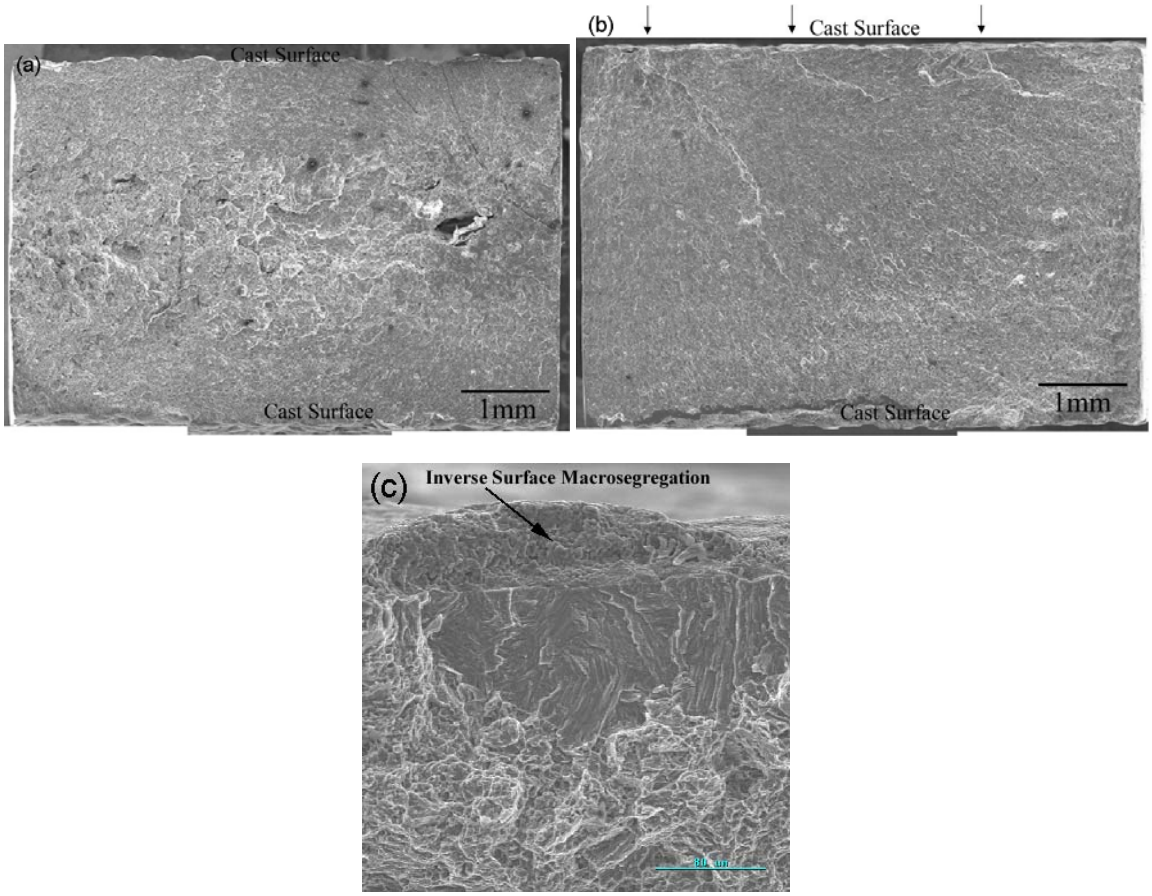

Figure 4.44: Overall fracture surfaces of sample A (a) and B (b). Arrows indicate the location of the fatigue crack initiation sites. (c) Magnified view of crack initiation site.

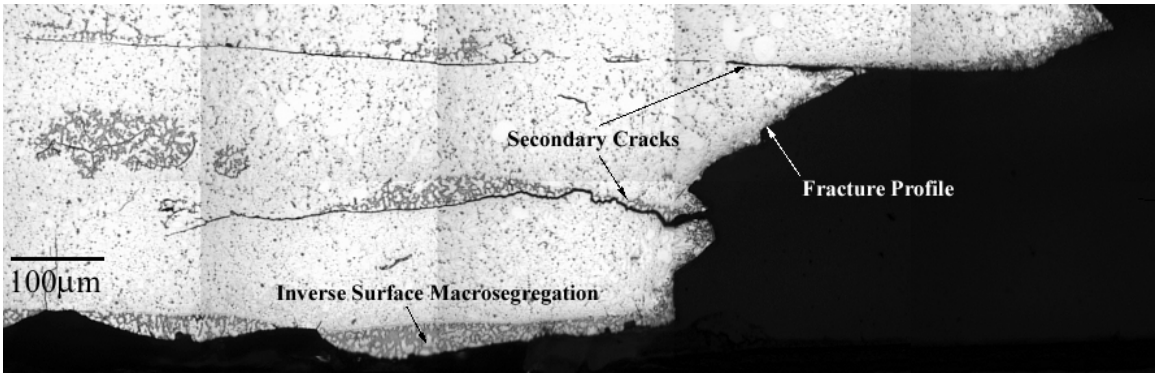

Figure 4.45: Metallographic section through a fatigue specimen from B-plate. The fracture profile is on the right hand side. Observe the secondary cracks at the boundaries of inverse macrosegregation regions just below fracture surface. The inverse surface macrosegregation is also clearly revealed at the bottom surface of the specimen.

Therefore, for higher fatigue life, it is essential to minimize *both* micro-porosity and macrosegregation in the high-pressure die-castings of the Mg-alloys. Unfortunately, the combination of process parameters (low gate velocity, intensification, and low melt temperature) that leads to a significantly lower micro-porosity in these die-castings appear to facilitate inverse macrosegregation at the cast surfaces, which substantially diminishes the beneficial effects of lower micro-porosity levels on the fatigue life.

4.1.5.6 Summary and Conclusions

Under certain process conditions, extensive inverse surface macrosegregation can occur in high-pressure die-cast AM60 Mg-alloy. The combination of process parameters such as lower gate velocity, application of intensification, or lower liquid melt temperature that usually leads to lower micro-porosity gives rise to a substantially higher extent of inverse macrosegregation on the cast surfaces of this alloy, which can adversely affect the fatigue life. The combination of process parameters that usually leads to lower micro-porosity gives rise to higher extent of the macrosegregation to an extent where the beneficial effects of lower micro-porosity on the fatigue life are swamped by the detrimental effects of the inverse surface macrosegregation. Therefore, it is essential to minimize *both* micro-porosity and macrosegregation in the high-pressure die-castings of the Mg-alloys.

4.2 Reconstruction and Visualization of Three-Dimensional Microstructure

Visualization and representation of three-dimensional (3D) pore morphologies in the high pressure die cast Mg-alloys are of significant interest for understanding and modeling processing-microstructure-properties relationships. Main objective of 3D reconstruction of microstructure is first to study detailed 3D morphologies and spatial correlations of gas and shrinkage pores. For detailed study on porosity morphologies and spatial correlations, an efficient and unbiased montage serial sectioning technique is

applied for reconstruction of large-volume (~ 1.24mm^3) high-resolution (~ 1μm) 3D microstructure taken from the center of AM50 thick plate W. The reconstructed 3D microstructure can be implemented in a 3D finite elements (FE) computational framework to illustrate how realistic complex microstructural feature morphologies can be incorporated in the simulations of micromechanical response of these high-pressure die-cast cast microstructures. Another 3D microstructure reconstruction experiment has been performed on AE44 HPDC specimens to reveal detailed morphologies, geometry, and spatial correlations of microstructural constituents such as dendrites and Al-RE rich intermetallic particles in the inter-dendritic eutectic regions.

4.2.1 Three-Dimensional Reconstruction of AM50 Alloy

Figure 4.46a shows a digitally compressed montage of 225 fields of view (FOV) grabbed at 200×.

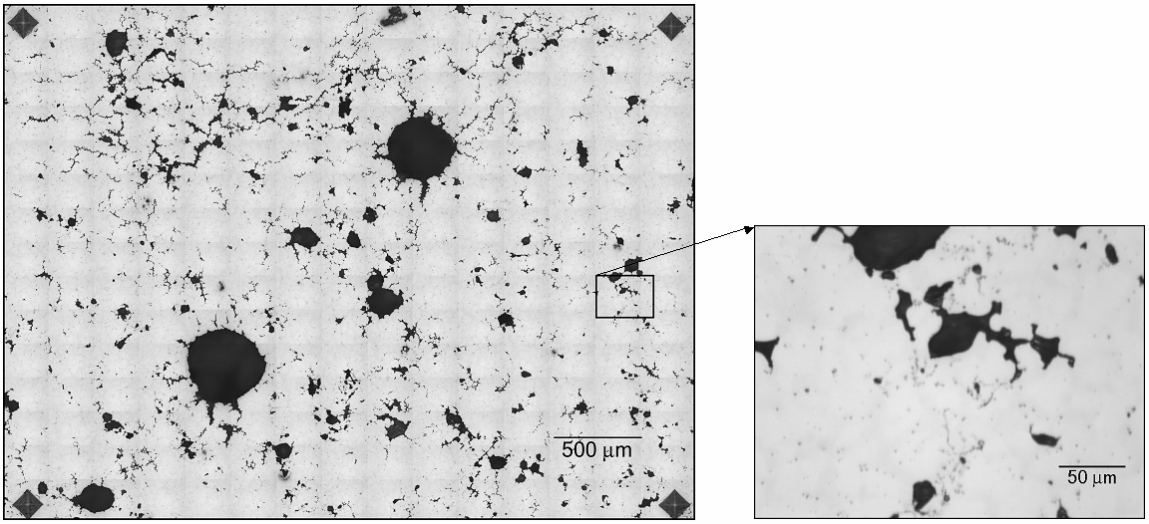

(a) (b)

Figure 4.46: (a) Montage of 225 fields of view covering an area of 12.4 mm^2 created by matching contiguous microstructural fields grabbed at a resolution of 0.5 μm. The montage is digitally compressed for presentation. Each field of view of the montage has been grabbed at the resolution of the image shown in (b).

Each region of this montage has a high resolution of the image shown in Figure 4.46b. Therefore, such a montage is a microstructural image of a large area (~12.4 mm^2) having a high resolution. In the present work, the 3D microstructure visualization has been done using such 100 aligned montage serial sections. Therefore, the resulting 3D data sets are useful for characterization and visualization of both short range and long-range spatial dispersion of the micro-pores.

Figure 4.47a shows a stack of aligned 20 montage serial sections for the cast microstructure, where each serial section is a digitally compressed montage of 169 contiguous microstructural fields. Observe that gas pores (equiaxed) and shrinkage pores are inter-connected. Figure 4.47b is the magnified view of that bordered region, where each section is exactly the stack of serial sections generated by the classical serial sectioning technique. This is the magnification at which all microstructural fields have been grabbed. In Figure 4.47b, observe the changes in the sizes of the micro-pores at the edges of these serial sections as well as appearance and disappearance of the smaller pores in the successive serial sections. Figure 4.48a shows a segment of volume rendered 3D microstructure. The volume rendered visualization is useful for implementation of the 3D microstructural images in the finite elements (FE) based computations of the micro-mechanical response. Figure 4.48b shows a segment of surface rendered 3D microstructure depicting gas and shrinkage pores, whereas Figure 4.48c depicts another type of surface rendering of 3D microstructure, where the matrix is effectively removed from the microstructure leaving behind only the pores. Note that the 3D microstructure displayed in Figure 4.48 is only about 2% of the actual 3D microstructural volumes contained in the 100 montage serial sections. These figures clearly show the complexity of the porosity shape and random spatial arrangement of the gas (air) and shrinkage porosity. In this cast microstructure, most of gas (air) and shrinkage pores are connected, except a few that is in very small size ranges.

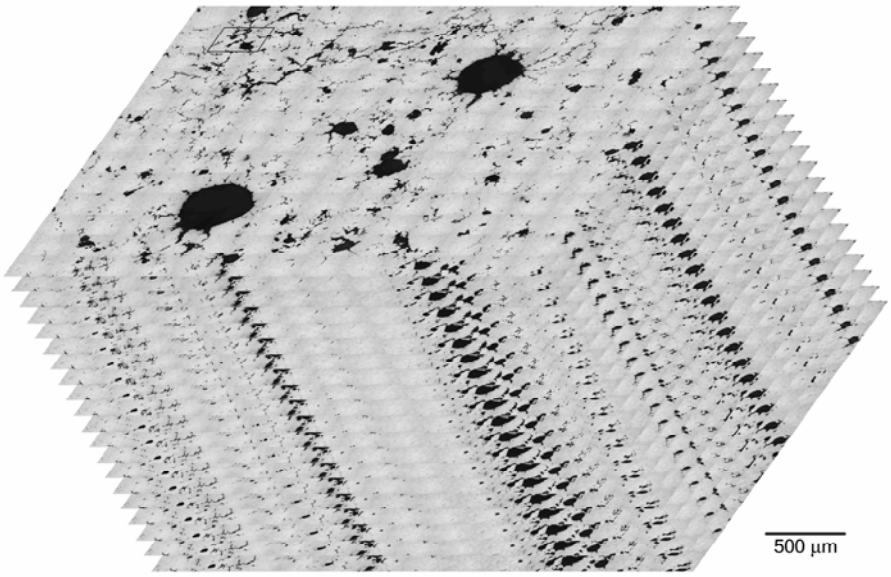

(a)

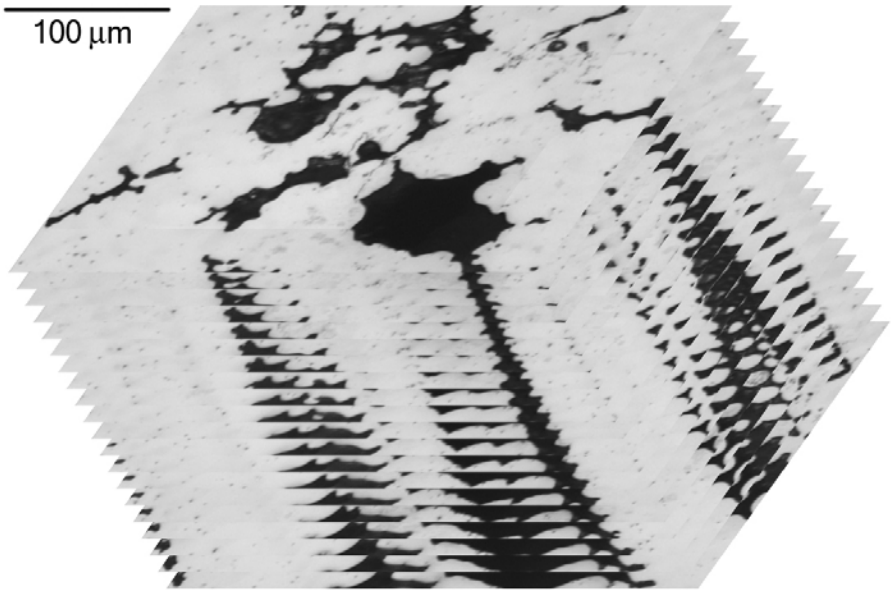

(b)

Figure 4.47: (a) Stack of 20 montage serial sections for the cast microstructure. Each serial section montage contains 169 contiguous microstructural fields. (b) The magnified view of the small-bordered region of the stack of 20 montage serial sections for the cast microstructure. This is the resolution of the individual microstructural fields.

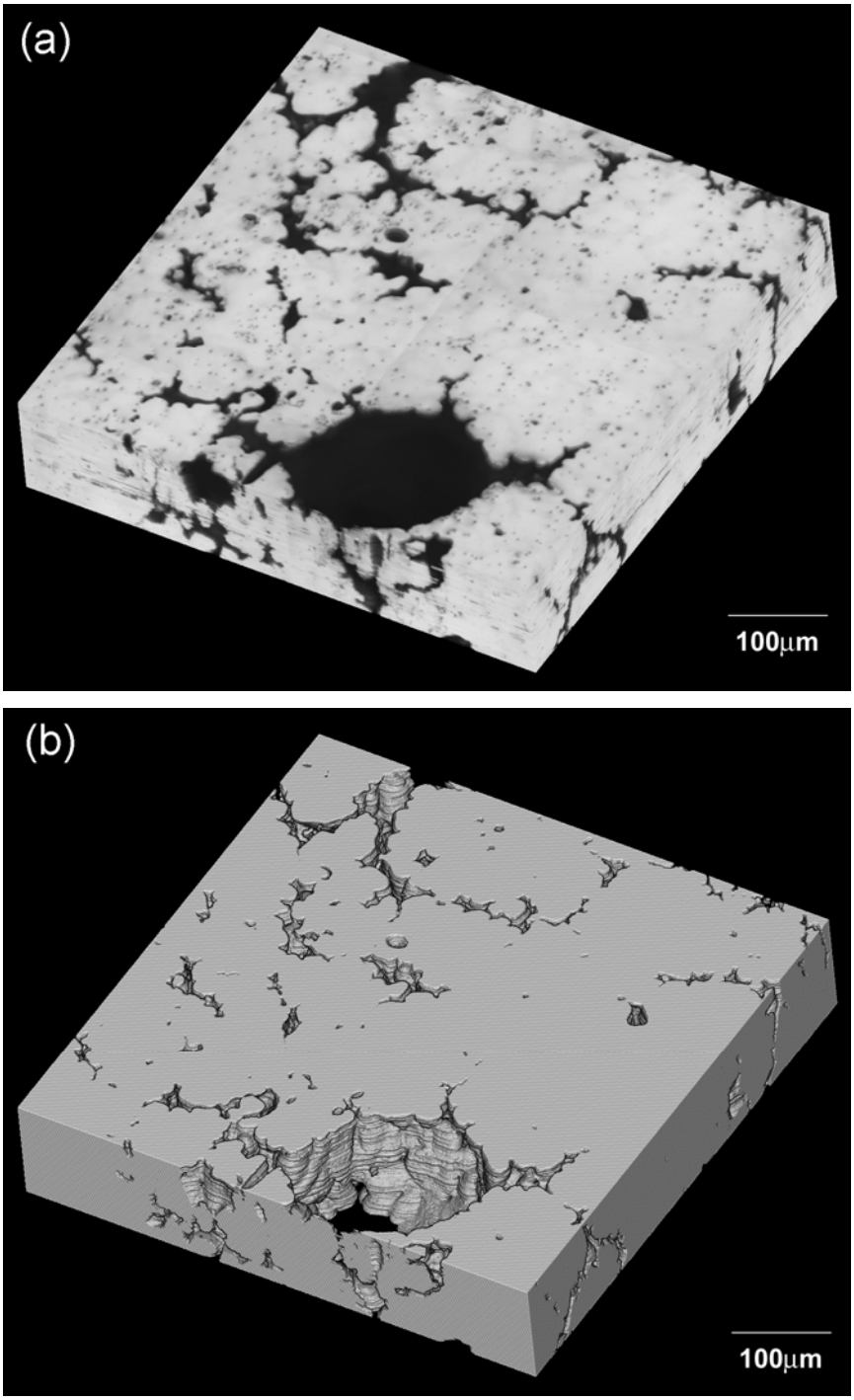

Figure 4.48: (a) A small segment of volume-rendered reconstructed 3D microstructure, (b) A surface-rendered reconstructed 3D microstructure, where the porosity is removed leaving behind just the matrix of volume-rendered reconstructed 3D microstructure.

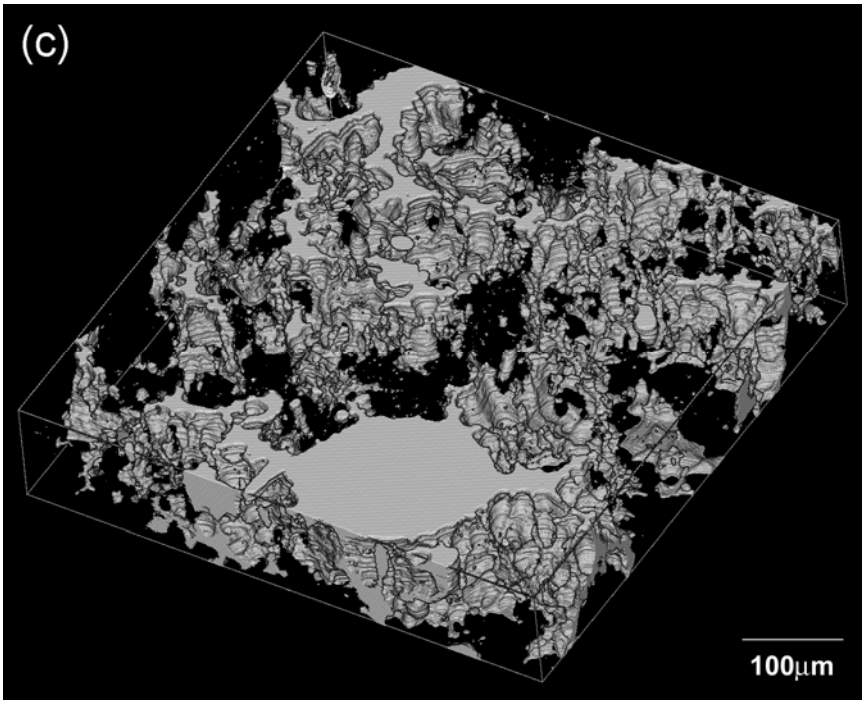

Figure 4.48: (c) inverted-contrast surface-rendered reconstructed 3D microstructure depicting porosity.

The high-resolution of montage serial sections and large volume permits extraction of individual pores from the 3D microstructure for a more detailed study. Figure 4.49a and b display typical individual gas (air) and shrinkage pore morphologies extracted from the 3D microstructure. Figure 4.49c displays one of connected porosity. The quantitative measurements reveal that gas (air) porosity in Figure 4.49a is on the 90 μm long, average 1066 μm^2 in the cross-sectional area, and 95940 μm^3 in volume. Such information on the porosity is extremely useful for understanding the effects of process parameters on the many attributes of porosity and for modeling virtual microstructures, and it can be obtained only from large-volume high-resolution 3D microstructure generated by a stack of montage serial sections: classical serial sectioning is not useful for this purpose. The complexity of the pore morphologies, spatial connectivity and their spatial arrangement reveal that 2D microstructural observation and/or some quantitative measurements for porosity may seriously underestimate the real three-dimensional

porosity size and spatial distribution. Further, the reconstructed 3D microstructure can serve as a representative volume element in the FE-based computational simulations of mechanical response as described in the chapter 4.1.4.4.

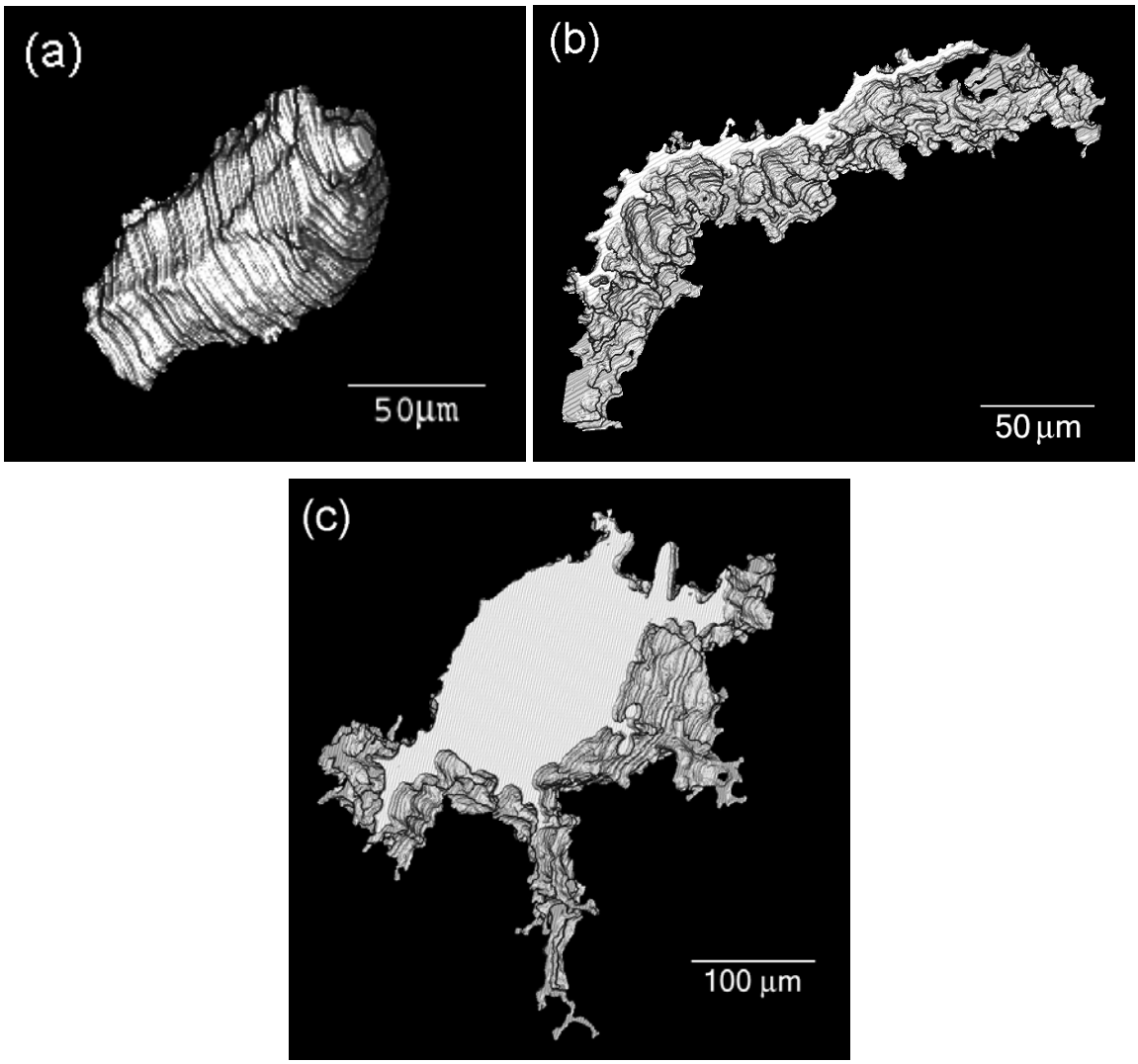

Figure 4.49: (a) Three-dimensional morphology of individual gas (air) and (b) shrinkage porosity extracted from the surface rendered three-dimensional image. (c) Three-dimensional morphology of connected porosity extracted from the surface rendered three-dimensional image.

4.2.2 Three-Dimensional Reconstruction of AE44 Alloy

Majority of the Mg-alloy high-pressure die-castings are made from Mg-Al base (AM series) and Mg-Al-Zn base (AZ series) alloys, which are suitable for structural automotive components that do not experience elevated temperatures in service. As AM and AZ series alloys do not have adequate high temperature strength and creep resistance above 400 K, they are not suitable for automotive components that operate at elevated temperatures [82, 83]. Consequently, cast Mg-alloys that have improved creep resistance and bolt load retention properties are required for such applications. Addition of rare earth elements (RE) such as Ce and La are known to improve creep resistance and corrosion resistance of Mg-Al base alloys [84]. As mischmetal (MM), standard grade Cerium-based alloy (>50% Cerium) with Lanthanum (20-35%), Neodymium (10-20%), and Praseodymium (4-10%), is an economical way of adding such beneficial alloying elements, AE series of Mg-Al-RE base casting alloys such as AE42 were developed in the 1990s [85]. Recently, Hydro Magnesium developed a new high-pressure die-casting alloy, AE44, which has attractive high temperature mechanical properties, as well as die-castability, and corrosion resistance [86]. The specimen is drawn from a prototype HPDC AE44 front engine cradle. The microstructure contains cored α-Mg-rich dendrites that are surrounded by grain boundary region containing eutectic phases consisting of Al-RE intermetallic compounds. In the present HPDC alloy both $Al_{11}RE_3$ and Al_2RE type intermetallic compounds are present. In the HPDC AE44 alloy, the intermetallic compounds mostly contain Ce and/or La rare earth elements. Not much information is available on the 3D morphologies of porosity and these intermetallic compounds. Therefore, it is of interest to reconstruct the 3D microstructures of the porosity, dendrites, and eutectic constituents in the HPDC AE44 alloy.

For the reconstruction of 3D porosity, sample is taken from the grip section of the AE44 tensile sample and the montage serial sections have been grabbed at 100×

magnification without etching. Whereas the length scale of the dendrites and eutectic constituents in the HPDC AE44 alloy are on the order of 1 to 20 μm, and consequently, the montage serial sections have been grabbed at a much higher magnification (1000×). Every serial section has been etched at room temperature using acetic glycol etching agent to reveal the grain structure, eutectic constituents, and intermetallic compounds at the grain boundaries.

Figure 4.50a and b show a segment of surface rendered 3D microstructure for magnesium matrix and porosity. It is important to recognize that 3D morphologies of porosity in AE44 alloy appear to have quite spherical shape and little porosity appears to be shrinkage, which are very different from those in AM50 alloy. It is expected to be related to the size of mushy zone range and the formation temperature of intermetallic compounds and the extent of latent heat generated as they form. The spherically shaped porosity is advantageous from a fracture related mechanical properties standpoint since they have a more beneficial effect on retarding the initiation and evolution of the damage.

Figure 4.51a depicts a volume rendered 3D microstructure. On the other hand, Figure 4.51b depicts the surface rendered 3D microstructure containing only the Mg-rich dendrites: in this image the inter-dendritic eutectic regions have been removed via image editing routines. The spatial distribution of the inter-dendritic eutectic regions is revealed in the surface rendered image shown in Figure 4.51c, where the dendrites are removed using image-editing routines. Figure 4.51d shows spatial distribution of the Al-RE rich intermetallic compounds present in the inter-dendritic regions depicted in Figure 4.51c. The 3D morphologies of the inter-dendritic eutectic regions and the rare earth rich intermetallic compounds are clearly revealed in the surface rendered 3D images shown in Figure 4.51c and d. Figure 4.52 shows a typical single colony of the rod-like inter-connected Al-RE rich intermetallic compound particles present in the inter-dendritic eutectic regions. Observe that these particles of the inter-metallic compounds have very high topological connectivity that leads to “tree-like” morphology of the colony.

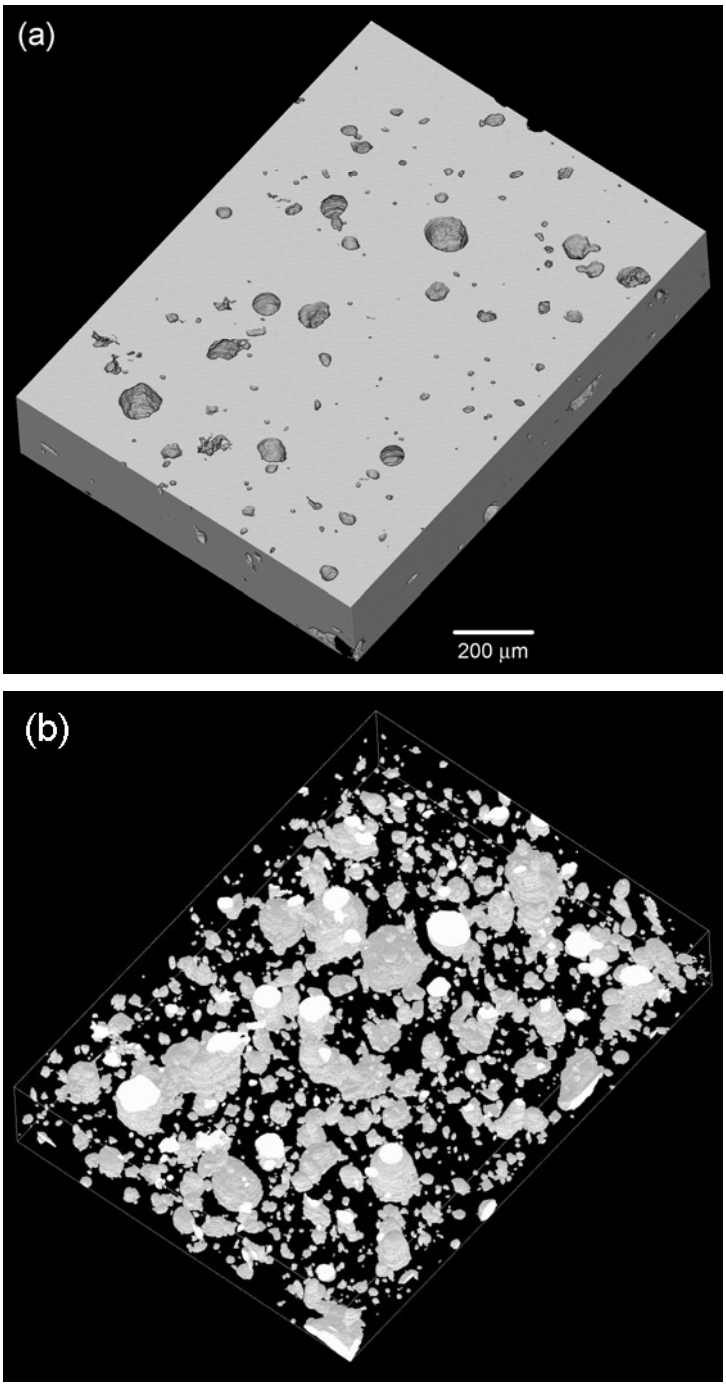

Figure 4.50: (a) A surface rendered 3D microstructure for matrix and (b) An inverted contrast 3D microstructure depicting porosity.

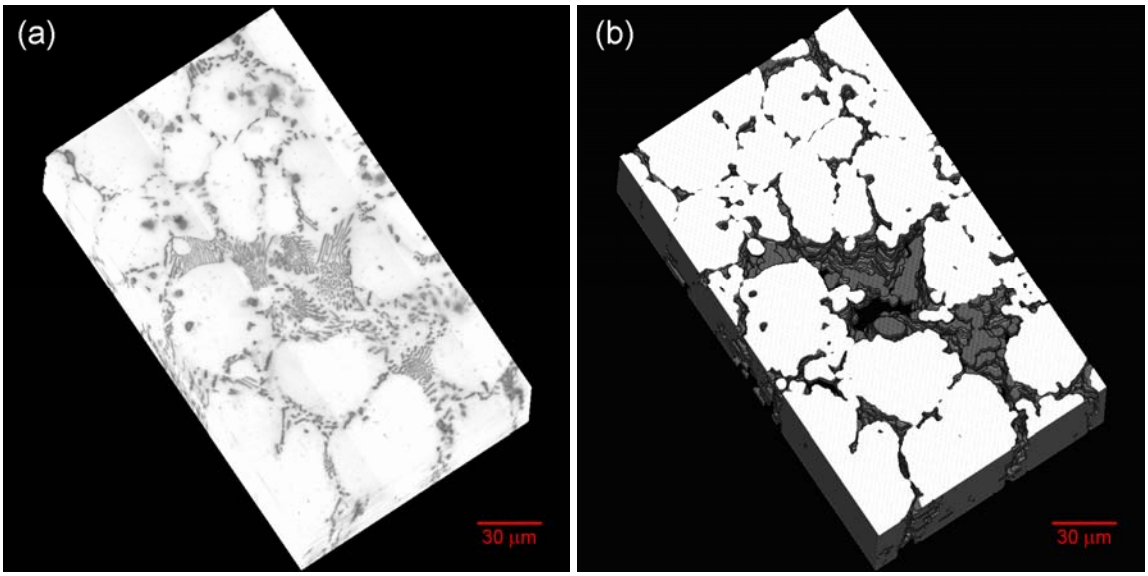

Figure 4.51: (a) Volume rendered reconstructed 3D microstructure and (b) surface rendered 3D microstructure showing Mg dendrites.

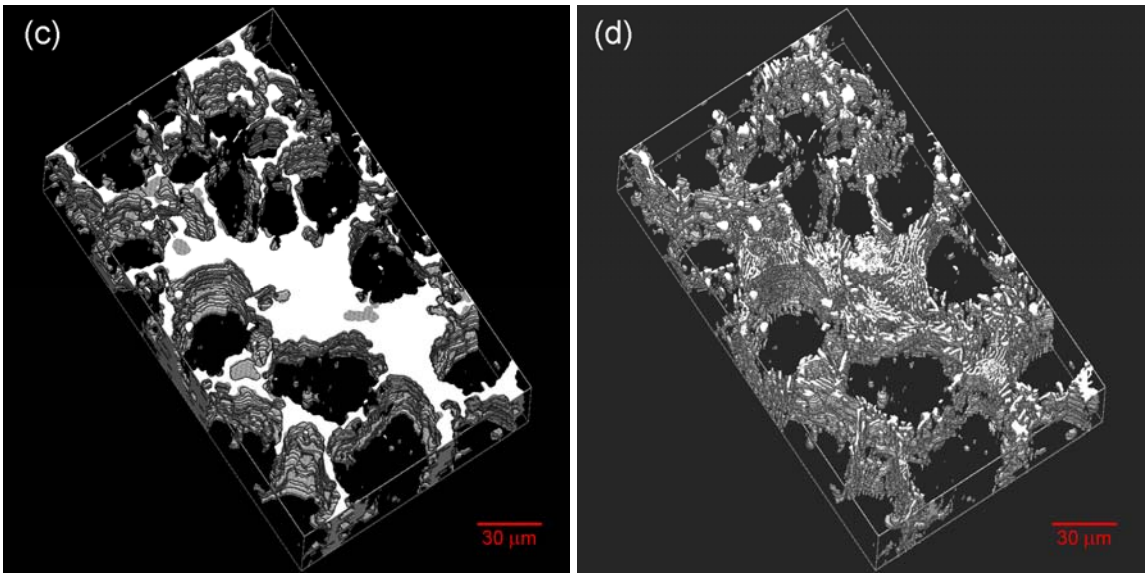

Figure 4.51: (c) Surface rendered 3D microstructure depicting interdendritic eutectic regions and (d) 3D microstructure depicting Al-RE rich intermetallic compounds present in the inter-dendritic regions.

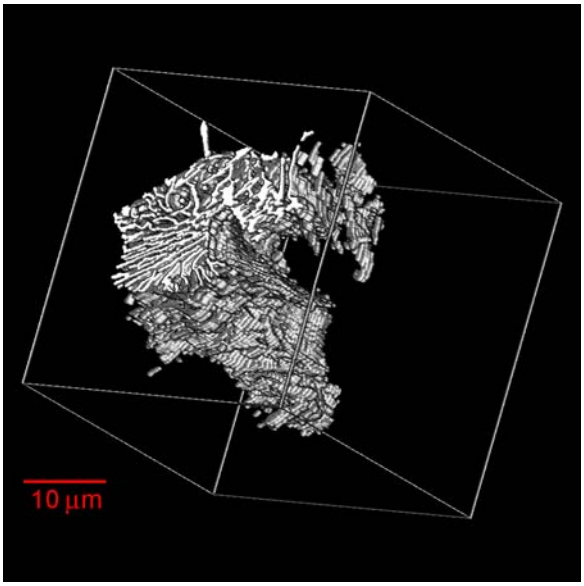

Figure 4.52: A typical single colony of the rod-like inter-connected Al-RE rich intermetallic compound particles present in the inter-dendritic eutectic regions.

Clearly, the usual concepts of shape and size do not apply to such morphological and topologically complex microstructural features. Note that the volume segments shown in Figures 4.51 to 4.52 constitute only a small fraction of the total 3D volume that can be reconstructed from the present stack of the montage serial sections. Statistically robust quantitative data on the 3D volume distribution of the colonies of the Al-RE rich intermetallic compounds, volume distribution of the Mg-rich dendrites, etc can be obtained from such large-volume high-resolution aligned montage serial sections and the 3D images.

4.2.3 Summary on the Three-Dimensional Microstructure Reconstruction

An efficient and unbiased montage serial sectioning technique has been applied for reconstruction of large-volume high-resolution 3D microstructures of high-pressure die-cast AM50 and AE44 Mg-alloys. The reconstruction of 3D microstructures from montage serial sections enables visualization and characterization of detailed 3D morphologies and spatial correlations of gas and shrinkage porosity and dendrite and

eutectic phases. In particular, 3D morphologies of porosity in AE44 alloy appear to have quite spherical shape and little porosity appears to be shrinkage, which are very different from those in AM50 alloy. The spherically shaped porosity in AE44 alloy is advantageous from a fracture related mechanical properties standpoint since they have a more beneficial effect on retarding the initiation and evolution of the damage.

The reconstructed 3D microstructure is implemented in a 3D finite elements (FE) computational framework to illustrate how realistic complex microstructural feature morphologies can be incorporated in the simulations of micromechanical response of these high-pressure die-cast cast microstructures.

4.3 Mechanical Properties of Mg-Alloys

Microporosity and other casting defects appear to adversely affect the mechanical properties of the HPDC Mg-alloys and may lead to significant variability in their fracture sensitive mechanical properties such ductility, fatigue life, and toughness. Therefore, a systematic study of the correlations between the variability in the microstructure and the corresponding variability in the relevant fracture related mechanical properties of HPDC AE44 Mg-alloy is of significant interest. Consequently, the central goal of this chapter is to explore the correlations between the variability in the tensile ductility of AM50 and AE44 HPDC Mg-alloys and the geometric attributes of the micro-porosity present in the corresponding tensile fracture surfaces using quantitative fractographic techniques. And then a new technique to simulate the microstructures with different degrees of porosity distribution by controlled parameters having realistic complex morphologies has been presented.

4.3.1 Variability in the Tensile Ductility of Mg-Alloys

Although amount of micro-porosity appears to adversely affect the tensile ductility of HPDC Mg-alloys, attempts to establish *quantitative* correlations between the

average amount of porosity in the *bulk* microstructure and fracture sensitive properties such as strength or ductility have often failed [13, 24, 66]. On the other hand, the amount of porosity observed in the *fracture surfaces* of tensile test specimens shows strong quantitative correlation with the fracture sensitive mechanical properties of HPDC AM50, AM60, and AZ91 Mg-alloys [66-67], which is similar to that observed in numerous cast Al-alloys [68-71]. For this purpose, the tensile tests have been performed on HPDC AM50 and AE44 alloy specimens at room temperature.

4.3.1.1 Mechanical Properties of AM50 and AE44 Alloys

Figure 4.53a shows typical true-stress (σ) versus true-strain (ε) curves of the high-pressure die-cast AM50 and AE44 alloys at room temperature. Figures 4.54b depicts the ln (σ) versus ln (ε) curves for the plastic part of the flow curves. The non-linearity of the plots in Figure 4.53b reveals that in the HPDC AM50 and AE44 alloys, the flow curve does not follow a simple power law equation often assumed in numerous theoretical models. It is well known that both slip and twinning contribute to plastic strain in Mg-alloys. Further, prism and pyramidal secondary slip systems become active at moderately elevated temperatures and/or at higher stresses. The relative contributions of the slip on primary basal slip system, secondary slip systems, and the twinning to the total global plastic strain varies with plastic strain and temperature, and therefore, work hardening rate varies with strain in a complex manner. Consequently, the flow behavior cannot be described by a simple power law type equation. As will be seen later, this has a bearing on the interpretation of the correlation between tensile ductility and fractographic attributes. Table 4.7 gives the data on the variability in the ductility, UTS, and yield stress of the tensile test specimens. Note that these specimens have the same average chemical composition and they were high-pressure die-cast using the same process parameters, and yet there is a significant specimen-to-specimen variability in the tensile ductility.

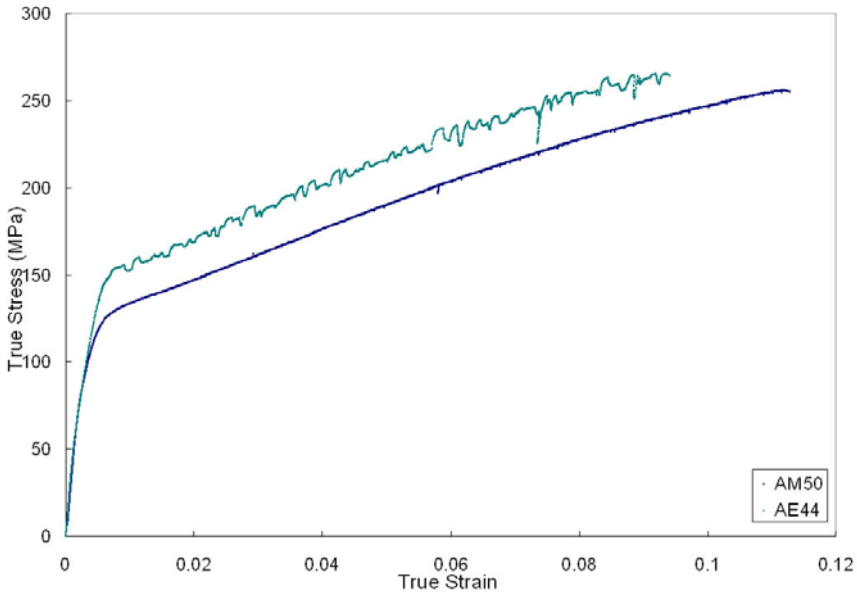

(a)

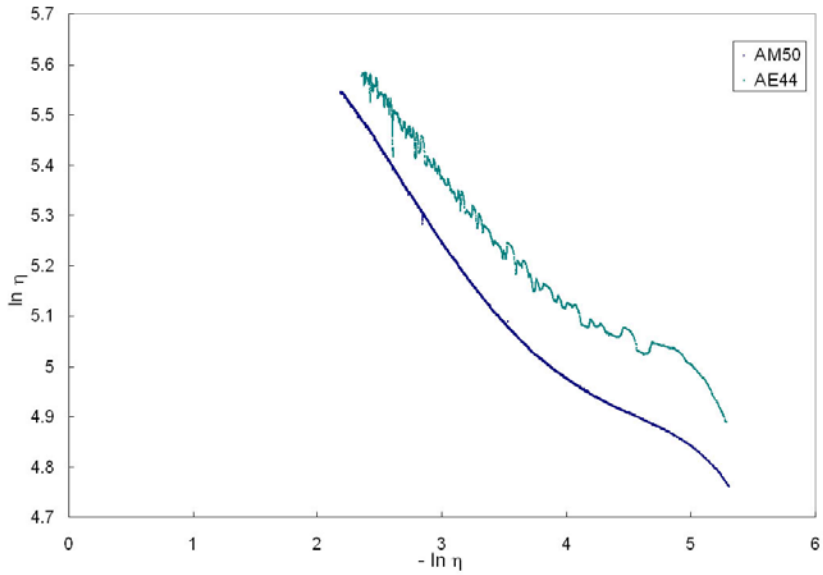

(b)

Figure 4.53: (a) True stress-strain curves of the alloy at room temperature and (b) lnσ vs. lnε curves for the plastic part of the flow curves

Table 4.7. Tensile properties of AM50 and AE44 specimens at room temperature.

	AM50			AE44		
Sample ID.	YS (MPa)	UTS (MPa)	%El	YS (MPa)	UTS (MPa)	%El
1	115.1	224.8	10.7	135.1	237.9	7.1
2	115.8	233.0	12.1	128.3	233.7	6.1
3	109.6	209.6	8.9	131.0	242.7	8.2
4	115.8	228.9	11.9	136.5	252.4	13.1
5	114.5	228.9	11.3	135.1	242.7	10.2
6	115.1	244.8	17.1	138.6	253.7	11.1
7				131.0	244.8	7.1
8				130.3	251.7	10.1
9				143.4	242.7	7.1
10				135.1	239.3	8.2
11				137.2	243.4	5.1
12				135.8	228.9	6.1
13				132.4	255.8	12.1
14				135.1	237.9	9.2
15				135.1	248.9	9.1

At room temperature, the tensile ductility varied from 8.9 % to 17.1 % in AM50 alloy and from 5.1% to 13.1% in AE44 alloy. There is some variability in the UTS as well, but the yield stress is about the same for the specimens tested.

4.3.1.2 Microstructural Observations

Figure 4.54 and 55 depict unetched microstructures of the AM50 and AE44 tensile test specimens. The microstructure pertains to a metallographic plane containing the applied stress and it is in the gage length region of the specimen. Shrinkage and gas porosity is observed in the microstructure, in particular, porosity defect band is observed in the AM50 microstructure. The gas porosity is primarily due to the trapped air in the die cavity during the high-pressure die-casting process and dissolved gases in the liquid alloy,

whereas shrinkage porosity is due to lack of liquid metal feeding the volume changes due to solidification. The shrinkage pores have crack-like morphologies, whereas the gas pores have equiaxed morphologies and they are larger in size. Table 4.8 gives the volume % of porosity in some of the tensile test specimens and their tensile ductility data. There appears to be no *quantitative* correlation between the average amount of porosity in the bulk microstructure and the tensile ductility in AM50 and AE44 alloys.

Table 4.8. Tensile ductility and bulk porosity in some of tensile test specimens

AM50			AE44		
Sample ID	Tensile Ductility (%)	Total Porosity (%)	Sample ID	Tensile Ductility (%)	Total Porosity (%)
1	10.7	0.8	4	13.1	0.4
2	12.1	3.1	6	11.1	0.9
3	8.9	1.4	10	8.2	0.6
4	11.9	1.1	11	5.1	0.6
5	11.3	1.7			
6	17.1	1.9			

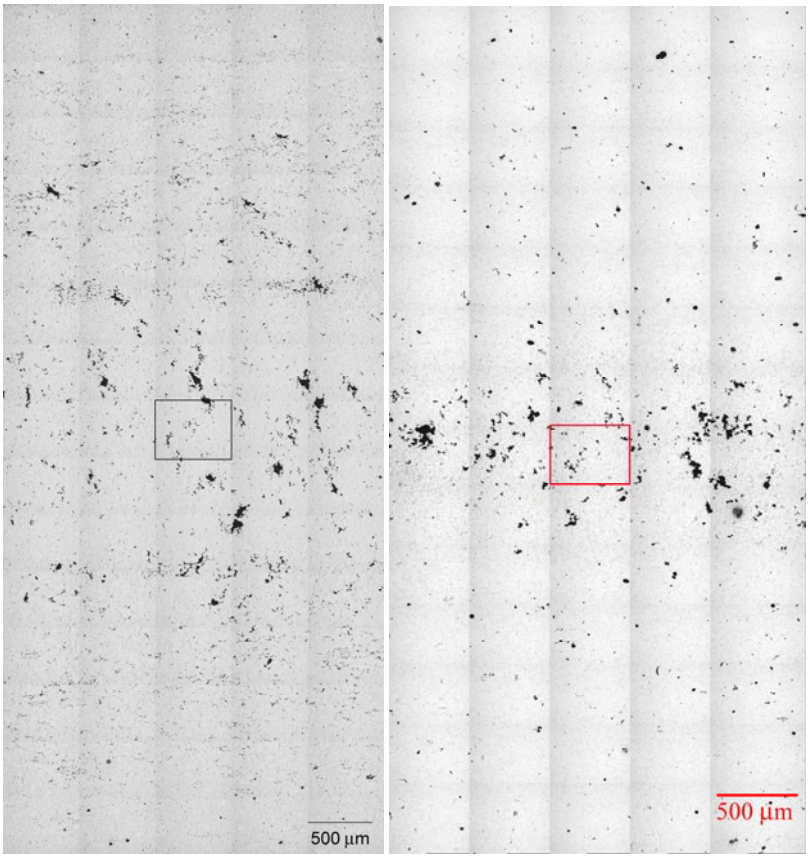

(a) (b)

Figure 4.54: Digitally compressed seamless montages of 75 contiguous microstructural fields of AM50 (a) and of 70 microstructural fields of AE44 (b) covering the complete thickness (y-axis).

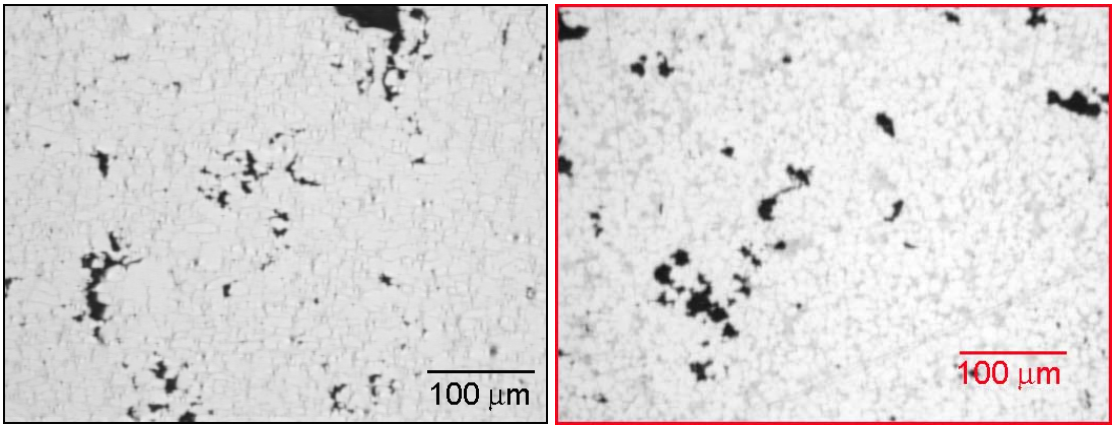

(a) (b)

Figure 4.55: (a) and (b) Enlarged one field of view of the small window in Figure 5.54

4.3.1.3 Relationship between variability in tensile ductility and fractographic parameters

Figure 4.56 shows a plot of ductility versus amount of porosity in the corresponding fracture surface for the specimens tested at room temperature, which demonstrates a quantitative correlation between these quantities. Figure 4.57 shows the variation of tensile ductility (as represented by % plastic elongation to failure), *e*, versus the area fraction of porosity f observed in the fracture surface of the corresponding specimen, plotted in the format of ln (*e*) versus {-ln (1-f)}. Interestingly, the data show quantitative correlation between the tensile ductility *e* and the area fraction of porosity f in the corresponding fracture surface. The trends in Figure 4.57 can be represented by the following simple equation.

$$e = e_0 [1 - f]^m \quad (1)$$

In equation (1), e_0 and exponent m are empirical constants. Table 4.9 gives the values of e_0 and *m* at the two alloys.

Table 4.9. Values of parameters e_0 and m at AM50 and AE44 alloys

	AM50	AE44
e_0	29	15.8
m	10.3	34.7

Interestingly, e_0 increases significantly with temperature. It is tempting to interpret e_0 as the ductility of a pore-free alloy having the same remaining microstructure, but it may not be true. This is because at very low porosity levels, some other competing damage accumulation mechanism may become dominant (for example, cracking of eutectic constituents and void growth around cracked particles), and consequently, equation (1) may not be applicable. Caceres and Selling [89] have given an equation similar to equation (1) that expresses quantitative correlation between the tensile ductility

and amount of porosity in the fracture surfaces observed in some Al-alloys (which is based on earlier contributions of Bourcier, et al. [90] and Marciniak and Kuczinski [91]).

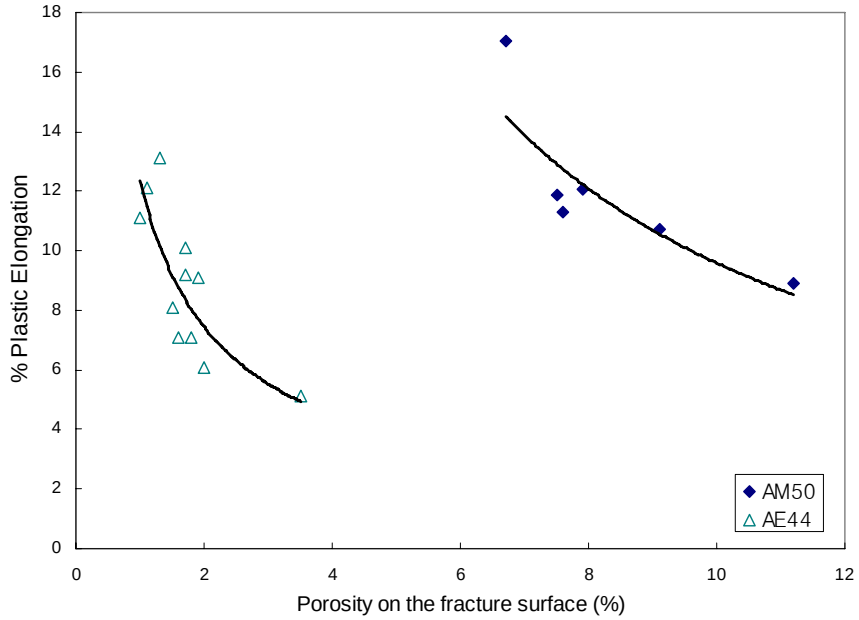

Figure 4.56: Tensile ductility versus amount of porosity in the fracture surface for the specimens tested at room temperature.

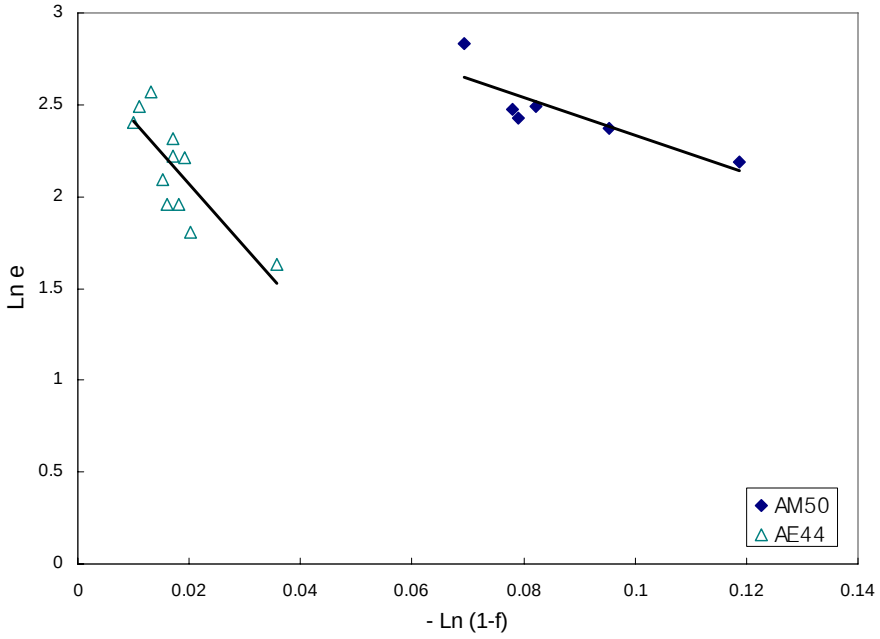

Figure 4.57: Variation of tensile ductility versus area fraction of porosity in the *fracture surface* plotted as [Ln (e)] versus [-Ln (1-f)].

However, Caceres and Selling's model [89] assumes that the tensile flow curve of the alloy can be represented by a simple power law equation, which is certainly not the case for the present HPDC Mg alloys as documented in Figures 4.53. Therefore, more research is needed to establish the theoretical basis for the correlation represented by equation (1) in the HPDC Mg-alloys where the tensile flow curves cannot be represented by simple power law equation.

The present data reveal that the amount of porosity present in the fracture surfaces of the tensile test specimens is significantly higher than the average volume fraction of porosity in the bulk three-dimensional microstructure. Therefore, it is reasonable to conclude that the fracture path preferentially goes through the regions of the specimens containing large amount of localized (clustered) shrinkage and gas porosity. The quantitative correlation between the tensile ductility and the area fraction of the porosity in the fracture surfaces strongly supports this hypothesis. Therefore, the ductility of high-pressure die-cast Mg alloys can be increased by decreasing the regions of localized clustered pores in the microstructure, which may not necessarily require decreasing the global average volume fraction of the pores in the three-dimensional microstructure. These observations also show that as the localized clustered pores constitute the extrema in the microstructure, and the fracture is governed by these extrema in the microstructural geometry rather than the average attributes such as average porosity volume fraction, average pore size. On the other hand, most of the current models and simulations of fracture in materials containing pores [92-95] utilize *global average* microstructural parameters (average volume fraction of pores, average pore size, etc.), and therefore, do not capture the variability in the fracture sensitive properties such as ductility in a set of specimens having the same average microstructure. Thus, there is a need to develop a new class of damage evolution and fracture models that incorporate the spatial clustering of shrinkage and gas pores in order to predict the variability in the fracture related properties of the HPDC Mg-alloys.

4.3.2 Simulation of Virtual Microstructures

Variability in the properties of cast components as discussed in the chapter 4.3.1 is obviously not desirable and limits materials properties by the tail end of distributions. Therefore, designer must assume the lowest possible property values, which translates to higher section thickness and, therefore, higher component weight, which offsets the advantage of magnesium alloy being low density. This variability also can lead to problems concerning reliability and safety issues. In this chapter, a new technique to simulate the microstructures with different degrees of porosity distribution by controlled parameters having realistic complex morphologies is presented. Such simulations permit parametric study of the effects of different degree of porosity distribution on the mechanical response of the microstructures.

4.3.2.1 Simulation of Microstructures Having Different Degrees of Pore Clustering

The pores in the high-pressure die-cast microstructures of Mg-alloys exhibit different degrees of spatial clustering depending on the process conditions. The spatial clustering of pores in turn affects the mechanical properties and contributes to variability in the properties. Therefore, it is of interest to first define a parameter that describes pore clustering, and then develop a methodology to simulate a series of microstructures that have same attributes except the degree of pore clustering.

It is of interest to incorporate the realistic complex porosity shapes and morphologies as well as other important microstructural attributes in the computer simulated microstructures, because the complex porosity morphologies can not be modeled as idealized shapes such as circles or ellipses. In the present work, recently developed technique that utilizes combination of digital image processing and microstructure simulations is used for the simulations of microstructures with realistic complex porosity shapes/morphologies [96-97]. First step is to grab the original microstructure and the microstructure has to be large enough to capture the long-range

distribution of pores in the microstructure. Figure 4.58 (a) shows a grey scale montage image created from the cross section of the gage of the AM50 tensile sample. Next step is to segment large pores, and to obtain the centroid coordinates of each pore from the coordination transformation as shown in figure 4.58 (b). Next step is to move each centroid coordinate toward the center of the frame according to a certain value in terms of degree of clustering, DC. Degree of clustering can be defined as follows. L is the original distance between each porosity centroid coordinate and origin at the center and L` is its corresponding distance toward the center after it has been displaced. For instance, when each porosity coordinate moves to the half of its original position, L` is equal to 0.5L, and therefore degree of clustering, DC, is equal to 2.

$$Degree\,of\ Clustering, DC = \frac{L(original\ distance)}{L`(clustered\ distance)}$$

Clustered large pores are illustrated in figure 4.58 (c). Next, superimpose the remaining porosity that was segmented at first step as shown in figure 4.58 (d). Note that this clustered porosity image has exactly the same number density and volume fraction as the original microstructure. Only difference is the clustering of the large porosity. Figure 4.59 shows the simulated microstructures with different degree of porosity clustering values, 1.2, 1.4, and 2.0.

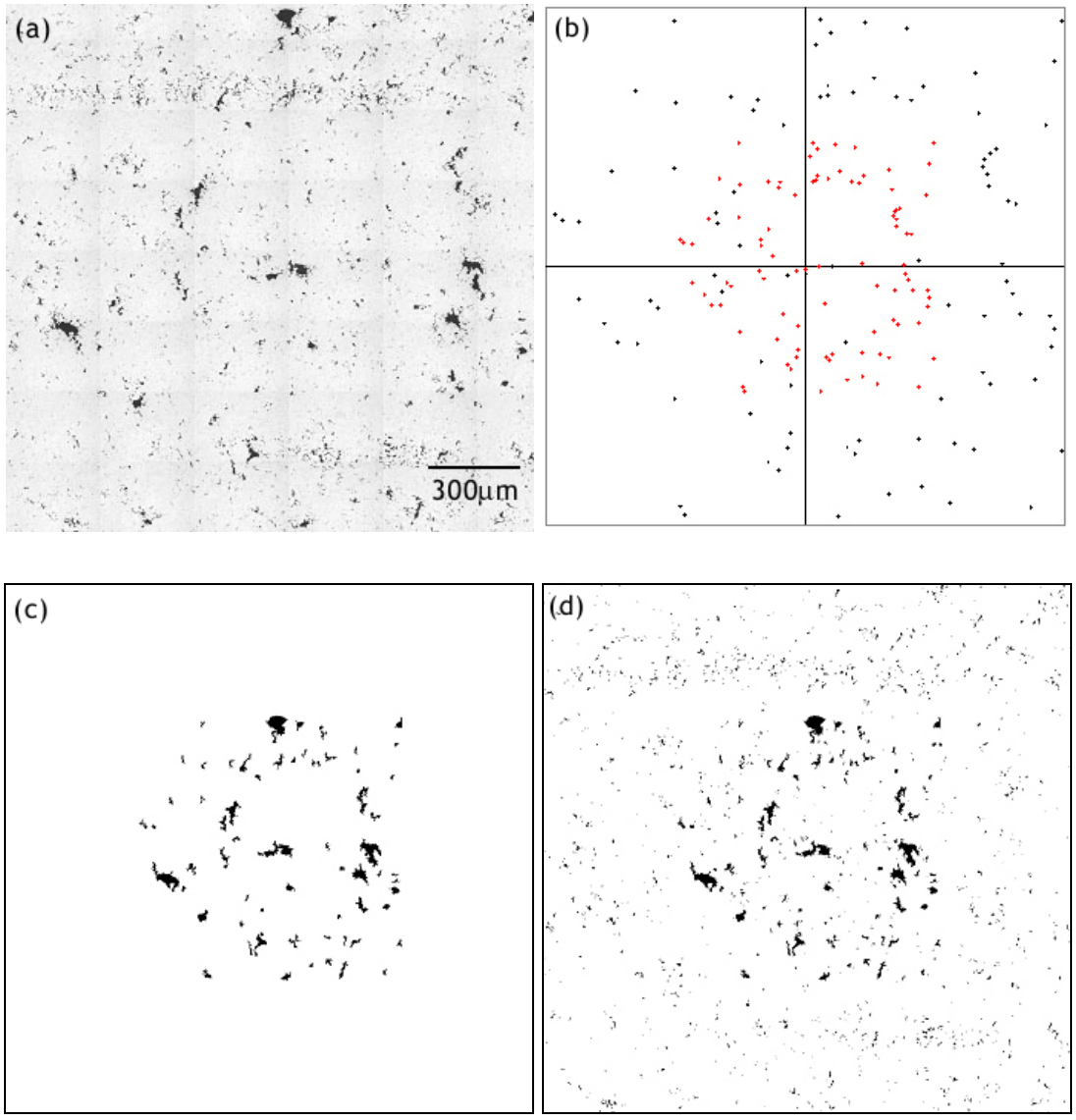

Figure 4.58: (a) original gray scale image, (b) centroid coordinate of each porosity representing black dot is the original coordinate and red one is new coordinate for clustering value, (c) large porosity corresponding coordinate, and (d) overlapped image with small porosity.

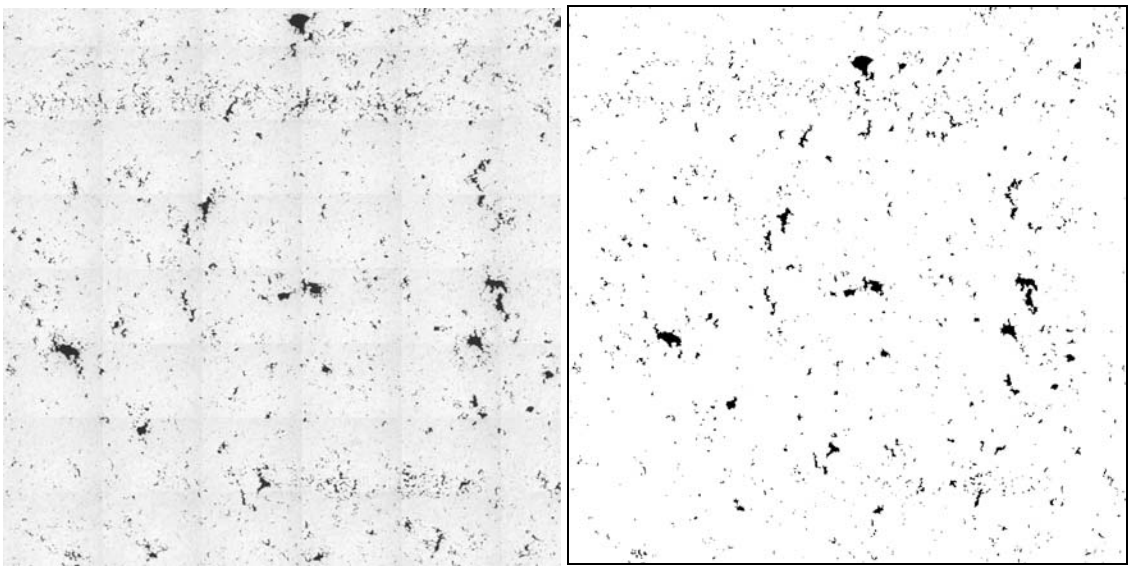

(a) (b)

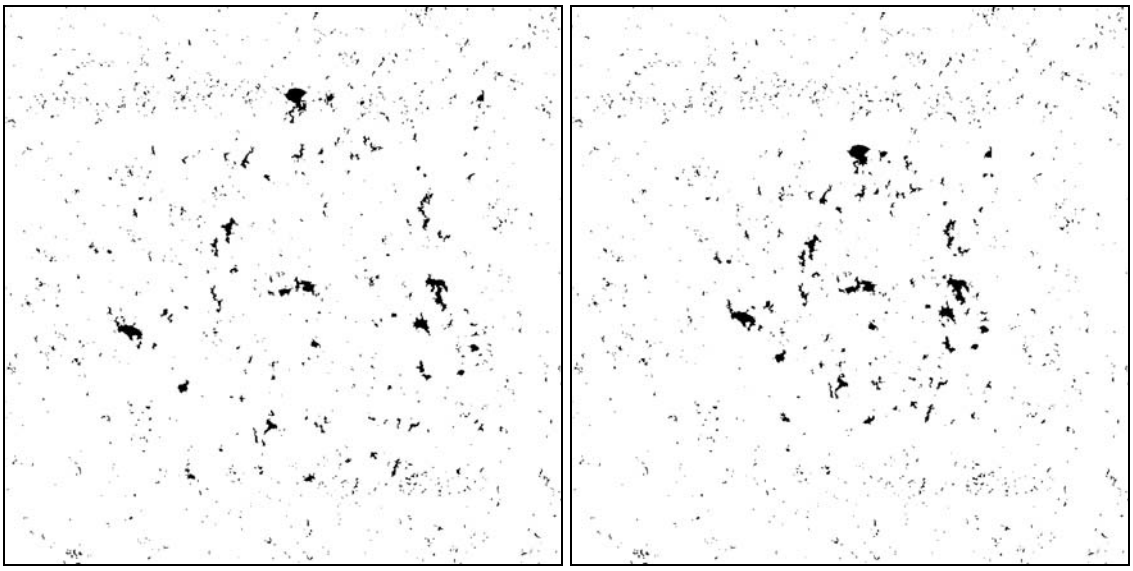

(c) (d)

Figure 4.59: Simulated microstructures with different degree of porosity clustering values (a) original image, DC 1.0, (b) DC 1.2, (c) DC 1.4, and (d) DC 2.0.

4.3.2.2 Simulation of Microstructures Having Different Pore Volume Fractions

Another possible way to simulate the clustered microstructure is by variation of volume fraction of porosity. Degree of volume fraction of porosity can be defined as follows.

$$Degree\,of\,Volume\,Fraction, DV = \frac{Vv'(simulated\ volume\ fraction\ of\ porosity)}{Vv(original\ volume\ fraction\ of\ porosity)}$$

Vv is the original volume fraction of porosity and Vv' is increased volume fraction of porosity. For instance, when same amount of porosity as that of porosity in original microstructure is added onto the simulated, Vv` is equal to 2Vv, and therefore degree of volume fraction, DV, is equal to 2. Conceptually, this simulation procedure is as follows. Consider a hypothetical experiment where a large number of porosity images are simply plucked out form the microstructural images and stored in boxes with specific size ranges, such that the set is representative of the size of the porosity population in the microstructure of the real material. Next, consider simulation of porosity centroids (as per some specified spatial arrangement and number density) in a digitized simulation space where the pixel size is the same as that in the microstructural images from which the porosity is plucked out. Finally takes out each porosity at random and place it at one simulated centroid by keeping their size distribution same as that in the original microstructure. Repeat the process till the desired DV values are achieved. The result is a simulated microstructure with controlled parameter, DV, but a different spatial arrangement and volume fraction of porosity. Figure 4.60 shows the simulated microstructure with different porosity volume fractions. Further, this simulation parameter, DV, can be combined with DC to generate a range of different simulated microstructures. The real and simulated microstructures can be implemented in a finite elements (FE) computational framework to study the micromechanical response of these microstructures.

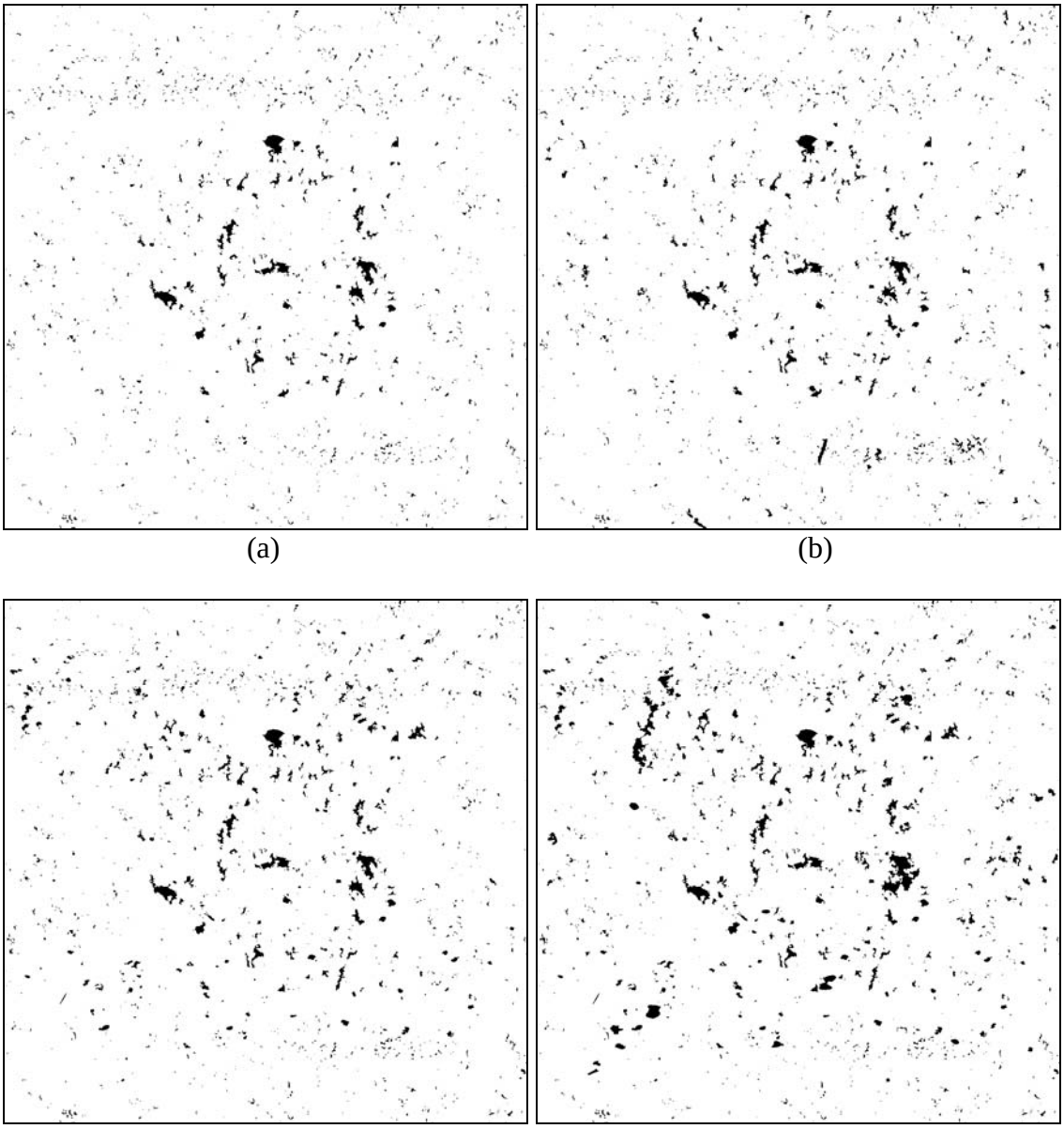

(a) (b)

(c) (d)

Figure 4.60: Simulated microstructures with different degree of porosity volume fraction (a) reference image, DV1.0, (b) DV 1.2, (c) DV 1.4, and (d) DV 2.0.

4.4 Relationships between Processing-Structure-Properties

Three components, processing, microstructures, and mechanical properties are closely intertwined, and therefore, an in-depth understanding of their relationships is essential for successful development and application of high-pressure die-cast (HPDC) Mg-alloys

HPDC process parameters significantly affect porosity, which is the most common casting defect that often serves as the weakest link in the microstructure under certain loadings. In order to understand the relationships between the HPDC process parameters and the porosity distributions, the first step is the quantitative characterization of porosity. For this purpose, in the present work, an efficient and unbiased montage based digital image processing technique has been developed, which permits automatic detection and segmentation of individual gas and shrinkage pores in the microstructure in an unbiased manner. This new image processing technique permits quantitative characterization of both gas and shrinkage pores via estimation of attributes such as size and spatial distribution, volume fraction, number density, and so on. In the present work, this technique has been applied for systematic study on the correlations between process parameters and porosity distributions in the HPDC plates of AM50 and AM60 alloys cast with different combinations of process parameters. Further, this technique also has been applied to correlate porosity with mechanical properties of HPDC Mg-alloys. The digital image analysis technique developed in this study is very essential for porosity characterization, which has been successful and can be applicable to other materials characterization.

The effects of individual process parameters on the porosity distribution have been systematically studied keeping all other process parameters the same, which permits deconvolution of the effects of each important process parameter on the porosity distributions. The sampling scheme for porosity characterization also enables constructing porosity distribution maps that are very useful for detailed understanding of

the effects of process parameters on the porosity and for validation of the computer simulations of HPDC casting process. The present data reveals that varying any of three process conditions, lowering gate velocity, liquid melt temperature, and intensification pressure has beneficial effects on decreasing porosity in both the AM50 thick and AM60 thin plates. The 3D porosity distributions constructed in this study clearly reveal in detail on the manner of porosity reduction in each plate. In the AM60 thin plates, a new type of shrinkage porosity named gas induced shrinkage porosity is observed and a hypothesis for formation of such porosity has been presented for the first time. This hypothesis is further supported by the three-dimensional microstructure reconstruction and numerical analysis for heat transfer. This analysis has lead to an important conclusion: under certain combination of process parameters, reduction in the gas porosity can automatically lead to some reduction in the shrinkage porosity.

In the present work, inverse macrosegregation on the cast surfaces has been observed for the first time in HPDC Mg-alloys and it has been correlated with the process parameters using novel digital image analysis and stereological techniques. This analysis has led to a very important conclusion of significant practical relevance: the process conditions intended to decrease the amount of porosity in turn lead to formation of inverse macrosegregation on the cast surfaces under specific conditions, which facilitates the earlier initiation of fatigue cracks. Consequently, process parameters to decrease both the porosity and inverse surface macrosegregation should be taken into consideration for improving the mechanical properties of cast Mg-alloys, which is one of important observations about the processing-microstructure-properties relationships in this study. The gathered quantitative relationships between process conditions and porosity provide the essential information on how these process conditions affect the formation of porosity and on how the porosity affects mechanical properties as well.

It is important to recognize that the porosity adversely affects the average fracture sensitive mechanical properties as well as the variability in these properties. Therefore, a

systematic study on the correlations between the variability in the microstructure and the corresponding variability in the relevant fracture related mechanical properties of HPDC AE44 Mg-alloy has been performed in this investigation. The quantitative fractographic data reveal strong quantitative correlation between the tensile ductility and the area fraction of the porosity present in the corresponding fracture surfaces. Therefore, the spatial clustering of pores significantly contributes to the variability in the fracture sensitive mechanical properties of the HPDC alloys. Such variability in the properties of cast components is obviously undesirable as it can lead to problems concerning reliability and safety issues. For future simulation studies on the effects of pore clustering on the fracture sensitive mechanical properties, a new microstructure simulation tool is developed that enables simulations of virtual microstructures having realistic complex pore morphologies, size and shape distributions, and different extents of spatial clustering of pores. In the future studies, these simulated virtual microstructures can be implemented in the object oriented finite analysis framework to simulate the variability in the mechanical response caused by the clustering of the pores.

CHAPTER 5

FUTURE WORK

In the chapter 4.3, a combination of digital image processing and simulations of spatial point processes has been used for the simulations of virtual microstructures with realistic complex porosity shapes/morphologies. The simulations incorporate realistic complex porosity shapes/morphologies similar to those present in the corresponding real microstructures. Harpreet Singh and co-workers [96] have recently reported a new methodology for incorporation of simulated microstructural windows in finite element-based computations to study the local stresses and strains. This technique can be applied to the simulated microstructures explored in this dissertation to study the micromechanical response and further can be enhanced in terms of damage initiation and evolution models in ABAQUS/Explicit that have the potential to evaluate the damage progress in materials to predict the variability in the mechanical properties of pressure die-cast Mg-alloys. This chapter presents preliminary works and some of the ideas for the finite element computations of simulated virtual microstructures for future work.

5.1 Elastic-Plastic Properties of Simulated Microstructure

The real and simulated microstructures as shown in Figure 4. 59 and 60 are meshed with linear triangular elements using object oriented finite element (OOF) software [58] and adaptive mesh routines are used to conform the element edges to the phase boundaries and to refine the element size as shown in Figure 5.1 and 5.2. The reported microscale constitutive properties by Shan and Gokhale [62] have been used as input properties for unbiased simulations that are not influenced by the presence of porosity.

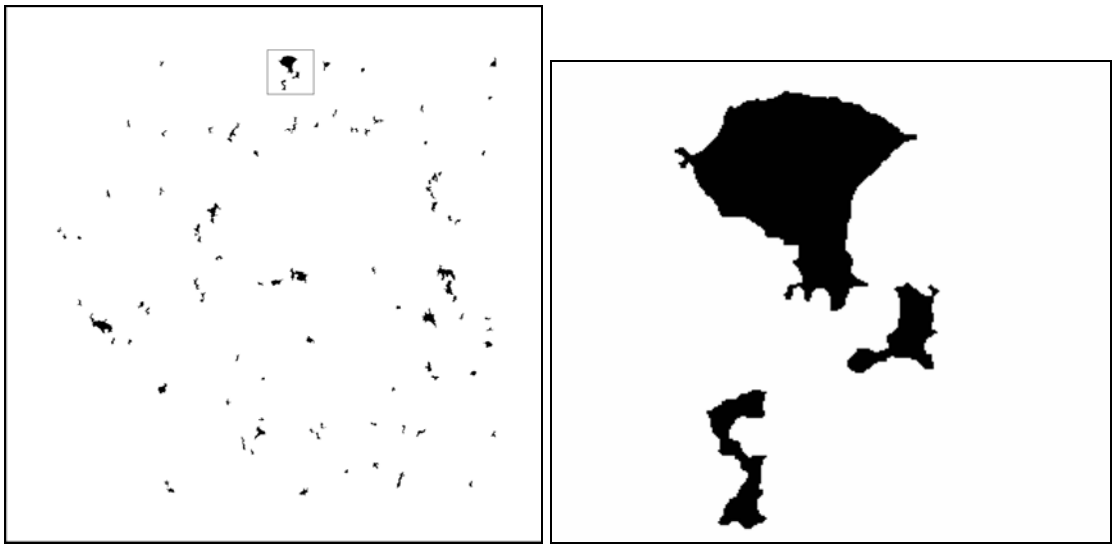

(a) (b)

Figure 5.1: (a) Binary montage image of a cast AM50 alloy and (b) magnified view of the small-bordered region.

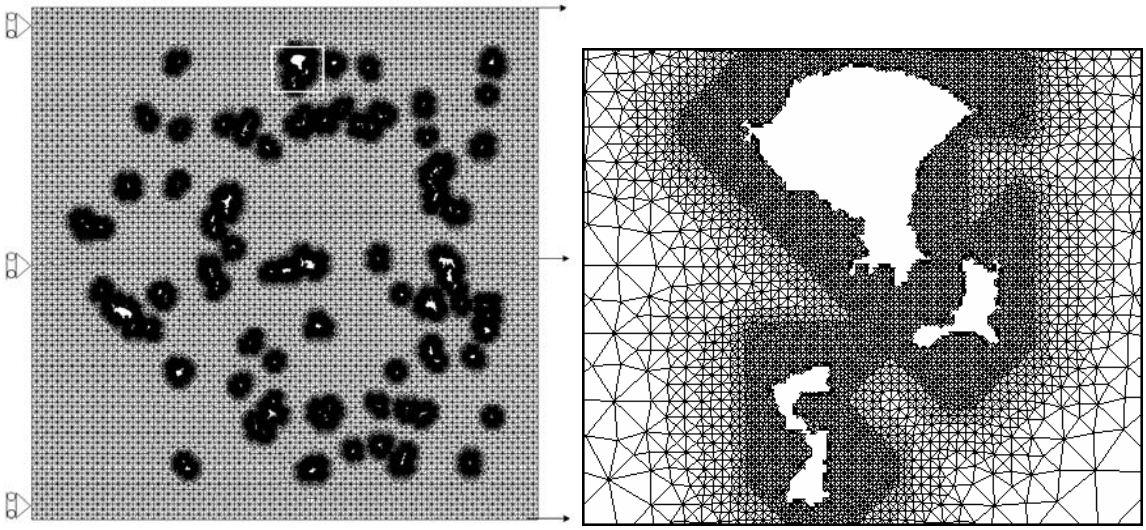

(a) (b)

Figure 5.2: (a) Finite element mesh and boundary conditions and (b) magnified view of the small-bordered region.

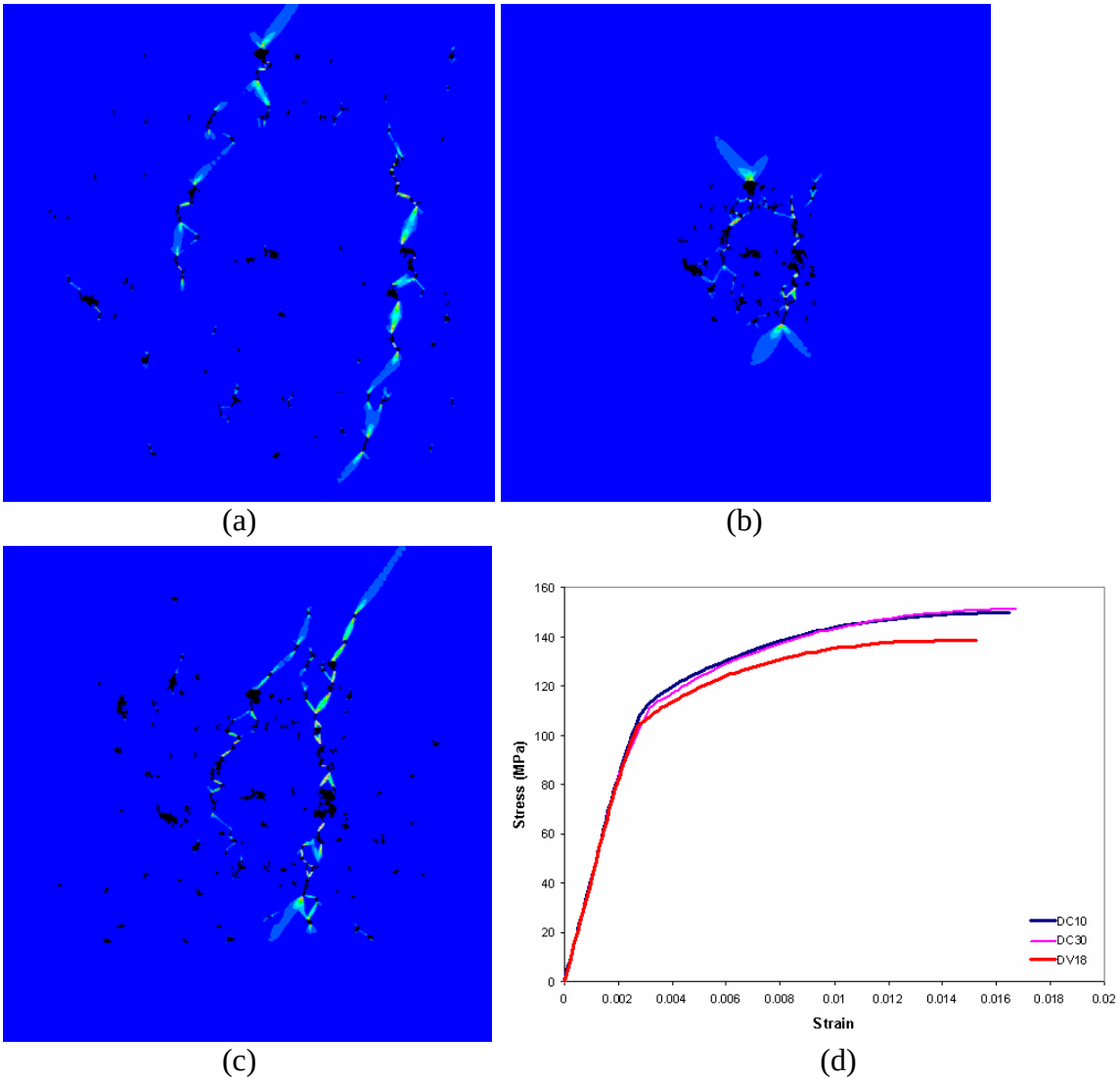

Figure 5.3: Contours for equivalent plastic strain at the strain of 2% for the real (a) and simulated microstructures DC 3.0 (b), DC 2.0 + DV 1.8 (c), and corresponding local stress-strain curves (d).

Left edge of the simulated space is constrained to move only in y direction (vertical direction) as shown in figure 5.2a and uniaxial loading is simulated by applying a strain of 2% along the tensile direction. The overall mechanical behavior of the material is determined by area averaging the stress/strain values at the integration point of each element in the finite element mesh. Figure 5.3 a, b, and c show the contours of equivalent plastic strains at the strain of 2% for the real and simulated microstructures with the parameters of DC 1.0, DC 3.0, and DC 2.0 and DV 1.8 respectively. The corresponding local stress-strain curves are shown in Figure 5.3d. There is no significant difference in local stress-strain curves between the microstructures. However the stress of the microstructure with the simulation parameters of DC 2.0 and DV 1.8 is slightly lower than the other two because of the reduction in the load-bearing area caused by the increased level of porosity volume fraction, DV. These properties can be extended to the region of materials failure based on the damage initiation and evolution models with element removal in ABAQUS/Explicit to predict the onset of damage and progressive degradation of the material stiffness. Such models will further the usefulness of simulated microstructures and will be explored in detail. Figure 5.4 shows simulated failed microstructures and computed percentage tensile ductility of the simulated microstructures. The computed tensile ductility of the simulated microstructures shows good agreement with the linear trend of test tensile data reported in the Table 4.9.

5.2 Model Extended to 3D Space

The same procedure can be further extended to simulations of realistic 3D microstructure as well. Such 3D analyses are particularly important for cast microstructure containing porosity where numerical analysis on the mechanical behaviors of the corresponding 2D observational planes can be seriously misleading in that some of fracture related characteristics such as the real three-dimensional stress distribution and preferential crack path can’t be involved in 2D observation planes. Such simulations of

the realistic 3D microstructure would require the 3D digital porosity images from the corresponding 3D microstructure. The realistic 3D porosity images can be obtained from the 3D microstructure reconstructed from serial sectioning as described in the chapter 4.2.

The reconstructed 3D microstructure in STL (stereo lithography) format is exported into Harpoon (CEI), commercial automatic meshing software to mesh the geometry with tetrahedral elements. Only the external volume of the STL file is meshed leaving the voids (porosity) free of elements as shown in Figure 5.5b. The microstructure is embedded in a homogeneous material volume to avoid edge effects. The FE mesh is then exported to ABAQUS, commercial finite element code and analyzed for the elastic mechanical response to a tensile load. Figure 5.5c shows the local von Mises stress distribution in the microstructural volume due to a tensile load. In the present contribution, the FE analysis is presented to illustrate the *methodology* for incorporation of the reconstructed 3D digital microstructural image in the computational framework of the FE techniques. The damage initiation and evolution models used in 2D analyses can be further applied to 3D microstructures to study the effects of 3D microstructures on the micromechanical behaviors. These 3D microstructures can be further simulated with the developed parameters of DC and DV for parametric studies of the effects of different degree of porosity distributions on the micromechanical behavior of materials. The following investigations could be taken up for future explorations.

- Further refinement and enhancement of damage initiation and evolution models
- Data collection and refinement of 3D microstructures
- Further enhancement of algorithms for 3D porosity distribution simulation
- Applications of simulation technique to other materials

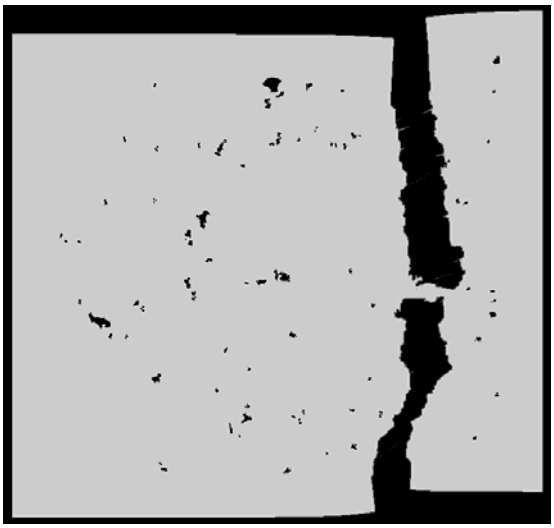

(a)

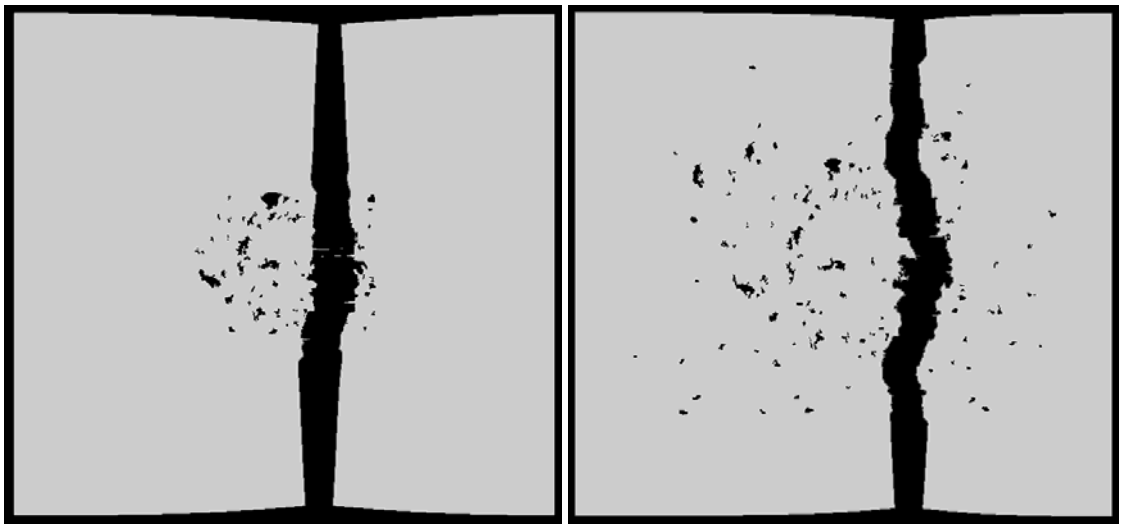

(b) (c)

Figure 5.4: Failed simulated microstructures and computed tensile ductility of (a) 10.3% (original, DC 1.0), (b) 7.5% (DC 3.0), and (c) 6.3% (DC 2.0 and DV 1.8).

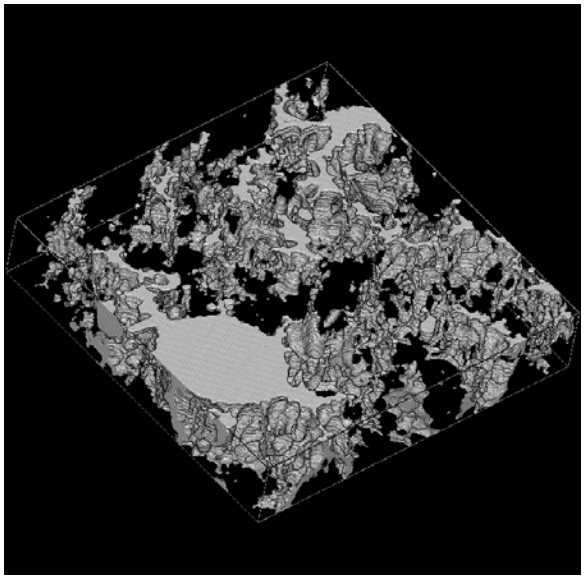

(a)

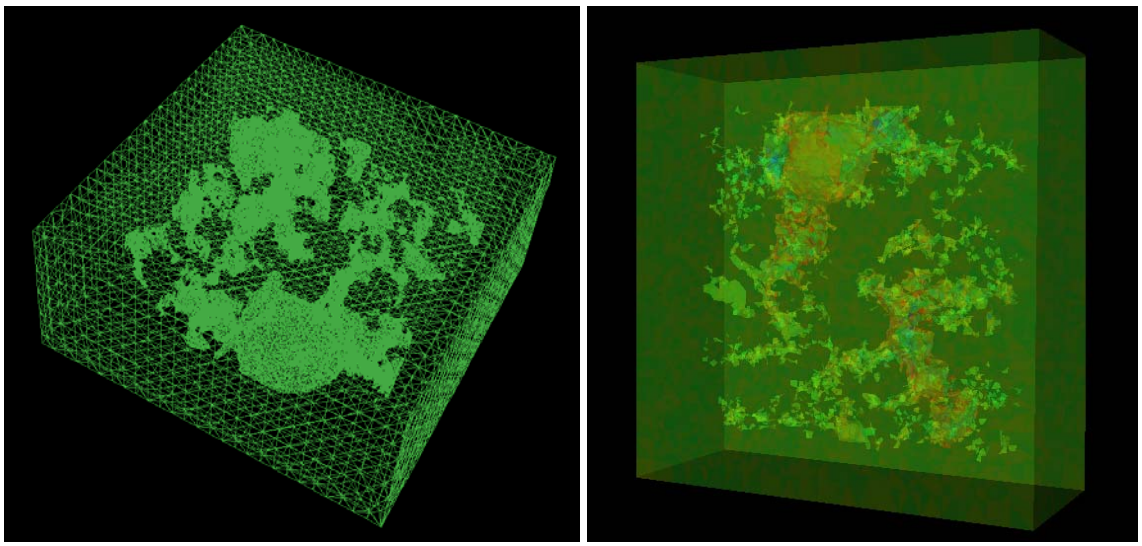

(b) (c)

Figure 5.5: (a) Reconstructed three-dimensional porosity image, (b) three-dimensional finite element mesh, and (c) corresponding analysis showing stress distribution around porosity.

CHAPTER 6

SUMMARY AND CONCLUSIONS

The central goal of this research was to quantitatively characterize the relationships between processing, microstructure, and mechanical properties of important high-pressure die-cast (HPDC) Mg-alloys. For this purpose, a series of experiments were performed to generate a set of HPDC microstructures and these microstructures have been quantitatively characterized. In addition, computer simulations of the HPDC microstructures with controlled parameters have been developed. The important observations, conclusions, and achievements of this research are as follows.

1. The digital image processing technique for automatic detection and segmentation of gas (air) and shrinkage pores in pressure die-cast Mg alloys was further developed to quantitatively characterize the size distribution and spatial arrangement of the porosity. This technique is essential to observe and quantify the gas and shrinkage pores in the HPDC microstructures.
2. The experimental parametric study has been performed to quantitatively characterize the effects of HPDC process parameters on the porosity distributions in the HPDC AM50 Mg-alloy. The main observations and conclusions are as follows.
    - A decrease in the gate velocity decreases the total amount of porosity predominantly via a decrease in the gas porosity and a small extent of decrease in the shrinkage porosity. The lower gate velocity uniformly decreases the number density and area fraction of gas pores of all sizes (small and large).
    - Application of intensification pressure significantly reduces the total amount of porosity primarily via reduction in the gas porosity. The intensification pressure significantly reduces the number density and area fraction of the gas pores larger than 100μm diameter.

- A decrease in the melt temperature also reduces the total amount of porosity primarily via reduction in the gas porosity. The lower melt temperature reduces the number density and area fraction of the gas pores larger than 30 μm.
- There are no beneficial synergistic effects of combinations of process parameters in decreasing the shrinkage porosity.

3. It is shown that the presence of gas porosity in the HPDC casting components can lead to the formation of a new type of shrinkage porosity, gas induced shrinkage porosity, under specific conditions, because the presence of gas porosity can retard the heat transfer and change the local solidification rate leading to the formation of gas induced shrinkage porosity. Two- and three-dimensional metallographic evidence has been presented to support this hypothesis, and it is further substantiated using heat transfer simulations. The visualization of the reconstructed 3D microstructures yields the real morphologies of the gas and shrinkage porosity, their connectivity, and spatial correlations, which further support conclusions drawn from the numerical analysis and 2D microstructural observations.
4. An experimental parametric study has been carried out to quantitatively characterize the effects of gate velocity, intensification pressure, and melt temperature on the porosity distributions in the high-pressure die-cast AM60 Mg-alloy. These process parameters affect the porosity volume fraction in ways similar to those observed in the AM50 alloy. However, in these thin plates (4 mm thickness), the shrinkage porosity has higher contribution to the total porosity volume fraction. This is due to formation of gas induced shrinkage porosity at lower section thickness levels.
5. Under certain process conditions, extensive inverse surface macrosegregation can occur in the high-pressure die-cast AM60 Mg-alloy. The combination of process parameters such as lower gate velocity, application of intensification, or lower liquid melt temperature that usually leads to lower micro-porosity gives rise to a substantially higher extent of inverse macrosegregation on the cast surfaces of this

alloy, which can adversely affect the fatigue life. The combination of process parameters that usually leads to lower micro-porosity gives rise to higher extent of the macrosegregation to an extent where the beneficial effects of lower micro-porosity on the fatigue life are swamped by the detrimental effects of the inverse surface macrosegregation. Therefore, it is essential to minimize *both* micro-porosity and macrosegregation in the high-pressure die-castings of the Mg-alloys.

6. An efficient and unbiased montage serial sectioning technique has been applied for reconstruction of large-volume high-resolution 3D microstructures of high-pressure die-cast AM50 and AE44 Mg-alloys. The reconstruction of 3D microstructures from montage serial sections enables visualization and characterization of detailed 3D morphologies and spatial correlations of gas and shrinkage porosity and dendrite and eutectic phases. The reconstructed 3D microstructure is implemented in a 3D finite elements (FE) computational framework to illustrate how realistic complex microstructural feature morphologies can be incorporated in the simulations of micromechanical response of these high-pressure die-cast cast microstructures.
7. High-pressure die-cast AM50 and AE44 Mg-alloys exhibit variability in the tensile ductility. The variability in the tensile ductility does not quantitatively correlate to the average volume fraction of porosity in the bulk three-dimensional microstructure. There is a quantitative correlation between the tensile ductility and the area fraction of the porosity present in the corresponding fracture surfaces, which can be represented by a simple power law type equation. The fracture path preferentially goes through the regions containing localized and clustered pores, and therefore, in these cast microstructures, the fracture related properties such as ductility are more sensitive such local extrema in the microstructure rather than global averages of microstructural attributes such as porosity volume fraction.
8. A new method is developed for efficient computer simulations of realistic microstructures with different degrees of porosity clustering, DC and volume fraction,

DV. The simulations incorporate realistic complex porosity shapes/morphologies similar to those present in the corresponding real microstructures. These simulated microstructures can be incorporated in a finite elements (FE) computational framework to study the micromechanical response of these simulated microstructures.

REFERENCES

[1] Magnesium and Magnesium Alloys, ASM Specialty Handbook, edited by Michael M. Avedesian and Hugh Baker, 1999.

[2] R. Brown, Light Metal Age, vol. 50 (No. 5 and 6), pp. 21, 1992.

[3] "Magnesium", www.bookrags.com/sciences/sciencehistory/magnesium-wsd.html (accessed Oct. 15, 2005)

[4] J. A. Carpenter, Materials Science Forum, vol. 488-489, pp. 17-20, 2005.

[5] J. Aragones, K. Goundan, S. Kolp, R. Osborne, L. Ouimet, and W. Pinch, SAE Transactions. Paper 2005-01-0340, 2005.

[6] B. R. Powell, Journal of Materials, vol. 55, pp. 28-30, 2003.

[7] Naiyi Li, Richard Osborne, Bruce Cox, and Donald Penrod, SAE Transactions, Paper 2005-01-0337, 2005.

[8] www.dynacast.com/die-casting (accessed Oct. 22, 2005)

[9] H. Okamoto, J. Phase Equilibria, vol. 19 (No. 6), pp. 598, 1990.

[10] A. Balasundaram and A. M. Gokhale, Materials Characterization, vol. 46, pp. 419-426, 2001.

[11] A. K. Dahle, S. Sannes, D. H. St. John, and H. Westengen, Journal of Light Metals, vol. 1, pp. 99-103, 2001.

[12] B. J. Coultes, J. T. Wood, G. Wang, and R. Berkmortel, Proceedings of Symposium Magnesium Technology 2003, eds. H. I. Kaplan, TMS, Warrendale, pp. 45-50, 2003.

[13] A. M. Gokhale and G. R. Patel, Proceedings of Symposium Magnesium Technology 2001, eds. J. Hryn, TMS, Warrendale, pp. 195-199, 2001.

[14] V. D. Tsoukalas, St. A. Mavrommatis, N. G. Orfanoudakis, and A. K. Baldoukas, Journal of Engineering Manufacture, vol. 218, pp. 77-86, 2004.

[15] H. T. Gjestland, S. Sannes, H. Westerngen, and D. Albright, Die Casting Engineer, July issue, pp. 56-65, 2004.

[16] W. P. Sequeria, M. T. Nurray, G. L. Dunlop, and D. H. StJone, Proceedings of Automotive Alloys 1997, TMS, Warrendale, PA, pp. 169-187, 1997.

[17] D. F. Allsop and D. Kennedy, Pressure Die Casting, The Technology of the Casting and the Die, Pergamon Press, Oxford, UK, pp. 216-219, 1983.

[18] S. G. Lee, G. R. Patel, A. M. Gokhale, and M. Evans, Proceedings of Symposium Mgnesium Technology 2005, eds. N. Neelmeggham, H. I. Kaplan, and B. R. Powell, TMS, Warrendale, PA, pp. 371-375, 2005.

[19] S. G. Lee, A. M. Gokhale, and G. R. Patel, Materials Characterization, vol. 55, No. 3, pp. 219-224, 2005.

[20] E. M. Gutman, Y. B. Unigovski, A. Eliezer, E. Abramov, and E. Aghion, Materials Technology, vol. 16, pp. 126-132, 2001.

[21] W. G. Walkington, Die Casting Defects, NADCA press, Rosemont, IL.

[22] Y. J. Huang, B. H. Hu, I. Pinwill, W. Zhou, and D. M. R. Taplin, Materials and Manufacturing Processes, vol. 15, pp. 97-105, 2000.

[23] G. G. Wang, B. Froese, and P. Bakke, Proceedings of Symposium Magnesium Technology 2003, eds. H. I. Kaplan, TMS, Warrendale, pp. 65-69, 2003.

[24] A. L. Bowles, J. R. Griffiths, and C. J. Davidson, Proceedings of Symposium Magnesium Technology 2001, eds. J. Hryn, TMS, Warrendale, pp. 161-168, 2001.

[25] D. Rodrigo and M. Murray, SAE Technical Paper, 1999-01-0927, 1999.

[26] M. Easton, T. Abbott, and C. Caceres, Materials Science Forum, vol. 419-422, pp. 147-152. 2003.

[27] C. Hung, M. Chang, and N. Tang, Proceedings of Symposium Magnesium Technology 2004, eds. A. A. Luo, TMS, Warrendale, pp. 193-196, 2004.

[28] X. P. Niu, B. H. Hu, I. Pinwill, and H. Li, Journal of Materials Processing Technology, vol. 105, pp. 119-127, 2000.

[29] M. McLaughlin, C. W. Kim, G. P. Backer, J. Prindiville, S. G. Lee, and A. M. Gokhale, Die Casting Engineer, vol. 48, Sep. 40-45, 2004.

[30] G. Chadha, J. E. Allison, and J. W. Jones, Proceedings of Symposium Magnesium Technology 2004, eds. A. A. Luo, TMS, Warrendale, pp. 181-186, 2004.

[31] I. L. Ferreira, C. A. Santos, V. R. Voller, and A. Garcia, Metallurgical and Materials Transactions B, vol 35B, 285-297, 2004.

[32] A. K. Dahle and D. H. St. John, Acta Materialia, vol. 47, pp. 31-41, 1999.

[33] P. D. McCormack and L. Crane, Physical Fluid Dynamics, Academic Press, New York, 1973.

[34] A. Mo, Int. J. Heat Mass Transfer, vol. 36, pp. 4335-4340, 1993.

[35] F. Kaempffer and F. Weinberg, Metallurgical Transactions, vol. 2, pp. 2477-2483, 1971.

[36] B. R. Henriksen and E. K. Jensen, In Light Metals, TMS-AIME, Warrendale, PA, pp. 969-977, 1993.

[37] E. Haug, A. Mo, and H. J. Thevik, Int. J. Heat Mass Transfer, vol. 38, pp. 1553-1563, 1995.

[38] H. J. Thevik and A. Mo, Modeling of Casting, Welding and Advanced Solidification Processes VII, pp. 557-564, 1995.

[39] H. J. Thevik and A. Mo, Int. J. Heat Mass Transfer, vol. 40, pp. 2055-2065, 1997.

[40] M. M'hamdi, A. Mo, D. Mortensen, and H. G. Fjær, in Light Metals, TMS, Warrendale, PA, pp. 695-701, 2002.

[41] M. M'Hamdi and A. Håkonsen, Modeling of Casting, Welding and Advanced Solidification Processes X, TMS, pp. 505-512, 2003.

[42] S. G. Lee, G. R. Patel, and A. M. Gokhale, Materials Science Forum, vol 488, pp. 713-717, 2005.

[43] S. G. Lee, G. R. Patel, and A. M. Gokhale, Proceedings of Symposium Magnesium Technology 2005, eds. N. Neelameggham, TMS, Warrendale, pp. 377-380, 2005.

[44] J. P. Weiler, J. T. Wood, R. J. Klassen, E. Maire, R. Berkmortel, and G. Wang, Materials Science and Engineering A, vol. 359, pp, 315-322, 2005.

[45] P. Louis and A. M. Gokhale, Metallurgical and Materials Transactions A, vol. 26A, pp. 1449-1455, 1995.

[46] P. Louis and A. M. Gokhale, Acta Materialia, vol. 44, pp. 1519-1528, 1996.

[47] F. N. Rhines and K. R. Craig, Metallurgical Transactions *A*, vol. 7A, pp. 1729-1734, 1976.

[48] R. S. Sidhu and N. Chawla, Materials Characterization, vol. 52, pp. 225-230, 2004.

[49] M. Li, S. Ghosh, O. Richmond, H. Weiland, and T. N. Rouns, Materials Science and Engineering, vol. A265, pp.153-173, 1999.

[50] K. M. Wu and M. Enomoto, Scripta Materialia, vol. 46, pp. 569-574, 2002.

[51] M. V. Kral, M. A. Mangan, G. Spanos, and R. O. Rosenberg, Materials Characterization, vol. 45, pp. 17-23, 2000.

[52] T. Yokomizo, M. Enomoto, G. Spanos, and R. O. Rosenberg, Materials Science and Engineering, vol. 344A, pp. 261-267, 2003.

[53] A. Tewari, A.M. Gokhale, and R. M. German, Acta Materialia, vol. 47, pp. 3721-3734, 1991.

[54] S. Yang, A. Tewari, and A.M. Gokhale, Acta Materialia, vol.45, pp. 3059-3069, 1997.

[55] A. M. Gokhale and A. Tewari, Journal of Microscopy, vol. 200, pp. 277-283, 2000.

[56] A. Tewari and A.M. Gokhale, Materials Characterization, vol. 46, pp. 329-335, 2001.

[57] M.D. Dighe, A. Tewari, G. R. Patel, T. Mirabelli, and A. M. Gokhale, Transactions American Foundry Society, vol. 99, pp. 353-356, 2000.

[58] OOF: Analysis of Real Microstructures, www.ctcms.nist.gov/oof.

[59] A. M. Gokhale and S. Yang, Composites Science and Technology, vol. 60, pp. 2547, 2000.

[60] Z. Shan and A. M. Gokhale, International Journal of Plasticity, vol. 20, pp. 1347, 2004.

[61] Z. Shan and A. M. Gokhale, Acta Materialia, vol. 49, pp. 2001, 2001.

[62] Z. Shan and A. M. Gokhale, Materials Science and Engineering A, vol. 361, pp. 267-274, 2003.

[63] E. Keppel, IBM Journal of Research and Development, vol. 19, pp. 2, 1975.

[64] E.W. Lorensen and H. E. Cline, Computer Graphics, vol. 22, pp. 38, 1987.

[65] P. Sabella, Computer Graphics, vol. 22, pp. 51, 1988.

[66] A.M. Gokhale and G.R. Patel, Aluminum 2002, Proceedings of TMS Symposium on Automotive Alloys 2002, eds, M. Skillinberg and S. Das, TMS, Warrendale, pp. 65-73, 2002.

[67] S. G. Lee, G. R. Patel, A. M. Gokhale, A. Sreeranganathan, H. T. Gjestland, and M. F. Horstemeyer, Scripta Materialia, vol. 53, pp. 851-856, 2005.

[68] M. K. Surappa, E. W. Blank, and J. C. Jaquet, Scripta Metallurgica, vol. 20, pp. 1281-1286, 1986.

[69] A. M. Gokhale and G. R. Patel, Materials Science and Engineering, vol. 392, pp. 184-190, 2005.

[70] A. M. Gokhale and G. R. Patel, Materials Characterization, vol. 54, pp. 13-20, 2005.

[71] A. M. Gokhale, ASM Handbook, vol. 11, Materials Park, Ohio, ASM International, pp. 538, 2002.

[72] K. Gall, G. Biallas, H. Maier, P. Gullett, M. F. Horstemeyer, D. M. McDowell, and J. Fan, International Journal of Fatigue, vol. 26, pp. 59, 2004.

[73] M. F. Horstemeyer, N. Yang, K. Gall, D. M. McDowell, J. Fan, and P. M. Gullett, Acta Materialia, vol. 52, pp. 1327, 2004.

[74] D. Stoyan, W. S. Kendall, and J. Mecke, Stochastic geometry and its applications, John Wiley & Sons, Chichester, New York, Brisbane, Toronto, Singapore, 1995.

[75] P. Bakke and H. Westengen, Proceedings of Magnesium Technology 2005, TMS, Warrendale, eds. N. R. Neelamegham, H. I. Kaplan, B. R. Powell, pp. 291-296, 2005.

[76] E. J. Vinarcik, High integrity die casting processes, John Wiley & Sons, Inc, 2002.

[77] M. Barkhudarov, Die Casting Engineer, Jan. pp. 52-54, 2006.

[78] Arun Sreeranganathan, Ph. D. Dissertation Proposal, 2006.

[79] S. A. Langer, E. R. Fuller, and W. C. Carter, Computing in Science and Engineering, vol. 3A, pp. 15, 2001.

[80] ABAQUS 6.5 Documentation; User's Manual

[81] S. G. Lee, G. R. Patel, A. M. Gokhale, A. Sreeranganathan, H. T. Gjestland, and M. F. Horstemeyer, Scripta Materialia, vol. 53, pp. 851-856, 2005.

[82] K. S. Nair and M. C. Mittal, Materials Science Forum, vol. 30, pp. 89, 1998.

[83] G. Pettersen, H. Westengen, R. Hoier, and O. Lohne, Materials Science and Engineering A207, pp. 115, 1996.

[84] G. S. Foerster, Proceedings of 8th SDCE International Casting Exposition and Congress, Paper no. G-T75-112, 1975.

[85] T. Aune, T. Westengen, and T. Ruden, SAE Transactions, Technical Paper No. 94077, 1994.

[86] P. Bakke and H. Westengen, Proceedings of Magnesium Technology 2005, TMS, Warrendale, pp. 291-296, 2005.

[87] C. W. Hirt, Flow Science Technical Notes, FSI-03-TN66, 2004.

[88] Yoon Ho Kim, Soft-Tech International Inc., South Korea.

[89] C. H. Caceres and B. I. Selling, Materials Science and Engineering, 220, pp. 109-116.

[90] R. J. Bourcier, D. A. Koss, R. E. Smelser, and O. Richmond, Acta Metallurgica, Vol. 34, pp. 2443-2453, 1986.

[91] Z. Marciniak and K. Kuczinski, Int. J. Mech. Sci., Vol. 9, pp. 609-620, 1967.

[92] A.L. Gurson, Journal of Engineering Materials and Mechanics, Vol. 99, pp. 2-12, 1977.

[93] V. Tvergaard, International Journal of Fracture, Vol. 33, pp. 1079-1087, 1985.

[94] F.A. McClintock, Journal of Applied Mechanics, Vol. 35, pp. 363, 1968.

[95] L.M. Brown and J.D. Embury, Proceedings of Third International Conference on the Microstructure and Design of Alloys, Institute of Metals, London, UK, 1, pp. 164-173, 1973.

[96] H. Singh, Y. Mao, A. Sreeranganathan, and A. M. Gokhale, Modeling and Simulation in Materials Science and Engineering, Vol. 14, pp. 351-363, 2006.

[97] H. Singh, A. M. Gokhale, Y. Mao, and J. E. Spowart, Acta Materialia, Vol. 54, pp. 2131-2143, 2006.